UNIVERSITÉ DE GRENOBLE

THÈSE

Pour obtenir le grade de

DOCTEUR DE L'UNIVERSITÉ DE GRENOBLE

Spécialité : **Physique Subatomique et Astroparticules**

Arrêté ministériel : 7 août 2006

Présentée par

Yann Dutheil

Thèse dirigée par **Johann Collot**

et codirigée par **François Méot**

préparée au sein du **laboratoire national de Brookhaven**

et de l'**école doctorale de physique de Grenoble**

Modélisation de la dynamique de spin dans l'AGS basée sur une méthode de résolution pas-à-pas du mouvement

Spin dynamics modeling in the AGS based on a stepwise ray-tracing method

Thèse soutenue publiquement le **8 avril 2015**,
devant le jury composé de :

Dr. Ralph Aßmann

Physicien, synchrotron allemand à électrons (DESY), Hambourg, Allemagne, Rapporteur

Pr. Andreas Lehrach

Professeur, université technique de Rhénanie-Westphalie, Aix-la-Chapelle, Allemagne, Rapporteur

Pr. Johann Collot

Professeur, université Joseph Fourier, Grenoble, France, Directeur de thèse

Dr. Haixin Huang

Physicien, laboratoire national de Brookhaven (BNL), New York, Etats-Unis, Co-Encadrant de thèse

Dr. François Méot

Physicien, laboratoire national de Brookhaven (BNL), New York, Etats-Unis, Co-Directeur de thèse

Pr. François Montanet

Professeur, université Joseph Fourier, Grenoble, France, Examinateur

Abstract

The AGS provides a polarized proton beam to RHIC. The beam is accelerated in the AGS from $G\gamma = 4.5$ to $G\gamma = 45.5$ and the polarization transmission is critical to the RHIC spin program. In the recent years, various systems were implemented to improve the AGS polarization transmission. These upgrades include the double partial snakes configuration and the tune jumps system. However, 100 % polarization transmission through the AGS acceleration cycle is not yet reached. The current efficiency of the polarization transmission is estimated to be around 85 % in typical running conditions.

Understanding the sources of depolarization in the AGS is critical to improve the AGS polarized proton performances. The complexity of beam and spin dynamics, which is in part due to the specialized Siberian snake magnets, drove a strong interest for original methods of simulations. For that, the Zgoubi code, capable of direct particle and spin tracking through field maps, was here used to model the AGS.

A model of the AGS using the Zgoubi code was developed and interfaced with the current system through a simple command: the *AgsFromSnapRampCmd*. Interfacing with the machine control system allows for fast modelization using actual machine parameters. Those developments allowed the model to realistically reproduce the optics of the AGS along the acceleration ramp. Additional developments on the Zgoubi code, as well as on post-processing and pre-processing tools, granted long term multiturn beam tracking capabilities: the tracking of realistic beams along the complete AGS acceleration cycle.

Beam multiturn tracking simulations in the AGS, using realistic beam and machine parameters, provided a unique insight into the mechanisms behind the evolution of the beam emittance and polarization during the acceleration cycle. Post-processing softwares were developed to allow the representation of the relevant quantities from the Zgoubi simulations data. The Zgoubi simulations proved particularly useful to better understand the polarization losses through horizontal intrinsic spin resonances

The Zgoubi model as well as the tools developed were also used for some direct applications. For instance, some beam experiment simulations allowed an accurate estimation of the expected polarization gains from machine changes. In particular, the simulations that involved involved the tune jumps system provided an accurate estimation of polarization gains and the optimum settings that would improve the performance of the AGS.

Acknowledgments

I would like to express my special appreciation and thanks to my supervisor Dr. François Méot, you have been a tremendous mentor for me. I would like to thank you for encouraging my research and for allowing me to grow as a research scientist. Your advice on both research as well as on my career have been priceless. I would also like to thank Pr. Johann Collot, for keeping a distant but always careful eye on my work, and Dr. Haixin Huang who always found time to share his expertise of the AGS.

I would like to thank my committee members Dr. Ralph Aßmann, Pr. Andreas Lehrach and Pr. François Montanet for taking time to review my thesis and attend my defense.

In addition, I would like to thank Dr. L. A. Ahrens, Dr. K. Brown, Dr. C. Gardner, Dr. E. D. Courant, J. W. Glenn, Dr. N. Tsoupas for the help and fruitful discussions we had over the last few years. I am also thankful to Dr. Thomas Roser and Dr. Wolfram Fisher for their support and welcome in the collide accelerator department.

I thank the operators and the operation support group for their constant work. In particular, I acknowledge the expertise and work from Dr. A. Zelenski for providing ever higher polarization from the OPPIS source and K. Zeno for his careful tuning of the injectors.

I also use this occasion to thanks the NERSC facility for giving me the opportunity to use their powerful supercomputers[1].

[1]This research used resources of the National Energy Research Scientific Computing Center, a DOE Office of Science User Facility supported by the Office of Science of the U.S. Department of Energy under Contract No. DE-AC02-05CH11231.

Contents

List of Figures

List of Tables

Chapter 1

RHIC Experimental Complex

1.1 RHIC Spin Program

The spin, the proton and the proton spin crisis

The spin of a particle is its intrinsic angular momentum. It plays a very important role in modern physics, but it is in particle physics that the spin is the most challenging to understand. While the proton is known to be a spin $^1/_2$ composed subatomic particle, the question of how its spin is distributed among its constituents arises [6].

In quantum chromodynamics, the proton is composed of 3 valence quarks, gluons and sea quarks (pairs of virtual quarks and anti-quarks). Quarks are elementary fermions (of spin $S = {}^1/_2$) and gluons are bosons ($S = 1$). For a long time, it was assumed that only the 3 quarks of the proton were contributing to its spin. In 1987 the EMC[2] realized an experiment of deep inelastic muon-proton scattering to measure the spins of the quarks in the protons of the target. Results showed that the spin of the valence and sea quarks (Σ) do not contribute by more than 30% to the spin of the proton, instead of 100% as expected. This was totally unexpected by the physics community and led to a theoretical crisis often referred as the *proton spin crisis* [7]. It was then stated that

[2]European Muon Collaboration

the missing fraction of the spin must be created by the gluon spin (ΔG), gluon orbital angular momentum (L_{G}) and quark orbital angular momentum (L_{q}). The contributions to the proton spin can be summarized by:

$$\frac{1}{2} = \frac{1}{2}\Sigma + \Delta G + L_{\mathrm{q}} + L_{\mathrm{G}} \tag{1.1}$$

Overview and ambitions of the RHIC spin program

The RHIC[1] is the first high-energy polarized proton collider. It was commissioned at BNL[2] in 2001. The RHIC is capable today of delivering collisions of polarized protons at energies up to $\sqrt{s} = 510\mathrm{GeV}$ with an average beam polarization of 50 to 55 %. Energies of $\sqrt{s} = 510\mathrm{GeV}$ or $\sqrt{s} = 200\mathrm{GeV}$ and collisions of transversally or longitudinally polarized protons allow to probe various characteristics of the proton spin structure. The two experiments STAR[3] and PHENIX[4] have recently reported, for the first time, a non-zero contribution of the gluons to the proton spin [8]. In the coming years the RHIC spin program is expected to be extended to collisions of polarized protons with polarized ^{3}He and other heavy nuclei. The RHIC program will not only explore important questions in spin physics but it will also give the opportunity to study cold QCD matter effects through proton-ion collisions, as part of the heavy ion RHIC program. Whatever the investigated physics is, the polarization of the proton beams is critical. While in general the physics potential grows linearly with the integrated luminosity, it scales quadratically or even quartically with the beam polarization, depending on the physics process explored. This drives a strong interest to improve the beam's polarization in collision.

While proton bunches are produced polarized, their polarization can only decrease during the acceleration through the RHIC chain of accelerators. Polarization losses are observed through the last two acceleration stages: in the AGS[5] and in the RHIC. Therefore, increasing the polarization

[1] Relativistic Heavy Ion Collider
[2] Brookhaven National Laboratory
[3] Solenoidal Tracker at RHIC
[4] Pioneering High Energy Nuclear Interaction eXperiment
[5] Alternating Gradient Synchrotron

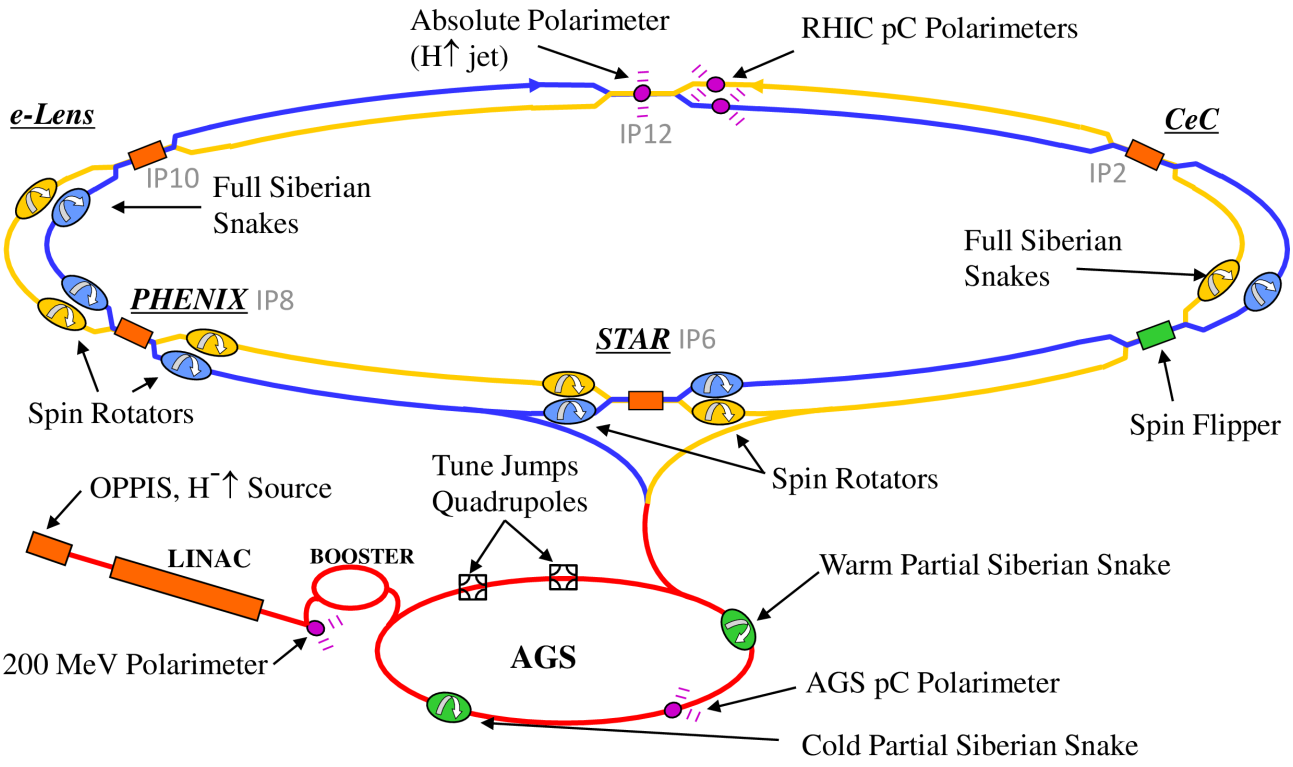

Figure 1.1 Schematic representation of the RHIC complex with the important devices involved in the acceleration of polarized protons.

transmission through the AGS is critical for the RHIC spin program.

1.2 General Presentation of the RHIC Complex

The experimental complex dedicated to high-energy physics at the BNL accelerates polarized protons up to 255GeV. Figure 1.1 shows that many stages and multiple specialized devices are needed to provide collisions of polarized protons at the two physics experiments: STAR and PHENIX.

The OPPIS[1] produces polarized H^- ions using multiple steps and a unique experimental apparatus. After production in an atomic hydrogen injector and stripping in a gas ionizing cell,

[1] Optically Pumped Polarized Ion Source

protons pick-up a polarized electron in an optically pumped rubidium vapor cell. A superconducting solenoid generates a strong magnetic field that splits the energy levels of the rubidium atoms by Zeeman effect. A laser at 795 nm is used to pump the external electron of all the rubidium atoms into the same spin state. The polarization is then transferred to the proton in the Sona transition region using suitable perturbing fields. The resulting polarized hydrogen atoms are negatively ionized in a sodium-jet vapor cell. The ensuing beam of H^- ions leaves the source at an energy of 35 KeV with a polarization estimated around 85 to 90% [9].

The ions are then accelerated to 200 MeV through a 140 m DTL-type[1] linac. Various beam diagnostic devices are installed at the end of the linac, including a polarimeter to continuously monitor the polarization of the beam delivered by the source. The measured polarization of the beam at this location is today typically around 82 % [10], although this value depends on the intensity provided by the source. The beam then goes through the LtB[2] transfer line and is injected in the Booster using a continuous injection scheme by stripping the hydrogen ions from their two electrons at the end of the LtB. The injection typically lasts for $\sim 300\mu$s.

The Booster is a synchrotron with a FODO-type lattice and a circumference of 201.7 m. The coasting beam is captured within a single proton bunch and accelerated to an energy of 2.4 GeV or $G\gamma = 4.5$ where G is the anomalous g-factor of the proton and γ the Lorentz factor. Acceleration is achieved using an RF harmonic number of $h = 2$ and takes approximatively 90 ms [11].

Acceleration of polarized protons imposes particular manipulations in order to preserve the beam polarization. While the extraction occurs at $G\gamma = 4.5$ the vertical tune is kept around $Q_y = 4.85$ to avoid intrinsic spin resonances. Imperfection spin resonances at $G\gamma = 3$ and $G\gamma = 4$ are fully overcome by spin flipping or by the harmonic correction of the vertical orbit. The polarization of the proton beam is fully preserved during its acceleration through the Booster without the use of

[1] Drift Tube Linac
[2] Linac to Booster

specialized devices. The BtA[1] transfer line transports the bunched beam to the next acceleration stage: the AGS.

The AGS is the second synchrotron of the RHIC chain. Based on a FODO-type cell, it is four times the size of the previous accelerator with a circumference $C = 807\,\text{m}$. The lattice is composed of 12 super-periods labeled from A to L, the starting point defined as the first magnet following the inflector of the injection system. Each super-period is composed of 20 combined function main magnets[2] featuring both dipole and quadrupole fields and marked from 1 to 20. Each main magnet is identified by the letter of its super-period followed by the position in the super-period. Every straight section is named after the upstream main magnet. Figure 1.1 shows several devices specifically used in the polarized proton configuration of the AGS. Two specialized magnets called partial Siberian snakes are used to preserve the polarization: a superconducting version is installed in the A20 straight section, while a weaker normal conducting version is installed in the E20 straight section. The AGS pC polarimeter[3] is located in the C15 straight section and is used to measure the beam's polarization. The layout and use of the specific equipment is detailed in Chapter 3.

A single proton bunch is captured at injection using an RF harmonic number of $h = 8$ and accelerated to 23.8 GeV or $G\gamma = 45.5$ within approximatively 400 ms. The single bunch is then extracted to the AtR[4] transfer line, toward the last accelerator of the complex: the RHIC collider.

Polarization measurements in the AGS are particularly complex and need to be calibrated. While an absolute polarimeter based on a polarized hydrogen jet is located in the RHIC ring and used to calibrate the AGS polarimeter at the AGS extraction energy, no absolute measurement of

[1] Booster to AGS

[2] The lattice is similar to the CERN Proton Synchrotron where the number of main magnets is 200 instead of 240 for the AGS. The AGS was commissioned 8 months after the PS in July 1960 but at a higher maximum proton energy of 33 GeV versus 29.5 GeV for the CERN PS [12].

[3] Makes use of the proton-Carbon scattering asymmetry to measure the polarization of the beam [13].

[4] AGS to RHIC

the beam polarization during its acceleration is possible. Details regarding the AGS polarization measurement can be found in appendix D. Optimization of the accelerator is also complex since no measurement of the polarization losses along the acceleration cycle is possible. This is the main motivation to simulate in detail the polarization transport and losses along the AGS cycle.

The RHIC is a circular accelerator but also a collider storage ring with a circumference of 3.8 km. Composed of two independent beam pipes, it allows the circulation of different species counter-rotating at different rigidities. The two pipes cross in 6 locations, defining 6 arcs between the crossing points (IP). Each arc is made of 11 regular FODO cells of superconducting magnets cooled at 4 K, with a maximum dipole field of ~ 3.5 T [14].

Figure 1.1 displays the role of the different interaction points. The two beams collide at locations 6 and 8 where the experiments STAR and PHENIX respectively record the events. Spin rotators are placed on both sides of the experiments to switch the direction of the polarization in the longitudinal direction prior to collisions without altering it elsewhere. Two full Siberian snake magnets per ring are also used for the polarized proton collisions and acceleration. The hydrogen jet polarimeter measures the absolute polarization of the beams, while the pC polarimeters are used as fast relative polarization measurement devices. Being faster, they are also critical for operation and tuning of the accelerator [13].

In the polarized proton configuration, the RHIC accelerates 111 bunches per ring to an energy of $E = 254.9$ GeV with a usual intensity of $1.8\,10^{11}$ particles per bunch. The average polarization of the beam during the 2013 Run reached 52% [15].

1.3 Recent and Future Developments of the RHIC Complex

The RHIC complex is also famous for its research program in accelerator physics, particularly concerning the development and implementation of new technologies improving the RHIC perfor-

mance. Some of the most important ongoing projects on the RHIC ring include the e-lens project in IP10, the proof of principle of the coherent electron cooling in IP2 and the spin-flipper in IP4.

The e-lens will compensate for the head-on beam-beam effect generated by the interaction of the proton beams at the PHENIX experiment and will allow an increase of the maximum bunch intensity, hence increasing the luminosity achieved in polarized proton collisions [16]. The coherent electron cooling will be used to reduce the hadron beam emittance and increase the collision rates for the future eRHIC electron ion collide [17]. The spin-flipper will be used to reverse the spin direction during a physics store to cancel the systematic errors for the spin physics experiments [18].

As the first and only facility to accelerate polarized protons to hundreds of GeV, RHIC is a unique machine. While the last 10 years saw numerous technologies being developed and successfully implemented at the RHIC complex to produce and improve the polarized proton beam, many projects are ongoing to carry on this effort. The coming years will see a dramatic increase in both intensity and polarization of the polarized proton beam driven by RHIC improvements and the development and optimization of the injector chain, particularly in the AGS. We expect intensities of 3.10^{11} per bunch, with an average polarization of 65 % to 70 % at $E = 255$GeV to be possible in the next few years.

Numerous other projects are being carried out at the RHIC complex to develop different branches of accelerator physics, from medical applications [19] to the next generation electron ion collider [20], as well as plasma acceleration [21]. A lot of efforts are also being made at BNL to promote accelerator science and help reach a broader audience, including future potential researchers from local schools and universities.

Chapter 2

Theory of Beam and Spin Dynamics

Basic theory of beam dynamics will be developed and applied to the special case of the AGS. Then spin dynamics will be presented and we will review the history of polarized protons acceleration in the AGS to the light of the basic theory of beam and spin dynamics.

2.1 Transverse Dynamics

The motion of a charged particle in an electromagnetic field is governed by the Lorentz force:

$$\frac{\mathrm{d}\vec{p}}{\mathrm{d}t} = q(\vec{E} + \vec{v} \times \vec{B}) \tag{2.1}$$

where:

- $\vec{p} = \gamma m_0 \vec{v}$ is the momentum of the particle with m_0 its rest mass, γ the Lorentz parameter and $\vec{v}$ the velocity. We also define p and v as the norms of the momentum and velocity.
- q is the charge of the particle.
- $\vec{E}$ and $\vec{B}$ are, respectively, the electric and magnetic fields.

2.1.1 Equations of Motion in a Curvilinear Coordinate System

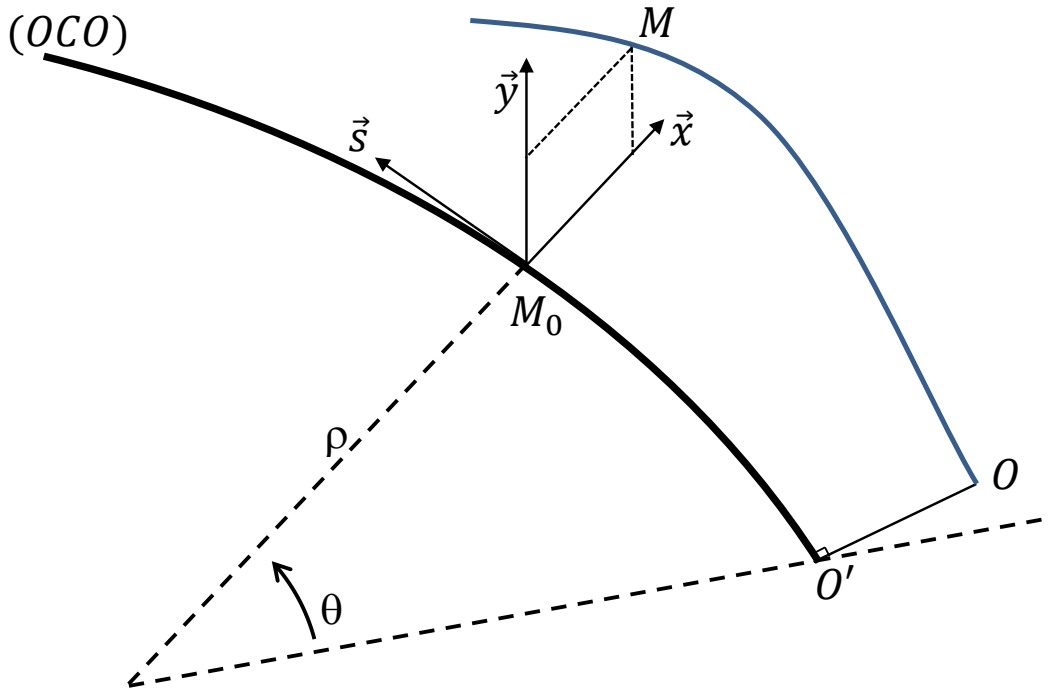

Figure 2.1 Serret-Frenet coordinate system (x,s,y).

The AGS uses a circular lattice composed of a series of magnets ideally aligned in the horizontal plane defining the AGS lattice. The basic layout is defined by the AGS main magnets that create the curvature of the orbit. It is convenient to describe all fields in the same reference frame. For this we use a system (x,s,y) attached to a trajectory of reference called the *OCO*[1] and connected to the reference particle of momentum p_0 (Fig. 2.1). Both the *OCO* and p_0 are fundamental to the AGS and clearly defined [22, 23]. The *OCO* is a straight line outside the main magnets and goes through the magnetic center of every element. In the main magnets the OCO can be defined as a curve of constant radius of curvature ρ_0 in the field $\vec{B} = B_0\vec{y}$ [23]. The dipole field B_0 is defined in the AGS as the mean vertical field along the reference trajectory in a main magnet.

The referential (x,s,y) is used to describe the particle motion and the fields encountered. One

[1] Optimum Closed Orbit

can locally consider a cylindrical coordinate system (r,θ,y) by defining [24]:

$$r = \rho + x\,, \quad \frac{\mathrm{d}\theta}{\mathrm{d}s} = \frac{1}{\rho} \quad \text{and} \quad \theta = \int_0^s \frac{\mathrm{d}s}{\rho} \tag{2.2}$$

In the case of a straight section we have $\rho \to \infty$ and the referential (x,s,y) transforms into a Cartesian coordinate system [25].

The point O is the origin of the particle trajectory and is fixed relative to the OCO. In the AGS the position O' of the projection of O on the OCO is the origin of the lattice and taken at the magnetic face entrance edge of the first main magnet (Fig. 2.4). We also define:

- M_0 the projection of M on the OCO
- $\overrightarrow{OM} = \vec{r} = \overrightarrow{OM_0} + x\vec{x} + y\vec{y}$
- $\vec{s} = \dfrac{\mathrm{d}\overrightarrow{O'M_0}}{\mathrm{d}s}$
- s the longitudinal coordinate of M_0 from O'

The (x,s,y) coordinate system is a Serret-Frenet coordinate system. In this system the directional derivatives of the base unit vectors are:

$$\frac{\mathrm{d}\vec{x}}{\mathrm{d}s} = \frac{\vec{s}}{\rho} \quad , \quad \frac{\mathrm{d}\vec{s}}{\mathrm{d}s} = -\frac{\vec{x}}{\rho} \quad \text{and} \quad \frac{\mathrm{d}\vec{y}}{\mathrm{d}s} = 0 \tag{2.3}$$

And using Newton's notation of the time derivatives, where $\dot{s} = \dfrac{\mathrm{d}s}{\mathrm{d}t}$ is the speed of M_0, we write the time derivatives of the base vectors:

$$\frac{\mathrm{d}\vec{x}}{\mathrm{d}t} = \frac{\dot{s}}{\rho}\vec{s} \quad , \quad \frac{\mathrm{d}\vec{s}}{\mathrm{d}t} = -\frac{\dot{s}}{\rho}\vec{x} \quad \text{and} \quad \frac{\mathrm{d}\vec{y}}{\mathrm{d}t} = 0 \tag{2.4}$$

Using the expression of $\vec{r}$ in the Serret-Frenet coordinate system its time derivatives can be written:

$$\vec{v} = \frac{\mathrm{d}\vec{r}}{\mathrm{d}t} = \begin{pmatrix} \dot{x} \\ \dot{s}\left(1+\frac{x}{\rho}\right) \\ \dot{y} \end{pmatrix} \quad \text{and} \quad \frac{\mathrm{d}\vec{v}}{\mathrm{d}t} = \begin{pmatrix} \ddot{x} - \dot{s}^2 \frac{1}{\rho}\left(1+\frac{x}{\rho}\right) \\ \ddot{s}\left(1+\frac{x}{\rho}\right) + 2\dot{s}\frac{\dot{x}}{\rho} + \dot{s}x\left(\dot{\frac{1}{\rho}}\right) \\ \ddot{y} \end{pmatrix} \tag{2.5}$$

The AGS only uses magnetic elements to guide the particles, and the electric field of equation 2.1 is discarded for now. Therefore we can rewrite equation 2.1 in the Serret-Frenet system using equations 2.5:

$$\begin{pmatrix} \ddot{x} - \dot{s}^2 \frac{1}{\rho}\left(1+\frac{x}{\rho}\right) \\ \ddot{s}\left(1+\frac{x}{\rho}\right) + 2\dot{s}\frac{\dot{x}}{\rho} + \dot{s}x\left(\dot{\frac{1}{\rho}}\right) \\ \ddot{y} \end{pmatrix} = \frac{qv}{p} \begin{pmatrix} \dot{s}\left(1+\frac{x}{\rho}\right)B_y - \dot{y}B_s \\ \dot{y}B_x - \dot{x}B_y \\ \dot{x}B_s - \dot{s}\left(1+\frac{x}{\rho}\right)B_x \end{pmatrix} \tag{2.6}$$

The magnetic field is expressed in the (x,s,y) system so that $\vec{B} = B_x\vec{x} + B_s\vec{s} + B_y\vec{y}$. In the AGS the magnetic field can always be considered as constant in time since the revolution period for protons is around $3\,\mu$s, much faster than the typical time considered to change the field in magnetic elements (in the order of the millisecond) [26]. Nonetheless, the field varies along the *OCO*. It is therefore convenient to change variables, from the time t to the longitudinal coordinate s. All quantities depending on the lattice, such as the magnetic field $\vec{B}$ or the curvature of the trajectory ρ, are now a function of s. Using equations 2.4 and Lagrange's notation of the longitudinal derivative $\frac{\mathrm{d}*}{\mathrm{d}s} = *'$ we obtain:

$$\begin{aligned} \dot{x} &= x'\dot{s} \qquad \text{and} \qquad \dot{y} = y'\dot{s} \\ \ddot{x} &= x''\dot{s}^2 + x'\ddot{s} \qquad \text{and} \qquad \ddot{y} = y''\dot{s}^2 + y'\ddot{s} \end{aligned} \tag{2.7}$$

Then using 2.4 and 2.7 we can rewrite 2.6, the equations of motion in the transverse planes as:

$$x'' - \frac{1}{\rho(s)}\left(1+\frac{x}{\rho(s)}\right) + x'\frac{\ddot{s}}{\dot{s}^2} = \frac{q}{p}\frac{v}{\dot{s}}\left[\left(1+\frac{x}{\rho(s)}\right)B_y(s) - y'B_s(s)\right] \tag{2.8}$$

$$y'' + y'\frac{\ddot{s}}{\dot{s}^2} = -\frac{q}{p}\frac{v}{\dot{s}}\left[\left(1+\frac{x}{\rho(s)}\right)B_x(s) - x'B_s(s)\right] \tag{2.9}$$

with:

$$\frac{v}{\dot{s}} = \sqrt{\left(1+\frac{x}{\rho(s)}\right)^2 + x'^2 + y'^2} \quad \text{and} \quad \frac{\ddot{s}}{\dot{s}^2} = -\frac{1}{2}\left[\frac{\frac{\mathrm{d}}{\mathrm{d}s}\left(\frac{v}{\dot{s}}\right)^2}{\left(\frac{v}{\dot{s}}\right)^2}\right] \tag{2.10}$$

2.8 and 2.9 rule the particle motion in the transverse planes, but in order to solve these equations we need to make approximations. We will expand the magnetic field around the OCO in the (x,s,y) system, then we will use the linear part of the equation of motion to establish a linear approximate solution of the transverse motion.

2.1.1.1 Field Expansion in the Serret-Frenet Coordinate System Around the OCO

In the ideal case the AGS magnetic elements are centered on the OCO, which is in the horizontal plane. The magnetic field is antisymmetric relative to the plane $y=0$ and we also have $B_x = B_s = 0$ in the median plane. Using this symmetry and Maxwell's equations we expand the magnetic field in the Serret-Frenet coordinate system and obtain [24]:

$$B_x(s) = \frac{p}{q}\left[k_1(s)y + k_2(s)xy + \ldots\right] \tag{2.11}$$

$$B_s(s) = \frac{p}{q}\left[k_0'(s)y + \alpha'(s)xy + \ldots\right] \tag{2.12}$$

$$B_y(s) = \frac{p}{q}\left[k_0(s) + k_1(s)x + \frac{1}{2}k_2(s)x^2 - \frac{1}{2}\beta(s)y^2 + \ldots\right] \tag{2.13}$$

with:

$$\alpha(s) = \frac{1}{2}k_0^2(s) + k_1(s) \quad \text{and} \quad \beta(s) = k_0''(s) - k_0(s)k_1(s) + k_2(s) \tag{2.14}$$

where the field is expanded up to its sextupole component:

$$k_0(s) = \frac{q}{p}B_y(s) = -\frac{1}{\rho(s)} \qquad \text{dipole} \tag{2.15}$$

$$k_1(s) = \frac{q}{p}\frac{\mathrm{d}B_y(s)}{\mathrm{d}x} \qquad \text{quadrupole} \tag{2.16}$$

$$k_2(s) = \frac{q}{p}\frac{\mathrm{d}^2B_y(s)}{\mathrm{d}x^2} \qquad \text{sextupole} \tag{2.17}$$

We call k the normalized field strength and it directly characterizes the effect of the field on the particle. Also, using equation 2.15 with a constant vertical magnetic field B_0 we have:

$$B_0\rho_0 = -\frac{p_0}{q} \tag{2.18}$$

where ρ_0 is a constant defined for the AGS as $\rho_0 = 85.38084\,\mathrm{m}$ [23]. The product of the field B_0 by the trajectory radius of curvature is used to characterize the particle or beam momentum. We define the magnetic rigidity $B\rho$:

$$B\rho = -\frac{p_0}{q} \quad \text{or} \quad B\rho = -\frac{p}{q} \tag{2.19}$$

The magnetic rigidity characterizes the ease of bending the trajectory of a particle in a magnetic field.

2.1.1.2 Linear Equations of Motion in the Serret-Frenet Coordinate System

The AGS was designed to operate using the main magnets alone. Furthermore the AGS main magnets are combined function dipoles featuring dipole and quadrupole fields with a small sextupole error [27]. We will neglect for now the sextupole component and only retain the linear terms in the

x and y components of the magnetic field. Equations 2.11 to 2.13 become:

$$B_x(s) \approx -B\rho k_1(s)y \tag{2.20}$$

$$B_s(s) \approx 0 \tag{2.21}$$

$$B_y(s) \approx -B\rho\left(k_0(s)+k_1(s)x\right) \tag{2.22}$$

By taking only linear terms in equations 2.10 we get:

$$\frac{v}{\dot{s}} \approx \left(1+\frac{x}{\rho(s)}\right) \quad \text{and} \quad \frac{\ddot{s}}{\dot{s}^2} \approx 0 \tag{2.23}$$

We also consider small variations of the particle momentum p around the reference momentum p_0 of the particle on the OCO, as we define $p = p_0 + \Delta p$ with $\Delta p \ll p_0$. By expanding $1/p$ for small $\Delta p/p_0$ in Taylor's series and keeping only the first two terms of the expansion we get:

$$\frac{1}{p} = \frac{1}{p_0}\left(1-\frac{\Delta p}{p_0}+\left(\frac{\Delta p}{p_0}\right)^2+[\ldots]\right) \approx \frac{1}{p_0}\left(1-\frac{\Delta p}{p_0}\right) \tag{2.24}$$

Using the equations above and by taking only linear terms in x, y and Δp, equations 2.8 and 2.9 take the form:

$$x'' - \left(k_1(s)-\frac{1}{\rho^2(s)}\right)x = \frac{1}{\rho(s)}\frac{\Delta p}{p_0} \tag{2.25}$$

$$y'' + k_1(s)y = 0 \tag{2.26}$$

Equations 2.25 and 2.26 describe the trajectory in the linear approximation in the curvilinear coordinate system (x,s,y). In the linear approximation, the motion in the two planes appear to be

Table 2.1 Forms of the focusing term in the most common types of elements.

Element	$K_x(s)$	$K_y(s)$
Pure dipole	$\rho^{-2}(s)$	0
Pure quadrupole	$-k_1(s)$	$k_1(s)$
Combined function dipole	$\rho^{-2}(s)-k_1(s)$	$k_1(s)$
Drift	0	0

independent. Equations 2.25 and 2.26 can be written in a more general form:

$$z''+K_z(s)z=\frac{1}{\rho(s)}\frac{\Delta p}{p_0} \tag{2.27}$$

where z stands for x or y and $K_z(s)$ takes different forms depending on the magnetic element considered (Tab. 2.1). In the vertical plane the radius of curvature is infinite and the right hand side of equation 2.27 vanishes. In the general case $K_z(s)$ varies with s periodically along the ring and the equation 2.27 is of Hill's type. The general solution to equation 2.27 can be written [24]:

$$z(s) = C_z(s)z_0+S_z(s)z_0'+D_z(s)\frac{\Delta p}{p_0} \tag{2.28}$$

$$z'(s) = C_z'(s)z_0+S_z'(s)z_0'+D_z'(s)\frac{\Delta p}{p_0} \tag{2.29}$$

where $z'(s)$ is the angle between $\vec{s}$ and the projection of $\vec{v}$ in the plane $(\vec{s},\vec{z})$. The functions $C_z(s)$ and $S_z(s)$ are independent solutions for the homogeneous equation associated with 2.27. The function $D_z(s)$ is a particular solution of the inhomogeneous equation. It characterizes the chromatic effect of the magnetic elements and is called the dispersion function.

The linear transformation expressed by equations 2.28 and 2.29 can be written in a matrix form:

$$\begin{pmatrix} z(s) \\ z'(s) \\ \frac{\Delta p}{p_0} \end{pmatrix} = \begin{pmatrix} C_z(s) & S_z(s) & D_z(s) \\ C'_z(s) & S'_z(s) & D'_z(s) \\ 0 & 0 & 1 \end{pmatrix} \begin{pmatrix} z(0) \\ z'(0) \\ \frac{\Delta p}{p_0} \end{pmatrix} = T_z \begin{pmatrix} z(0) \\ z'(0) \\ \frac{\Delta p}{p_0} \end{pmatrix} \tag{2.30}$$

where T_z is the transfer matrix between entrance (0) and exit (s). The particular case of the transfer matrix associated to the AGS main magnets will be described in Chapter 3.

While the method described above allows to transport the coordinates of a particle through one or more elements, another way to express the motion along the OCO is to parametrize the motion in terms of amplitude and phase functions.

2.1.2 Twiss Parametrization of the Transverse Motion

If we consider the reference particle for which $\Delta p = 0$, 2.27 can be written:

$$z'' + K_z(s)z = 0 \tag{2.31}$$

The AGS being a circular machine, the restoring force term $K_z(s)$ is necessarily a periodic function of, at most, the machine circumference, *i.e.* $K_z(s) = K_z(s + C_0)$ with C_0 the length of the OCO over a full turn. Solution to the Hill's equation is established using the Floquet's theorem. The trajectory takes a quasi-harmonic form [24]:

$$z(s) = \sqrt{\varepsilon_z/\pi}\sqrt{\beta_z(s)}\cos\left(\mu_z(s) - \mu_z(0)\right) \tag{2.32}$$

where the amplitude $\beta_z(s)$ and phase $\mu_z(s)$ terms are respectively called the betatron (or "beta") function and the betatron phase. We also introduce ε_z, an invariant of the motion [26]. The motion described by the particle is usually referred as the betatron motion. The evolution of the phase

term can be expressed as:

$$\mu_z(s) = \int_0^s \frac{\mathrm{d}\sigma}{\beta_z(\sigma)} \tag{2.33}$$

By differentiation of equation 2.32 we find:

$$z'(s) = -\frac{\sqrt{\varepsilon_z}/\pi}{\sqrt{\beta_z(s)}}\left[\sin\left(\mu_z(s) - \mu_z(0)\right) + \alpha_z(s)\cos\left(\mu_z(s) - \mu_z(0)\right)\right] \tag{2.34}$$

where:

$$\alpha_z(s) = -\frac{1}{2}\frac{\mathrm{d}\beta_z(s)}{\mathrm{d}s} \tag{2.35}$$

We also define the function:

$$\gamma_z(s) = \frac{1+\alpha_z(s)^2}{\beta_z(s)} \tag{2.36}$$

The beta function together with equations 2.35 and 2.36 are called the Twiss functions. The Twiss functions retain the same periodicity as the lattice.

An important quantity for circular machines such as the AGS is the number of betatron oscillations per turn: the betatron tune Q_z. It can be expressed from equation 2.33 and using $s = C_0$:

$$Q_z = \frac{1}{2\pi}\mu_z(C_0) \tag{2.37}$$

Equations 2.32 and 2.34 describe the equation of an ellipse in the plane (z, z') at a given azimuth s. Therefore the particle positions in the (z, z') phase space turn after turn, are on an ellipse. Figure 2.2 shows the trajectory of a single particle motion in (z, z') and the relations between the maximum excursions on z or z' and the Twiss functions.

Additionally, the Liouville's theorem states that the area delimited by the particle in Figure 2.2 is conserved around the accelerator lattice. The parametric equation associated to the ellipse in

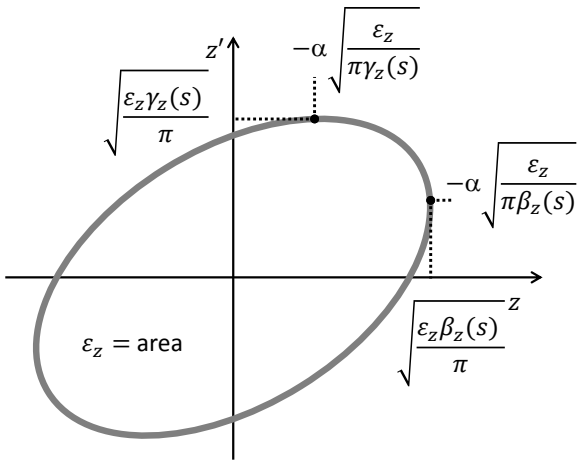

Figure 2.2 Representation of a particle trajectory in the (z, z') phase space.

Figure 2.2 is usually called the Courant-Snyder invariant of the particle and has the form:

$$\frac{\varepsilon_z}{\pi} = \gamma_z(s)z^2 + 2\alpha_z(s)zz' + \beta_z(s)z'^2 \tag{2.38}$$

We also define the normalized invariant $\varepsilon_{z,N}$ to account for the adiabatic damping of the transverse motion during acceleration:

$$\varepsilon_{z,N} = \varepsilon_z \beta\gamma \tag{2.39}$$

with $\beta = v/c$. This invariant does not change with the energy.

2.1.2.1 Betatron and Coupling Resonances

While we have considered a perfect machine until now, one has to understand the implications of errors on the beam dynamics. Lets consider N localized transverse deflections of the beam (or transverse kicks) of magnitude θ_i at azimuth s_i. These can be attributed not only to errors in the main magnets, but also to misalignments in other quadrupole or sextupole magnets. We can also use dedicated low field dipole magnets located in some of the AGS straight sections to deliberately create transverse kicks. This results in the distortion of the closed orbit, with respect to the OCO.

The distortion at s is given by [28]:

$$\Delta z(s) = \frac{\sqrt{\beta_z(s)}}{2\sin(\pi Q_z)} \sum_{i=1}^{N} \theta_i \sqrt{\beta_z(s_i)} \cos\left(|\mu_z(s) - \mu_z(s_i)| - \pi Q_z\right) \tag{2.40}$$

If $Q_z = p$ with p an integer, the term in front of the sum tends toward infinity. This is called an integer resonance and in that condition, the closed orbit is undefined. Integer values of the tune have to be avoided at any time.

We can now study the effect of localized gradient errors. We consider N integrated quadrupole errors $(\Delta k_1 l)_i$ at s_i. In the AGS these can be caused by orbit displacements in sextupoles or by field errors in quadrupole or main magnets. The resulting error in the beta function $\Delta\beta_z(s)$ along the AGS is [28]:

$$\frac{\Delta\beta_z(s)}{\beta_z(s)} = \frac{1}{2\sin(2\pi Q_z)} \sum_{i=1}^{N} (\Delta k_1 l)_i \beta_z(s_i) \cos\left(2|\mu_z(s) - \mu_z(s_i)| - 2\pi Q_z\right) \tag{2.41}$$

In this case the error in the beta function diverges when $Q_z = 2p$ with p an integer. This is called a half integer resonance and the beam envelopes are undefined. The half integer values of the tune need to be avoided.

We have developed the equations of the transverse motion in the approximation of uncoupled motion between the two transverse planes. However, coupling can arise from errors in the main magnets or quadrupole magnets. In the approximation of a weak coupling between the two planes, conditions were established on the transverse tunes for the motion to be stable. It was showed that the integer values of the tune sum, $Q_x + Q_y = p$, lead to instability whereas for integer tune differences ($Q_x - Q_y = p$), the motion remains stable [26].

Non-linear resonances driven by non-linear multipole fields also exist. A general expression of

all the betatron resonances can be written:

$$lQ_x + mQ_y = p \tag{2.42}$$

where l, m and p are integers. We define the resonance order $n = |l| + |m|$. Lower order resonances are generally the most dangerous and need to be avoided as much as possible. As for the linear case, sum resonances are unstable whereas difference resonances are stable [29].

2.1.2.2 Dispersion Function in the Motion Parametrization

We removed the chromatic term in equation 2.31 to find Hill's equation. We can reintroduce it in equations 2.32 and 2.34 to obtain the full linear form of the transverse motion, in terms of phase and amplitude:

$$z(s) = \sqrt{\varepsilon_z/\pi}\sqrt{\beta_z(s)}\cos\left(\mu_z(s) - \mu_z(0)\right) + \frac{\Delta p}{p_0}D_z(s) \tag{2.43}$$

$$z'(s) = -\frac{\sqrt{\varepsilon_z/\pi}}{\sqrt{\beta_z(s)}}\left[\sin\left(\mu_z(s) - \mu_z(0)\right) + \alpha_z(s)\cos\left(\mu_z(s) - \mu_z(0)\right)\right] + \frac{\Delta p}{p_0}D'_z(s) \tag{2.44}$$

It is important to note from equation 2.27 that in the vertical plane $\rho(s) \to \infty$, the inhomogeneous term vanishes and the functions $D_z(s)$ and $D'_z(s)$ in the equations above are equal to zero. This is true within the approximations used above, in the absence of coupling between the two transverse planes. We can also see from equation 2.43 that the betatron oscillation now occurs around $\frac{\Delta p}{p_0}D_z(s)$ and no longer around the *OCO* or the on-momentum closed orbit. The particle oscillates around the chromatic closed orbit.

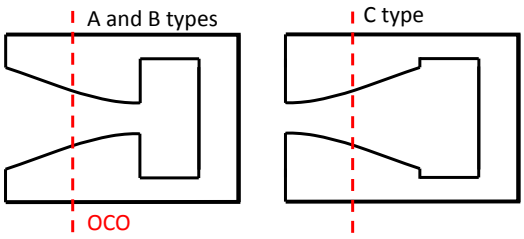

Figure 2.3 Drawing of the AGS main magnets cross section.

2.1.2.3 Natural Chromaticity

The chromatic term also has an important effect on the tune. We define the chromaticity denoted Q'_z as the change in tune ΔQ_z corresponding to a change in the particle momentum of Δp.

$$Q'_z = \frac{\Delta Q_z}{\Delta p / p_0} \tag{2.45}$$

Equation 2.16 shows that the focusing term, hence the strength of the focusing, decreases when the particle momentum p increases. This causes an intrinsic chromaticity also called the natural chromaticity. We will see in Section 2.1.3.2 that the chromaticity of the AGS can be controlled by sextupole magnets.

2.1.3 The AGS Lattice

The AGS uses combined function main magnets featuring both dipole and quadrupole fields. Table 2.2 summarizes the relevant optical parameters of the AGS. Two different magnet cross-sections leading to six different types of magnets are used in the AGS. Figure 2.3 shows the cross section of the magnets. The A and C magnets are 90 inches long while the B magnets are shorter with 75 inches. Although these lengths are the physical lengths of the magnets, we preferentially use their effective length defined as being longer by 4 inches [30]. Every magnet can be of defocusing or focusing effect on the beam by changing its orientation. We define the magnet function by its

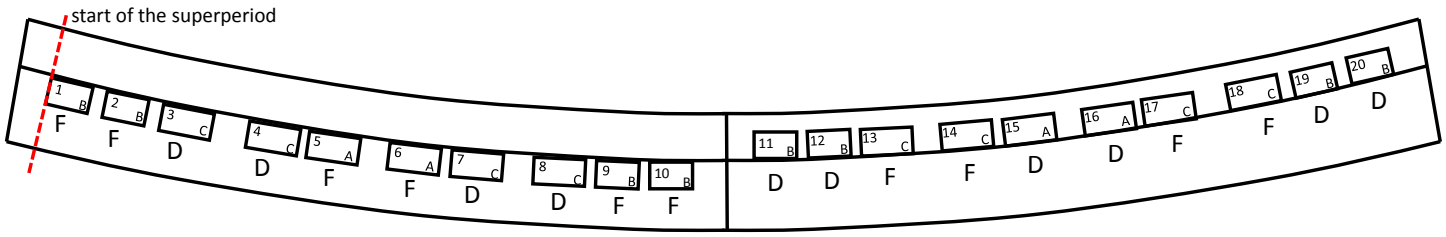

Figure 2.4 Synoptic drawing of one AGS superperiod with the opened side of each magnet facing the centerline. Magnet number, type and function is also labeled. The start of the superperiod is by convention at the magnetic edge of the first main magnet.

effect on the horizontal plane, *e.g.* C magnet is focusing when the open side faces the outside of the ring and the inverse is true for A or B magnets. Figure 2.4 shows the basic layout of the AGS superperiod. The superperiod is made of 5 FODO cells and 20 main magnets. The open sides are oriented toward the center of the ring in the first half of the superperiod and toward the outside in the second half.

The AGS lattice is defined by only two types of elements: the main magnets and the straight sections. A numbering system was established to locate any element in the lattice by using the letter associated to the superperiod followed by the main magnet number (see page 5). For instance, the 5^{th} main magnet of the 3^{rd} superperiod is labeled "MM C05" and the downstream straight section is called "SS C05".

Figure 2.5 shows the position of the long straight sections. Straight sections in positions 10 and 20 are 10 feet long, while the others are 5 feet long. The straight sections not mentioned in Figure 2.5 are only 24 inches long and usually only host BPMs[1], pumping stations or low field dipoles used for orbit correction. Figure 2.5 identifies the location of some devices used to operate the AGS. The horizontal and vertical tunes are controlled by two families of quadrupoles. In the straight sections 03 are located quadrupoles to control the vertical tune, while straight sections 17 host quadrupoles to control the horizontal tune. The 10-foot straight sections are mainly used for extraction/injection lines or RF cavities to accelerate the beam. However, straight sections A20 and

[1]Beam Position Monitors

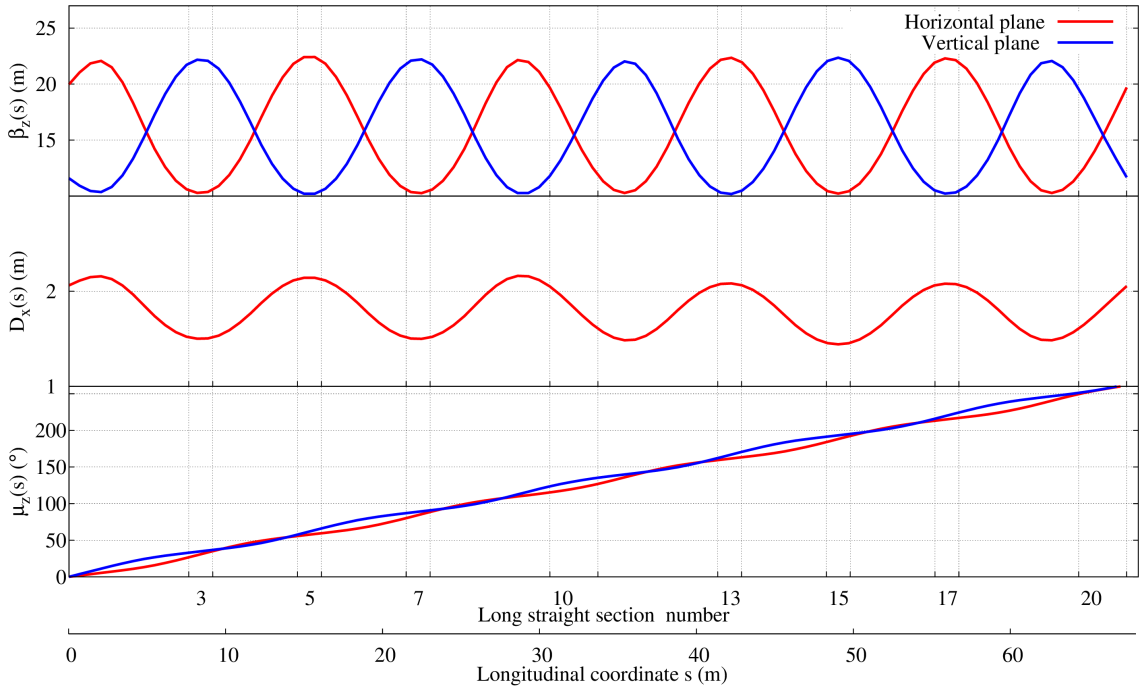

Figure 2.5 Graphic of the beta functions and horizontal dispersion along one AGS superperiod. The last plot shows the evolution of the phase advance in the two transverse planes along the superperiod.

E20 are hosting special magnets called Siberian snakes used to manipulate the proton spin during polarized proton operations.

Table 2.2 Relevant optical and RF parameters of the AGS, at the polarized proton extraction energy.

Paramter		Value
Energy (total)	E	23.8 GeV
Circumference	C	807.091 m
Horizontal tune	Q_x	8.69
Vertical tune	Q_y	8.73
Revolution frequency	f_{rev}	372 kHz
RF harmonic number	h	8
Maximum dipole field ramping rate	$\dot{B}_{max}$	$\approx 2.5\,\mathrm{T.s}^{-1}$
Maximum total RF voltage	$\hat{V}_{RF}$	$\approx$ 280 kV
Gamma transition	γ_{tr}	8.5
Synchrotron tune	Q_s	3.4

2.1.3.1 Tune Control in the AGS

The AGS main magnets feature both dipole and quadrupole fields. As such the transverse tunes of the AGS are fixed by design. However, it is very important to accurately control the transverse tunes. Looking at the effect of a single small gradient error $(\Delta k_1 l)_i$ at the location s_i the resulting variation of the tune δQ_z is [28]:

$$\delta Q_z = -\frac{\beta_z(s_i)}{4\pi}(\Delta k_1 l)_i \tag{2.46}$$

The AGS uses two families of quadrupoles located in regions where either the vertical or horizontal beta function reaches a maximum value. In each superperiod the straight sections 03 and 17, respectively, host the vertical and horizontal high field tune quadrupoles, commonly called tune quads.

2.1.3.2 Chromaticity Control in the AGS

While the natural chromaticity is intrinsic to the AGS we can use sextupole magnets to control the total chromaticity. In the case of a series of sextupole magnet of length l and integrated sextupole strength $(k_2 l)_i$ at locations s_i, the resulting change in chromaticity is:

$$\Delta Q'_z = -\frac{1}{4\pi}\beta_z(s_i)D_x(s_i)(k_2 l)_i \tag{2.47}$$

In the AGS, two families of sextupoles are used. The magnets are located in the straight sections 13 and 17, respectively controlling the horizontal and vertical chromaticities.

2.2 Longitudinal Dynamics

While we have seen that the magnetic term of the Lorentz force is used in synchrotrons to guide the trajectory of the particle, we will now focus on the electric term used to accelerate the particle. In synchrotrons the particles are accelerated by longitudinal RF[1] electric field. Resonant cavities are driven by high frequency RF field in order to produce the accelerating field seen by the beam. The energy gained ΔE by the particle across a cavity can be written [31]:

$$\Delta E = qV_{RF}T_a \sin\phi \tag{2.48}$$

where V_{RF} is the RF voltage, ϕ the phase of the field as seen by the particle. The transit time factor T_a takes into account the time variation of the field during the particle travel inside the cavity. In the AGS T_a is very close to 1 so we will ignore it. By convention, the origin of phases is taken at zero crossing of the RF voltage with positive slope.

The AGS contains several cavities, each only increases the beam energy by a small amount and all are synchronized for the particle to arrive at each with the same phase. In the model discussed later, we only consider single RF cavity with an RF voltage equal to the sum of the RF voltage of each cavity. This approximation is valid in the case of the AGS because the phase slip per turn of the particles remains very small [32]. The important quantity will be the energy gained by the particle per turn of the AGS or acceleration rate ΔE_{turn}.

2.2.1 Synchronous Particle

As a synchrotron, the AGS accelerates protons while the magnetic field of the main magnets increases in order to keep the average radius constant. We define the average radius R of the AGS

[1] Radio Frequency

using the circumference C:

$$R = \frac{C}{2\pi} \tag{2.49}$$

In the AGS, the average radius of the closed orbit on the OCO is $R_0 = 128.4525\,\text{m}$. By taking the time derivative of equation 2.18, one can find the required energy gain per turn to conserve a constant average radius R:

$$\Delta E_{turn} = q\rho\dot{B}_0 2\pi R \tag{2.50}$$

We define a synchronous particle traveling on the closed orbit with a momentum p_S called the synchronous momentum. It is important to note that p_s is not necessarily equal to p_0 but can be if the synchronous particle travels on the OCO. If $p_s \neq p_0$ the synchronous particle travels on a chromatic closed orbit. The synchronous particle enters the cavity at the synchronous phase ϕ_s and receives an energy gain given by equation 2.48:

$$\Delta E_{turn} = qV_{RF}\sin\phi_s \tag{2.51}$$

Additionally, the RF frequency f_{RF} is chosen to be an integer multiple of the revolution frequency f_{rev}:

$$f_{RF} = hf_{rev} \tag{2.52}$$

where h is called the harmonic number. In the AGS, the harmonic number currently used for protons is $h = 8$. Equations 2.50 and 2.51 link the evolution of $\dot{B}_0$, V_{RF} and ϕ_s.

In the AGS, the acceleration rate is driven as high as possible in order to reduce polarization losses (Section 2.3.4.1). The acceleration rate is limited by the main magnets power supply to around $\Delta E_{turn} = 170\,\text{keV/turn}$. Figure 2.6 shows the evolution of the main AGS RF parameters during the acceleration of polarized protons.

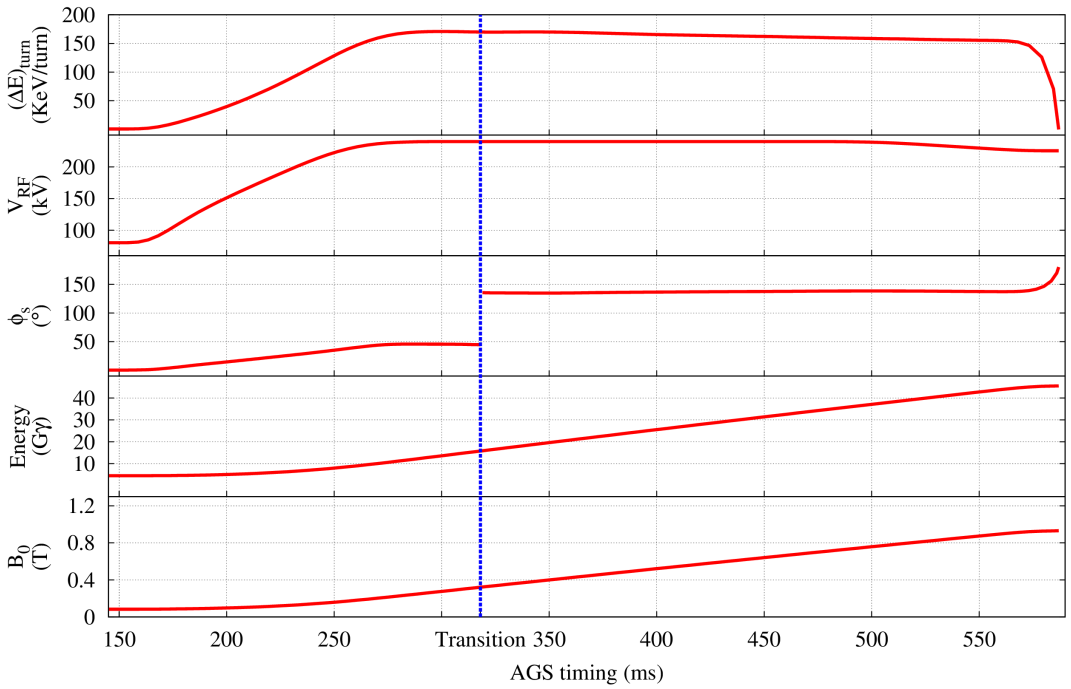

Figure 2.6 Plot of the main RF parameters used for acceleration of polarized protons in the AGS.

2.2.2 Non Synchronous Particle

We will describe the motion of any particle in the longitudinal plane by its deviation from the synchronous one, we define:

$$\begin{aligned} p &= p_s + \Delta p \\ C &= C_s + \Delta C \\ R &= R_s + \Delta R \\ E &= E_s + \Delta E \\ f_{rev} &= f_{rev,s} + \Delta f_{rev} \\ \phi &= \phi_s + \Delta\phi \end{aligned} \tag{2.53}$$

One can see that if $p_s = p_0$ all the "s" indexes in equations 2.53 can be replaced by the index "0". We now define the momentum compaction factor α_p as the variation of the orbit length of a particle for a variation in momentum:

$$\alpha_p = \frac{\Delta C/C}{\Delta p/p} \tag{2.54}$$

We also define η the phase slip factor:

$$\eta = \frac{1}{\gamma^2} - \alpha_p = \frac{1}{\gamma^2} - \frac{1}{\gamma_{tr}^2} \tag{2.55}$$

where γ_{tr} is the transition energy, *i.e.* the energy corresponding to $\eta = 0$. In the AGS, we have $\gamma_{tr} \sim 8.5$. Below the transition energy $\eta > 0$ and particles with higher energy have higher revolution frequency; and above it $\eta < 0$ and particles with lower momentum have higher revolution frequency.

From the equations above one can get a simple form of the differential equation ruling the longitudinal dynamics [31]:

$$\frac{\mathrm{d}^2\phi}{\mathrm{d}t^2} + \Omega_0^2(\sin\phi - \sin\phi_s) = 0 \tag{2.56}$$

where Ω_0 is given by:

$$\Omega_0^2 = \frac{qV_{RF}\eta hc^2}{2\pi R_s^2 E_s} \tag{2.57}$$

2.2.2.1 Small Amplitude Oscillations

We can find a simpler expression if we consider only small amplitude oscillations. We can expand $\sin(\phi_s + \Delta\phi)$ for small $\Delta\phi$ in equation 2.56 and obtain [31]:

$$\frac{\mathrm{d}^2(\Delta\phi)}{\mathrm{d}t^2} + \Omega_s^2\Delta\phi = 0 \tag{2.58}$$

We can see that 2.58 is the differential equation of a harmonic oscillator of angular frequency Ω_s given by:

$$\Omega_s^2 = \Omega_0^2 \cos\phi_s = \frac{qV_{RF}\eta hc^2}{2\pi R_s^2 E_s}\cos\phi_s \tag{2.59}$$

For the longitudinal motion to be stable the squared angular frequency Ω_s^2 needs to be positive. This imposes constraints on the values of the synchronous phase and η:

$$\eta\cos\phi_s > 0 \tag{2.60}$$

Figure 2.6 shows the jump in the synchronous phase during the crossing of the transition energy in order to maintain $\eta\cos\phi_s > 0$. The AGS uses a set of 6 quadrupoles called gamma transition quadrupoles to modify the γ_{tr} of the lattice. The system modifies the momentum compaction factor when the energy gets close to transition in order to accelerate the crossing of the transition.

Similarly to transverse dynamics, we define Q_s the synchrotron tune as the number of synchrotron oscillations per turn of the AGS. In the approximations of this section we have:

$$Q_s = \frac{\Omega_s}{2\pi f_{rev,s}} \tag{2.61}$$

In general, the synchrotron tune can excite synchro-betatron resonances [29] and synchrotron spin resonances [4]. However, the synchrotron tune is very small in the AGS: $Q_s < 10^{-4}$. Therefore the synchrotron motion does not add resonant conditions in the AGS.

2.2.3 RF System in the AGS

Table 2.2 summarizes the relevant RF parameters of the AGS. The AGS RF system is composed of 10 RF stations distributed around the lattice in 10-foot straight sections. Figure 2.7 shows one of the AGS RF stations. Each station contains 4 cavities loaded with a ferrite core. A ferrite core is

Figure 2.7 Picture of the RF station located in the straight section B10 and seen from downstream.

used to reduce the sensitivity of the cavity to the beam loading and to change the cavity frequency during acceleration [33]. Each cavity can provide a RF voltage of up to 7 kV, giving a total ideal RF voltage of around 280 kV.

2.3 Spin Dynamics in a Flat Circular Accelerator

In this section the motion of the spin will be introduced and applied to the case of a flat circular accelerator. The theory of the spin dynamics will be developed for the case of the so called "bare AGS", *i.e.* the AGS comprised of the sole combined function magnets

The spin of the proton is an intrinsic angular momentum and interacts with the magnetic field through the magnetic moment $\vec{\mu}$:

$$\vec{\mu} = g_p \frac{\mu_n}{2} \vec{S} \tag{2.62}$$

where g_p is the Landé g-factor of the proton, μ_n the nuclear magneton and $\vec{S}$ the spin vector. We will use the anomalous g-factor G that characterizes the distance of g_p to the g-factor predicted by the Dirac equation of an electron. In the case of the proton we have:

$$G = \frac{g_p - 2}{2} = 1.7928474 \tag{2.63}$$

Then considering a proton at rest subject to a magnetic field $\vec{B}$ the precession of the spin is governed by:

$$\frac{\mathrm{d}\vec{S}}{\mathrm{d}t} = \vec{\Omega}_S \times \vec{S} = -\frac{g_p e}{2\gamma m_0} \vec{B} \times \vec{S} \tag{2.64}$$

Although the spin is a quantum property its evolution can be described by the precession of the classical vector $\vec{S}$ using the semiclassical spin precession vector $\vec{\Omega}_S$ [4]. We will keep the classical approach of the spin dynamics theory.

2.3.1 Spin Motion of the Reference Particle

Equation 2.64 applies to protons at rest. For a moving particle the transformation of electromagnetic fields in the laboratory frame to the proton rest frame gives the Thomas-BMT equation:

$$\frac{\mathrm{d}\vec{S}}{\mathrm{d}t} = \frac{e}{m_0\gamma}\vec{S}\times\left[(1+G\gamma)\vec{B}_{\perp}+(1+G)\vec{B}_{\parallel}+\left(G\gamma+\frac{\gamma}{\gamma+1}\right)\frac{\vec{E}\times\vec{\beta}}{c}\right] \tag{2.65}$$

with $\vec{\beta}=\vec{v}/c$. We also introduce $\vec{B}_{\perp}$ and $\vec{B}_{\parallel}$, the orthogonal and parallel components of the magnetic field to the particle velocity.

We saw in Section 2.2 that electric fields are only used to accelerate the protons. The electric field is always considered parallel to the particle velocity and $\vec{\beta}\times\vec{E}=0$. The term with the electric field can be removed from equation 2.65.

In the case of the particle traveling on the OCO, only vertical guiding fields are encountered and $\vec{B}=B_0\vec{y}$. This results in the simplest form of the precession of the spin:

$$\vec{\Omega}_S = -\frac{q}{m_0\gamma}(1+G\gamma)B_0\vec{y} \tag{2.66}$$

In these conditions the Lorentz equation can be written [4]:

$$\frac{\mathrm{d}\vec{v}}{\mathrm{d}t} = \vec{\Omega}_c\times\vec{v} \tag{2.67}$$

where $\vec{\Omega}_c$ is the relativistic cyclotron frequency and characterizes the revolution frequency of the particle around the machine. Now it is interesting to compare the cyclotron frequency to the precession frequency of the spin in the same magnetic field.

$$\frac{\Omega_S}{\Omega_C} = 1+G\gamma \tag{2.68}$$

In the rotating frame, the spin makes $G\gamma$ turns around the vertical direction per turn of the AGS. By analogy with the betatron tunes, this defines a very important quantity called the spin tune Q_S. In the case of a circular machine Q_S is the unperturbed spin tune on the *OCO*:

$$Q_S = G\gamma \tag{2.69}$$

In synchrotrons such as the AGS, the spin tune plays a critical role and $G\gamma$ is commonly used as unit of energy.

2.3.2 Spin Motion in the Serret-Frenet Coordinate System

As for the transverse dynamics developed in Section 2.1.1, it is convenient to use the curvilinear coordinate system defined Figure 2.1. We will express $\vec{B}_\perp(s)$ and $\vec{B}_\parallel(s)$ along the OCO in the curvilinear coordinate system (x,s,y). We will neglect all non linear terms in x and y.

We can express the transverse field as:

$$\vec{B}_\perp(s) = \frac{1}{v^2}\left(\vec{v}\times\vec{B}(s)\right)\times\vec{v} \tag{2.70}$$

From equation 2.1 and using equation 2.19 we have:

$$\vec{v}\times\vec{B}(s) = \frac{\gamma m_0}{q}\frac{\mathrm{d}\vec{v}}{\mathrm{d}t} = -B\rho\frac{1}{v}\frac{\mathrm{d}\vec{v}}{\mathrm{d}t} \tag{2.71}$$

Equations 2.5 can be written using the longitudinal derivations of the coordinates from equations

2.7. Then we can use the approximations mentioned on equations 2.23 and write:

$$\vec{v} = \begin{pmatrix} x'\dot{s} \\ \dot{s}\left(1+\frac{x}{\rho(s)}\right) \\ y'\dot{s} \end{pmatrix} \quad \text{and} \quad \frac{\mathrm{d}\vec{v}}{\mathrm{d}t} = \begin{pmatrix} x''\dot{s}^2 + x'\ddot{s} - \dot{s}^2\frac{1}{\rho(s)}\left(1+\frac{x}{\rho(s)}\right) \\ 2\dot{s}^2\frac{x'}{\rho(s)} \\ y''\dot{s}^2 + y'\ddot{s} \end{pmatrix} \approx \begin{pmatrix} x''\dot{s}^2 - \dot{s}^2\frac{1}{\rho(s)}\left(1+\frac{x}{\rho(s)}\right) \\ 2\dot{s}^2\frac{x'}{\rho(s)} \\ y''\dot{s}^2 \end{pmatrix} \tag{2.72}$$

Using the equations above we get:

$$\begin{aligned}
\vec{B}_\perp(s) &\approx -B\rho\frac{1}{v}\frac{1}{\dot{s}^2\left(1+\frac{x}{\rho(s)}\right)^2}\frac{\mathrm{d}\vec{v}}{\mathrm{d}t}\times\vec{v} \\
&= -B\rho\left(1-\frac{x}{\rho(s)}\right)\frac{1}{\dot{s}^3\left(1+\frac{x}{\rho(s)}\right)^2}\begin{pmatrix} 2\dot{s}^3\frac{x'}{\rho(s)}y' - y''\dot{s}^3\left(1+\frac{x}{\rho(s)}\right) \\ y''\dot{s}^3x' - y'\dot{s}^3\left(x'' - \frac{1}{\rho(s)}\left(1+\frac{x}{\rho(s)}\right)\right) \\ \left(x'' - \frac{1}{\rho(s)}\left(1+\frac{x}{\rho(s)}\right)\right)\dot{s}^3\left(1+\frac{x}{\rho(s)}\right) - 2\dot{s}^3\frac{x'^2}{\rho(s)} \end{pmatrix} \\
&\approx -B\rho\left(1-\frac{x}{\rho(s)}\right)\begin{pmatrix} -y''\left(1-\frac{x}{\rho(s)}\right) \\ y'\frac{1}{\rho(s)}\left(1-\frac{x}{\rho(s)}\right) \\ x''\left(1-\frac{x}{\rho(s)}\right) - \frac{1}{\rho(s)} \end{pmatrix} \\
&\approx -B\rho\left(1-\frac{x}{\rho(s)}\right)\begin{pmatrix} -y'' \\ \frac{y'}{\rho(s)} \\ x'' - \frac{1}{\rho(s)} \end{pmatrix}
\end{aligned} \tag{2.73}$$

In the linear approximation, fields parallel to the particle trajectory are due to longitudinal magnetic fields $B_s(s)$ but also to the vertical orbit through vertical magnetic fields (*e.g.* solenoids or dipoles) [34]:

$$\vec{B}_\parallel(s) \approx \left(B_s(s) + y'B_y(s)\right)\vec{s} \tag{2.74}$$

Using Gauss's law for magnetism and equation 2.15 we have:

$$\frac{\partial B_s(s)}{\partial y} = \frac{\partial B_y(s)}{\partial s} = B\rho \left(\frac{1}{\rho(s)}\right)' \tag{2.75}$$

Thus one can write:

$$B_s(s) = B\rho y \left(\frac{1}{\rho(s)}\right)' \tag{2.76}$$

And we get an expression of the parallel field in terms of particle coordinates:

$$\vec{B}_{\parallel}(s) \approx B\rho \left(\frac{y}{\rho(s)}\right)' \vec{s} \tag{2.77}$$

We now change the independent variable to the angle θ introduced Section 2.1.1. Using the equations 2.2 and 2.23 we can express the spin precession in the cylindrical coordinate system:

$$\frac{\mathrm{d}\vec{S}}{\mathrm{d}t} = \frac{\mathrm{d}\vec{S}}{\mathrm{d}\theta}\theta' \dot{s} \approx \frac{1}{\rho(s)} \frac{v}{\left(1+\frac{x}{\rho(s)}\right)} \frac{\mathrm{d}\vec{S}}{\mathrm{d}\theta} \tag{2.78}$$

Then using equation 2.65, the expressions developed in equations 2.73 and 2.77, and keeping only the linear terms in x and y we get:

$$\frac{\mathrm{d}\vec{S}}{\mathrm{d}\theta} \approx \vec{S} \times \left[\left(1+G\gamma\right) \begin{pmatrix} -y'' \\ \frac{y'}{\rho(s)} \\ x'' - \frac{1}{\rho(s)} \end{pmatrix} - \left(1+G\right) \begin{pmatrix} 0 \\ \left(\frac{y}{\rho(s)}\right)' \\ 0 \end{pmatrix} \right] \rho(s) \tag{2.79}$$

It is worth pointing out that we keep the radius of curvature as being function of s, even if we now consider θ as the relevant independent variable, in order to keep the notation used until now. Although the spin vector is a function of the position θ or s we will just write it $\vec{S}$ to lighten the notation. New variables will not always explicitly show their dependence on the azimuth. We

pose:

$$\frac{\mathrm{d}\vec{S}}{\mathrm{d}\theta} = \vec{S} \times \vec{F} \quad \text{and} \quad \vec{F} = F_1\vec{x} + F_2\vec{s} + F_3\vec{y} \tag{2.80}$$

with:

$$\begin{aligned} F_1 &= -\rho(s)(1+G\gamma)y'' && (2.81)\\ F_2 &= y'(1+G\gamma) - \rho(s)(1+G)\left(\frac{y}{\rho(s)}\right)' && (2.82)\\ F_3 &= (1+G\gamma)(\rho(s)x'' - 1) \approx -(1+G\gamma) && (2.83) \end{aligned}$$

where the term in x'' in F_3 is dropped since it is small and averages to 0.

In the frame which rotates with the particle at its cyclotron frequency (see Eq. 2.67), equation 2.80 can be written [35]:

$$\frac{\mathrm{d}\vec{S}}{\mathrm{d}\theta} = \vec{n} \times \vec{S} \qquad \text{with} \qquad \vec{n} = -\left[F_1\vec{x} + F_2\vec{s} + (1+F_3)\vec{y}\right] \tag{2.84}$$

and

$$\begin{aligned} \vec{n} &= -\left[F_1\vec{x} + F_2\vec{s} + (1+F_3)\vec{z}\right] && (2.85)\\ &= -F_1\vec{x} - F_2\vec{s} + G\gamma\vec{z} \end{aligned}$$

where $\vec{n}$ is the local precession axis of the spin. If we consider a particle on the OCO its transverse coordinates are zero and $F_1 = F_2 = 0$. Equation 2.84 takes the form of a precession around the vertical axis:

$$\frac{\mathrm{d}\vec{S}}{\mathrm{d}\theta} = G\gamma\,\vec{y} \times \vec{S} \tag{2.86}$$

2.3.3 Spinor Formalism

The use of spinors and quantum mechanics formalism allows convenient representation of the solution to the Thomas-BMT equation. In the spinor formalism, the spin vector $\vec{S}$ can be expressed as [36]:

$$\vec{S} = \psi^{\dagger} \vec{\sigma} \psi \tag{2.87}$$

where ψ is a two component complex vector called spinor and $\psi^{\dagger}$ designates the hermitian conjugate of ψ. We also use $\vec{\sigma}$, the Pauli vector, defined as:

$$\vec{\sigma} = \sigma_x \vec{x} + \sigma_s \vec{s} + \sigma_y \vec{y}$$
$$\text{and} \qquad \sigma_x = \begin{pmatrix} 0 & 1 \\ 1 & 0 \end{pmatrix}, \quad \sigma_s = \begin{pmatrix} 0 & -i \\ i & 0 \end{pmatrix}, \quad \sigma_y = \begin{pmatrix} 1 & 0 \\ 0 & -1 \end{pmatrix} \tag{2.88}$$

Expressing the equation of spin motion in the spinor formalism we get [4]:

$$\frac{\mathrm{d}\psi}{\mathrm{d}\theta} = -\frac{i}{2}\left(\vec{\sigma} \cdot \vec{n}\right)\psi = -\frac{i}{2} \begin{pmatrix} G\gamma & -\xi \\ -\xi^* & -G\gamma \end{pmatrix} \psi \tag{2.89}$$

The term $\vec{\sigma} \cdot \vec{n}$ is called the precessing kernel and describes the evolution of the spin vector. The diagonal terms dominate and give the precession rate of the spin vector around the vertical axis, which is the spin tune Q_S. The off diagonal terms perturb the motion around the vertical axis.

2.3.3.1 Spin Transfer Matrix

As for beam dynamics, it is convenient to use a matrix formalism to transport the spin through successive magnetic elements in the accelerator. Since the precessing kernel in equation 2.89 is

independent of θ, the propagation of the spinor ψ from θ_1 to θ_2 is:

$$\psi(\theta_2) = e^{-\frac{i}{2}(\vec{\sigma}\cdot\vec{n})(\theta_2-\theta_1)}\psi(\theta_1) \tag{2.90}$$

In the case of a particle traveling on the *OCO*, longitudinal or radial fields are zero and $\xi = 0$. Then the transport of the spinor from θ_1 to θ_2 results in a rotation of the spin vector of $2\pi G\gamma(\theta_2 - \theta_1)$ around the vertical direction:

$$\psi(\theta_2) = e^{-\frac{i}{2}G\gamma\sigma_y(\theta_2-\theta_1)}\psi(\theta_1) \tag{2.91}$$

The carrying term $e^{-\frac{i}{2}(\vec{\sigma}\cdot\vec{n})(\theta_2-\theta_1)}$ is called the spin transfer matrix usually denoted $t(\theta_2, \theta_1)$. The spin transfer matrix can conveniently be expressed using the Pauli matrices:

$$t = t_0 I - i(t_x\sigma_x + t_s\sigma_s + t_y\sigma_y) = \begin{pmatrix} t_{11} & t_{12} \\ t_{21} & t_{22} \end{pmatrix} \tag{2.92}$$

where the classical nature of the spin vector constraints the matrix elements of the spin transfer matrix to satisfy:

$$t_{22} = t_{11}^* \quad \text{and} \quad t_{21} = -t_{12}^* \tag{2.93}$$

Similarly to beam dynamics, we can build the spin transfer matrix of multiple elements by multiplying the spin transfer matrix of each element:

$$\psi(\theta) = \prod_{j=1}^{n} t(\theta_{j+1}, \theta_j)\psi(\theta_1) = t(\theta, \theta_1)\psi(\theta_1) \tag{2.94}$$

The spin transfer matrix for one turn of the AGS is called the one turn spin map [4]:

$$t(\theta + 2\pi, \theta) = e^{-i\pi Q_S \vec{n}_{co}\cdot\vec{\sigma}} \tag{2.95}$$

where $\vec{n}_{co}$ along the ring is the spin closed orbit. The transformation of the spin vector is a rotation of $2\pi Q_S$ around $\vec{n}_{co}$.

2.3.3.2 Spin Transfer Matrix and Formal Computation

The spin tune and the spin closed orbit are fundamental quantities of the spin dynamics in the AGS. We want to be able to visualize the effect of different parameters on Q_S and $\vec{n}_{co}$. However, the computation of the one turn spin map and its identification to equation 2.95 gets very complex when the number of elements considered increases. For this reason, programs were developed with the formal computation software Mathematica [37].

First we transform the exponential notation of the rotations of in equation 2.90 using Euler's equation:

$$e^{-\frac{i}{2}(\vec{\sigma}\cdot\vec{n})(\theta_2-\theta_1)} = \mathbb{1}\cos\left(-\frac{1}{2}(\theta_2-\theta_1)\right) + i(\vec{\sigma}\cdot\vec{n})\sin\left(-\frac{1}{2}(\theta_2-\theta_1)\right) \tag{2.96}$$

where $\mathbb{1}$ is the identity matrix. Then spin transfer matrices are multiplied to obtain the one turn spin map $t(\theta+2\pi,\theta)$. Finally, we solve for (a,b,c,d):

$$t(\theta+2\pi,\theta) = \mathbb{1}a - i(b\sigma_x + c\sigma_s + d\sigma_y) \tag{2.97}$$

The spin tune and spin closed orbit are given by:

$$Q_s = \frac{1}{\pi}\cos^{-1}(a) \quad \text{and} \quad \vec{n}_{co} = \begin{pmatrix} \frac{b}{\sin(-\pi Q_s)} \\ \\ \frac{c}{\sin(-\pi Q_s)} \\ \\ \frac{d}{\sin(-\pi Q_s)} \end{pmatrix} \tag{2.98}$$

This gives a quick method to evaluate the effect of complicated configurations as we will see

in Section 2.4. The flexibility of Mathematica also allows to interactively change some of the parameters and understand their effects on the evolution of the spin vector and spin tune.

2.3.4 Depolarizing Spin Resonances

The off diagonal terms in equation 2.89 cause the spin to precess around the $\hat{x}$ and $\hat{s}$ directions. These terms are perturbing the precession around the vertical and can be expressed [4]:

$$\begin{aligned} \xi(\theta) &= F_1 - iF_2 \\ &= -(1+G\gamma)(\rho(s)y'' + iy') - i\rho(s)(1+G)\left(\frac{y}{\rho(s)}\right)' \end{aligned} \tag{2.99}$$

The perturbing term ξ has a very small effect on the spin compared to the precession around the vertical axis and the spin generally stays close to $\vec{y}$. However, when these perturbing fields add up coherently in the machine they can have strong effects on the polarization. Therefore, when conditions are satisfied, spin resonance can occur and amplify the effect of the perturbing fields, possibly leading to partial or total depolarization of the beam.

Equation 2.99 shows that the perturbing term depends on the motion of the particle in the vertical plane, which is a combination of vertical closed orbit and vertical betatron motion. Since this motion is quasi-periodic with θ, we can expand ξ in a Fourier series:

$$\xi(\theta) = \sum_K \varepsilon_K e^{iK\theta} \tag{2.100}$$

The resonant frequency is given by K and is called the resonant spin tune. The Fourier coefficient ε_K is called the depolarization resonance strength and is detailed in Section 2.3.4.2. While we define the depolarizing resonances, arises the question of the behavior of the polarization when such a resonance is crossed. It is also important to understand the relevant parameters to reduce or avoid losses of polarization across these resonances.

2.3.4.1 Depolarization Across a Single Resonance : Froissart-Stora Formula

We consider the case of an accelerated beam across a single isolated resonance. While we defined (Eq. 2.69) that the spin tune is function of the energy, we conveniently consider a constant acceleration rate, hence a constant time derivative of the spin tune:

$$\alpha = \frac{\mathrm{d}G\gamma}{\mathrm{d}t} \tag{2.101}$$

While α designates the acceleration rate in unit $G\gamma$, it is usually called the crossing rate. When the spin resonance at $G\gamma = K$ with a strength ε_K is crossed, the asymptotic final polarization P_f is given by:

$$\frac{P_f}{P_i} = 2e^{-\pi\frac{|\varepsilon_K|^2}{2\alpha}} - 1 \tag{2.102}$$

where P_i is the initial polarization. Equation 2.102 was derived by Froissart and Stora [38] and presents the asymptotic polarization for the crossing of a single resonance at constant speed. Equation 2.102 shows that the final polarization only depends on the ratio $\frac{|\varepsilon_K|^2}{\alpha}$. Hence, constraints can be established on this ratio to have most of the polarization conserved, i.e. $P_f/P_i \approx \pm 1$.

- In the case where the resonance strength is low enough or the crossing speed large, the polarization can be conserved. For instance, if we aim to conserve at least 99% of the polarization, resonance strength and crossing rate need to satisfy:

$$\frac{|\,\varepsilon_K\,|^2}{\alpha} \leq 3.2\,10^{-3} \tag{2.103}$$

- If the resonance is strong enough or the crossing rate small, the polarization can be preserved by achieving a spin-flip. In this case the resonance is strong enough to fully flip the spin, without loss of polarization. Again, if we want to conserve 99% of the polarization we need

to satisfy:

$$\frac{\mid \varepsilon_K \mid^2}{\alpha} \geq 3.4 \tag{2.104}$$

We have seen that polarization losses can be avoided by carefully adjusting the ratio $\frac{|\varepsilon_K|^2}{\alpha}$. We will now investigate the parameters influencing the strength ε_K of depolarizing resonances.

2.3.4.2 Spin Resonance Strength

The depolarization resonance strength is a complex quantity independent of θ [4]:

$$\begin{aligned} \varepsilon_K &= \frac{1}{2\pi}\oint \xi e^{iK\theta}\mathrm{d}\theta \\ &= \frac{1}{2\pi}\oint \left[(1+G\gamma)(\rho(s)y''+iy') - i\rho(s)(1+G)\left(\frac{y}{\rho(s)}\right)'\right] e^{iK\theta}\mathrm{d}\theta \end{aligned} \tag{2.105}$$

The resonant condition is satisfied when the resonant tune K equals the spin tune Q_S. While equation 2.105 gives the general form of the strength of spin resonances, one can find a simpler form by means of some approximations. In the AGS $\rho(s)$ is very large, therefore the integrand of equation 2.105 is dominated by the term $\rho(s)y''$. Neglecting the other terms and replacing the independent variable by the longitudinal coordinate s we get:

$$\varepsilon_K \approx -\frac{1+G\gamma}{2\pi}\oint y'' e^{iK\theta}\mathrm{d}s \tag{2.106}$$

We can also express ε_K as a function of the perturbing field. Using equation 2.26 we can write:

$$\varepsilon_K \approx \frac{1+G\gamma}{2\pi}\oint k_1(s) y e^{iK\theta}\mathrm{d}s \tag{2.107}$$

The resonance strength ε_K depends on the vertical motion around the machine and we can separate the depolarizing resonances between two types called imperfection and intrinsic spin resonances.

2.3.4.3 Intrinsic Spin Resonance

When the relation $Q_S = K \pm \nu_y$ is satisfied, perturbing fields add up coherently due to the betatron motion of the particle. The betatron motion cannot be avoided when beam with non zero emittance is considered. This type of resonance exists even in a perfect machine. While these resonances are intrinsically related to the machine they are called intrinsic depolarization spin resonances.

To compute the strength of an intrinsic spin resonance we can replace y in equation 2.107 by the parametric expression of the vertical motion (Eq. 2.43). We express the resonance strength as a function of s [4]:

$$\varepsilon_K \approx \frac{1+G\gamma}{2\pi}\sqrt{\varepsilon_y}\oint k_1(s)\sqrt{\beta_y(s)}\cos\big(\mu_y(s)+\mu_y(0)\big)e^{iK\theta}\mathrm{d}s \tag{2.108}$$

Due to the periodicity of the beta function, the integrand is non zero only if:

$$K = mP \pm Q_y \tag{2.109}$$

where m is an integer and P is the number of superperiods in the lattice. In a real accelerator, errors break the superperiodicity and weak intrinsic spin resonances occur when:

$$K = n \pm Q_y \quad (n \neq mP) \tag{2.110}$$

where n is an integer. Table 2.3 classifies the intrinsic resonances as a function of their strengths and shows that the strongest resonances also involve M, the number of FODO cells per superperiod [4].

One can note that in equation 2.108 the strength of the resonance depends on the Courant-Snyder invariant of the particle. Therefore, different particles within the same beam will see different spin resonance strength depending on their vertical invariant. This jeopardizes the possibility

Table 2.3 Types of intrinsic spin resonances [4]

K	Location in the AGS	Resonance denomination
nPM $\pm Q_y$	$0+Q_y$, $36\pm Q_y$	strong intrinsic resonance
nP $\pm Q_y$	$12\pm Q_y$, $24\pm Q_y$, $24\pm Q_y$,$48\pm Q_y$	intrinsic resonance
n $\pm Q_y$	all others	weak intrinsic resonance

of spin flip addressed in Section 2.3.4.2 because some particles with lower vertical invariant will not see a strong enough resonance to cause a full spin flip.

2.3.4.4 Imperfection Spin Resonances

When K is an integer and $Q_S = K$, the perturbing fields due to the vertical closed orbit add up coherently turn after turn and can cause the precession around $\hat{x}$ and $\hat{s}$ to become significant compared to $G\gamma$, depolarizing the beam. Since the vertical closed orbit in a synchrotron is due to field or alignment errors, this type of resonance is called imperfection spin resonance.

We can consider a closed orbit due to random errors along the ring. The resulting closed orbit distortion is given by [4]:

$$y_{co}(s) = \sqrt{\beta_y(s)} \sum_l \frac{Q_y^2 f_l e^{il\mu_y(s)}}{Q_y^2 - l^2} \tag{2.111}$$

where f_l is the Fourier coefficient of the error harmonic l and can be computed using: [4]

$$f_l = \frac{1}{2\pi Q_y} \oint \sqrt{\beta_y(s)} k_1(s) e^{-il\mu_y(s)} \mathrm{d}s \tag{2.112}$$

Replacing y by y_{co} in equation 2.107 we obtain [4]:

$$\varepsilon_K = \frac{1+G\gamma}{2\pi} \sum_l \frac{Q_y^2 f_l e^{il\mu_y(s)}}{Q_y^2 - l^2} \oint k_1(s) \sqrt{\beta_y(s)} e^{il\mu_y(s)} e^{iK\theta} \mathrm{d}s \tag{2.113}$$

As for the intrinsic resonance, the strength of the imperfection resonance is enhanced by the pe-

Table 2.4 Types of imperfection spin resonances [4]

K	Resonance denomination
nPM	strong imperfection resonance
nP	imperfection resonance
n	weak imperfection resonance

riodicity of the machine. Table 2.4 summarizes the different types of imperfection resonances. Unlike the intrinsic resonance, the strength of the imperfection spin resonance does not depend on the vertical invariant of each particle. Furthermore, harmonic correction or distortion of the vertical orbit, respectively, usually allow full conservation or spin-flip of all the particles within a bunch.

Figure 2.8 shows the resonance strength obtained by the Zgoubi code. The strengths were estimated using the depolarization of a single particle tracked through a single resonance and applying equation 2.102. The results were very close to the predicted theoretical strengths [1].

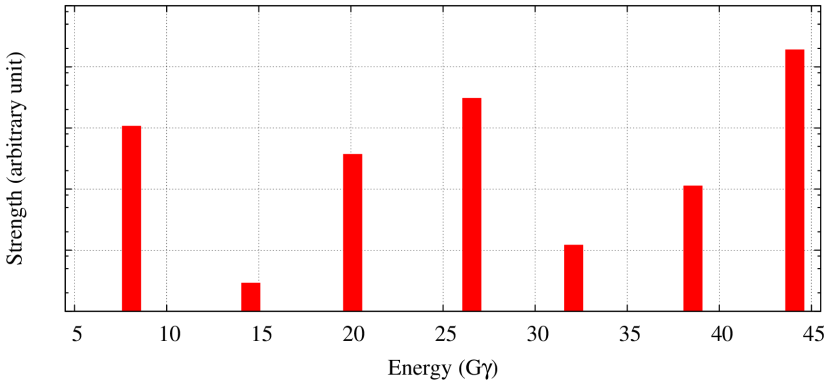

(a)

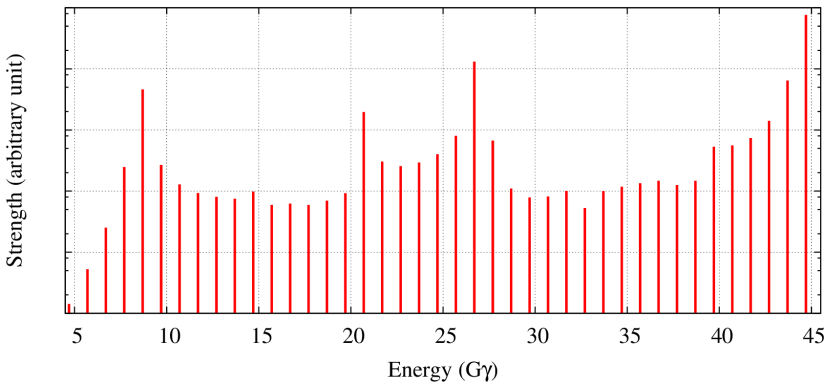

(b)

Figure 2.8 Intrinsic (a) and imperfection (b) resonances strengths in the AGS as a function of the energy, in arbitrary units on a logarithmic scale [1].

2.4 Spin Dynamics with Partial Snakes

In the early 70's, Derbenev and Kondratenko proposed to overcome spin resonances in circular accelerators by using a local spin rotator capable of rotating the spin vector by 180° about a horizontal axis.

2.4.1 Spin Dynamics with One Full Snake

To see the effect of such a spin rotator on the spin dynamics, we can conveniently use the spin transfer matrix formalism introduced earlier. We can consider the spin rotator as a localized rotation of the spin vector of 180° around $\vec{s}$. With the observer at an orbital angle θ from the spin rotator, the resulting one turn spin map is:

$$t(\theta+2\pi,\theta) = e^{-\frac{i}{2}G\gamma(2\pi-\theta)\sigma_y} e^{-\frac{i}{2}\pi\sigma_s} e^{-\frac{i}{2}G\gamma\theta\sigma_y} \tag{2.114}$$

Using the tools presented in Section 2.3.3.2 one finds:

$$Q_S = \frac{1}{2} \quad \text{and} \quad \vec{n}_{co} = \begin{pmatrix} -\sin\left(G\gamma(\pi-\theta)\right) \\ -\cos\left(G\gamma(\pi-\theta)\right) \\ 0 \end{pmatrix} \tag{2.115}$$

The spin tune is not function of the energy. All imperfection resonances are avoided since the spin tune never takes integer values. With the fractional part of the vertical betatron tune different than $Q_y = 0.5$, all intrinsic resonances are also avoided. In this case, the spin closed orbit vector is on the horizontal plane and precesses around the vertical dipole field around the ring.

This principle is used for RHIC, although 2 spin rotators are used to obtain a spin closed orbit vector aligned on the vertical axis.

2.4.1.1 Siberian Snakes

Spin rotators inducing a precession of the spin around the directions $\vec{x}$ or $\vec{s}$ are called Siberian snakes [4]. The first type of snake is a solenoid featuring a constant longitudinal field. From equation 2.65 we can see that such a field would slowly and continuously rotate the spin vector around the longitudinal axis. However, a longitudinal field is not very effective, particularly at high rigidity. The term $(1+G)$ in equation 2.65 shows that the required integrated field grows linearly with the momentum, for a constant rotation of the spin vector. This system was used in the AGS in the 90's [39] but is generally only used at low energy.

The second type of spin rotator uses transverse dipole fields to rotate the spin. The main advantage comes from the factor $(1+G\gamma)$ in equation 2.65 that enhances the effect of a transverse field $B_{\perp}$. The required integrated field to maintain the precession angle as the energy increases is then only proportional to $1/\beta$ [4]. This is necessary for high energy machines such as RHIC. Different solutions are possible, involving successions of horizontal and vertical dipole magnets but an original and compact solution features a helical dipole field. This last solution is used at RHIC and allows to minimize the excursion of the orbit inside the snake.

While Siberian snakes and especially helical magnets are a good solution to conserve the polarization in high energy synchrotrons, it is not always possible to use them. For instance, each snake in the RHIC is around 10m long to create the 180° rotation of the spin vector. In the AGS, the longer straight sections are no more than 3 m long. Therefore the use of a helical snake capable of rotating the spin vector by 180° is not possible. For this reason it was proposed to use partial snakes in the AGS, capable of rotating the spin vector by only a fraction of 180° [40].

2.4.2 Spin Dynamics with Two Partial Snakes

The AGS uses two partial helical snakes pictured in Figure 3.4. The idea was proposed to use two short partial snakes separated by one third of the ring [40], with the strong partial snakes being

(a) (b)

Figure 2.9 Pictures of the superconducting helical snake in the A20 straight section (a) and the normal conducting helical snake in the straight section E20 (b).

short enough to fit in a long straight section of the AGS while offering a precession of the spin around the longitudinal axis of 10 to 20 degrees.

While we have seen that a single full spin rotator allows to overcome imperfection and intrinsic spin resonances we will see the effect of the AGS configuration on the spin dynamics.

2.4.2.1 Spin Dynamics with Two Partial Snakes Separated by One Third of the Ring

Lets consider an observer located between the two snakes, at an angle θ from the warm snake (between A20 and E20 straight sections). With χ_w and χ_c, the angles of the spin rotation respectively caused by the warm snake and cold snake, we can write:

$$\begin{aligned} t(\theta+2\pi,\theta) &= t(\theta+2\pi,\text{cold snake})\cdot e^{-i\frac{1}{2}\chi_c\sigma_2}\cdot t(\text{cold snake},\text{warm snake})\cdot e^{-i\frac{1}{2}\chi_w\sigma_2}\cdot t(\text{warm snake},\theta) \\ &= e^{-i\frac{1}{2}G\gamma(2\pi/3-\theta)\sigma_3}e^{-i\frac{1}{2}\chi_c\sigma_2}e^{-i\frac{1}{2}G\gamma(4\pi/3)\sigma_3}e^{-i\frac{1}{2}\chi_w\sigma_2}e^{-i\frac{1}{2}G\gamma\theta\sigma_3} \end{aligned} \tag{2.116}$$

Again, using the method introduced in section 2.3.3.2 we determine the spin tune and the spin closed orbit between the snakes:

$$Q_S = \frac{1}{\pi}\arccos\left\{\cos\left(\frac{\chi_c}{2}\right)\cos\left(\frac{\chi_w}{2}\right)\cos(G\gamma\pi) - \sin\left(\frac{\chi_c}{2}\right)\sin\left(\frac{\chi_w}{2}\right)\cos\left(G\gamma\frac{\pi}{3}\right)\right\} \tag{2.117}$$

$$\vec{n}_{co}\cdot\vec{x} = \frac{-1}{\sin(\pi\nu_S)}\left\{\cos\left(\frac{\chi_c}{2}\right)\sin\left(\frac{\chi_w}{2}\right)\sin\left(G\gamma(\pi-\theta)\right) - \sin\left(\frac{\chi_c}{2}\right)\cos\left(\frac{\chi_w}{2}\right)\sin\left(G\gamma\left(\frac{\pi}{3}+\theta\right)\right)\right\} \tag{2.118}$$

$$\vec{n}_{co}\cdot\vec{y} = \frac{1}{\sin(\pi\nu_S)}\left\{\cos\left(\frac{\chi_c}{2}\right)\sin\left(\frac{\chi_w}{2}\right)\cos\left(G\gamma(\pi-\theta)\right). + \sin\left(\frac{\chi_c}{2}\right)\cos\left(\frac{\chi_w}{2}\right)\cos\left(G\gamma\left(\frac{\pi}{3}+\theta\right)\right)\right\} \tag{2.119}$$

$$\vec{n}_{co}\cdot\vec{y} = \frac{1}{\sin(\pi\nu_S)}\left\{\cos\left(\frac{\chi_c}{2}\right)\cos\left(\frac{\chi_w}{2}\right)\sin(G\gamma\pi) + \sin\left(\frac{\chi_c}{2}\right)\sin\left(\frac{\chi_w}{2}\right)\sin\left(G\gamma\frac{\pi}{3}\right)\right\} \tag{2.120}$$

In the case of an observer located in the superperiods F to A, slightly different expressions for the spin closed orbit are found [41]. We can see that the spin tune (Eq. 2.117) now depends on the energy $(G\gamma)$. From equations 2.118 to 2.120 we can see that the stable spin direction can be away from the vertical axis and precesses around the vertical bending field. We can now use the strength of the two snakes to determine the evolution of the spin tune as a function of the energy.

Figure 2.10 shows the spin tune around $G\gamma = 9$ for different strengths of the two snakes. We can see that without snakes we have the regular relation $Q_S = G\gamma$, but with non zero snake strengths a forbidden band for the spin tune opens around the integer. The forbidden band is called the spin tune gap and increases with the snake strength.

Similarly to the case with a single full snake seen in Section 2.4.1, the imperfection resonances are avoided since the spin tune cannot take integer values. The vertical intrinsic resonances can be avoided if the resonant condition $Q_S = I \pm Q_y$ is avoided, i.e. if the fractional part of the vertical

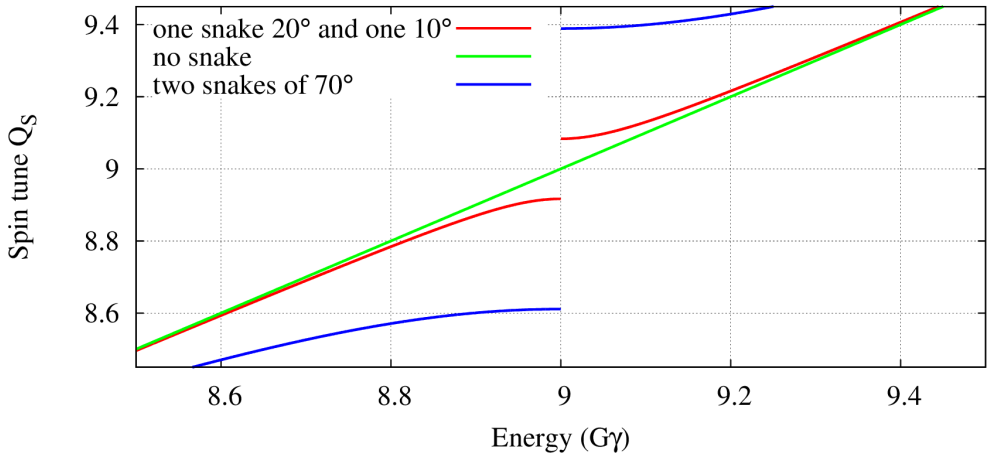

Figure 2.10 Spin tune as a function of the energy from equation 2.117 and for different snake strengths.

tune is in the spin tune gap. With our example in Figure 2.10, it would constrain the fractional part of the vertical tune to be higher than 0.916 or lower than .084 for the case with two snakes of 10° and 20°.

2.4.2.2 Partial Snakes Strengths in the AGS

As mentioned in Section 2.4.1.1, the spin rotation induced by helical magnets is proportional to $1/\beta$ [4]. Figure 2.11 shows the evolution of the strengths of the two snakes in the AGS, computed using OPERA field maps of the magnets and the Zgoubi code. The knowledge of the evolution of the snakes strengths as a function of the energy is important to accurately compute the spin tune and the stable spin direction during the AGS acceleration cycle. For easier handling, polynomial functions were fitted to the snake strengths in Figure 2.11. We can express the evolution of the snake strength in degrees as a function of the energy in γ using a polynomial function:

$$\chi(\gamma) = \left(\frac{B}{B_0}\right)^2 \left(C_1 + \frac{C_{12}}{\gamma} + \frac{C_2}{\gamma^2}\right) \tag{2.121}$$

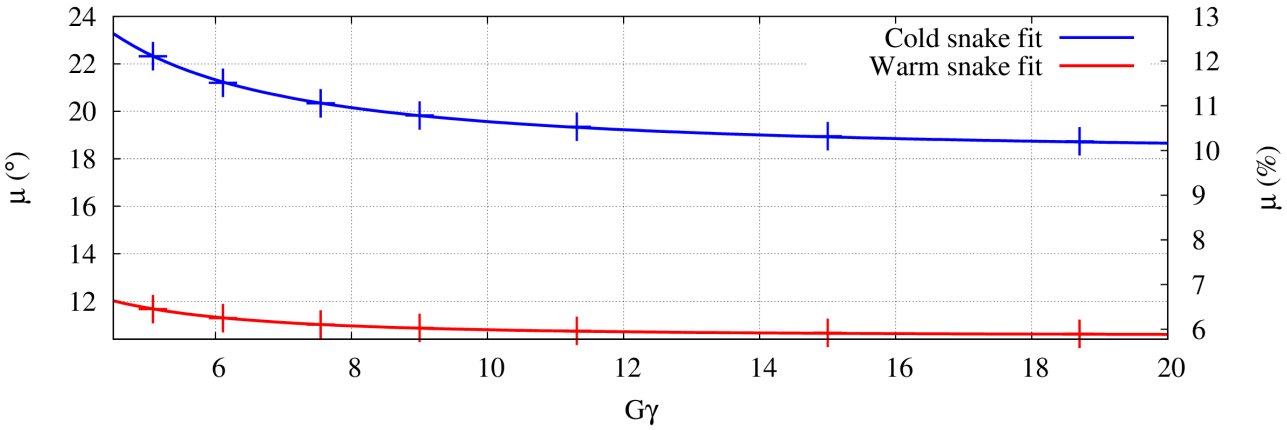

Figure 2.11 Snakes strengths expressed in degrees (left axis) and in fraction of full snake (right axis) as a function of the energy in the lower range of the AGS acceleration cycle.

For the cold snake the parameters are:

$$B = 2.14 \quad , \quad B_0 = 2.5 \quad , \quad C_1 = 24.7 \quad , \quad C_{12} = 5.82 \quad , \quad C_2 = 29.9 \tag{2.122}$$

and for the warm snake:

$$B = 1.53 \quad , \quad B_0 = 1.53 \quad , \quad C_1 = 10.584 \quad , \quad C_{12} = -0.79 \quad , \quad C_2 = 11 \tag{2.123}$$

We can now use equation 2.117 to plot the evolution of the spin tune as a function of the energy. Figure 2.12 shows the evolution of the spin tune in the AGS with the two partial snakes at their nominal strengths and allows important remarks, a periodicity of 3 in the maximum value reached by the spin tune is apparent. The separation of the two snakes by one third of the ring causes their strengths to add up coherently when $G\gamma = 3n$ with n an integer. It also appears that the 12 superperiods of the AGS makes the strongest intrinsics spin resonances occur when the strengths of the two snakes add up. Figure 2.12 (a) shows the spin tune gap reducing as the energy increases. This is due to the larger strength of the snakes being at low energy as shown Figure 2.11. If the vertical tune can be brought close enough to the integer, the resonant condition $Q_S \pm Q_y = I$ is

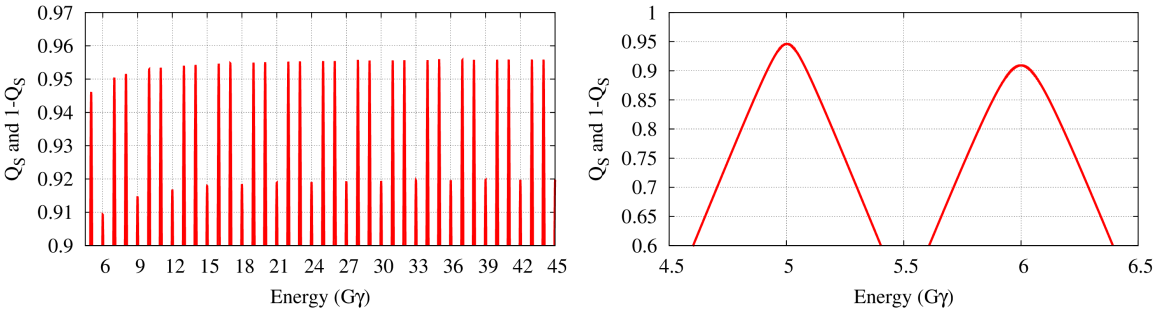

(a) (b)

Figure 2.12 Fractional part of the spin tune in the AGS (a) and a zoom in the low energy range of the AGS (b).

avoided. In the AGS, the vertical tune is pushed above $Q_y = 8.96$ as much as possible and the vertical intrinsic resonances are avoided.

We have seen that the partial snakes configuration is a good solution for the AGS since it allows overcoming both imperfection and intrinsic spin resonances. However, we will see that it also creates new issues both for beam and spin dynamics.

2.5 Downsides of the Partial Snakes Configuration

In this section we will list the side effects of the partial snake configuration in the AGS.

2.5.1 Horizontal Intrinsic Resonances

We have seen that with the partial snakes, the stable spin orbit direction on the closed orbit (Eq. 2.120) is not vertical. Figure 2.13 shows non zero horizontal competent of the stable spin direction $\vec{n}_0$. Therefore vertical fields can also perturb the precession of the spin. Through the same mechanism as for the usual intrinsic spin resonances seen in Section 2.3.4.3, depolarization can be driven

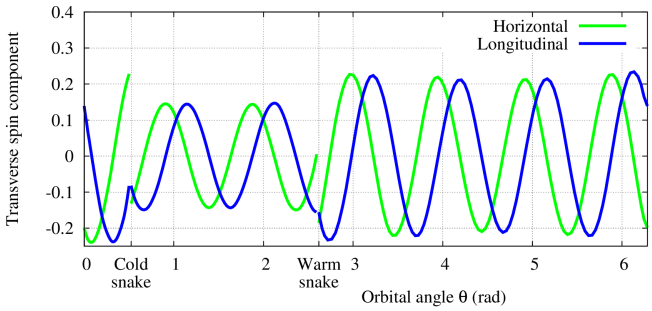

(a)

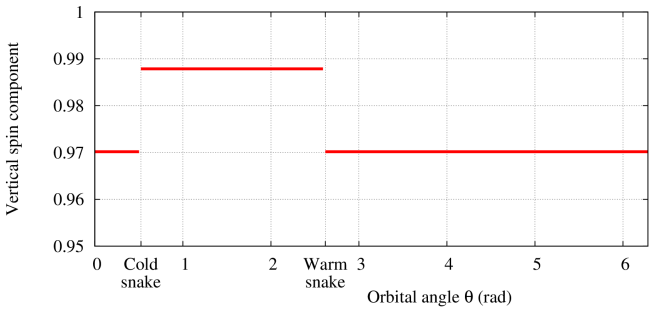

(b)

Figure 2.13 Evolution of the spin closed orbit around the AGS at an energy of $G\gamma = 6.5$, on the horizontal plane (a) and on the vertical plane (b).

by the horizontal betatron motion of the particle when:

$$\nu_S \pm Q_x = integer \tag{2.124}$$

Since these spin resonances are due to the horizontal betatron motion they are called horizontal intrinsic spin resonances. Figure 5.11 shows the crossing of the first two horizontal intrinsic spin resonances encountered during the AGS acceleration cycle.

2.5.2 Optical Effect

The strong and highly non linear magnetic field generated by the two Siberian snakes can also be detrimental to the beam dynamics. The effect is particularly strong at low energy and limits the flexibility of the machine in the early part of the acceleration cycle [15, 42]. This is a major aspect of this work and addressed in the next chapters.

Chapter 3

A Model of the AGS with the Ray-Tracing Code Zgoubi

3.1 History of the AGS Models: from BEAM to Zgoubi

As shown in Section 2.1, beam dynamics in synchrotrons such as the AGS is complex, even within the approximations used in this work (see Section 2.1.1.1). Hence the necessity for equally complex simulations of the beam dynamics, starting as early as the design stage in the 50's [43]. However, computation power was limited at that time and one could think that modeling was limited to the use of first order matrix formalism (Section 2.1.1.2). Nonetheless, one of the first computer codes used for the AGS was a tracking code, the BEAM code, operational in 1960 and developed by E.D. Courant using the Fortran language. In particular, the code was used to compute the orbit of an injected proton beam at 50 MeV under the influence of the main magnet fringe field, using one of the first standardized computers: the IBM 704 [44]. Other references mention the computation of particle trajectories with high accuracy using one of the first supercomputer, the CDC-6600 [45].

Although available material from these simulations is limited, it seems that the BEAM code was mainly used to compute stable injection orbits in the AGS, likely due to the limited computation power. The oldest *systematic* use of a computer model for AGS operations was based on the MAD code [46], in the 1980's [47, 48].

3.1.1 MADX Model of the AGS

The development of the MAD model of the AGS started in the late 1980's [49]. It uses matrices of the AGS elements to determine the Courant-Snyder parameters along the machine lattice. In its first implementation only main magnets and straight sections were included, without misalignments. The main magnets were simulated using constant quadrupole and sextupole normalized field strengths, available for only 6 different proton momenta (15, 20, 25, 27, 29 and 32 GeV/c), although the source of these data is not clear in the original publications [49].

Shortly afterward, the MAD model was used for the development and commissioning of the AGS gamma transition quadrupoles [47, 48], with good agreement on the measurements. Limited documentation on the evolution of the model precludes the establishment of a complete timeline.

Today the AGS model is well documented. It uses the MADX code and can be accessed through the *MadxFromSnaprampCmd* command [50]. The command accepts several parameters activated by specific arguments, the most relevant to understand the *MadxFromSnaprampCmd* being:

- `-snapramp` to provide the *snapramp* directory. It contains AGS operational settings and readbacks for all power supplies used, along a single cycle. The save of a *snapramp* is triggered by several ways, including through a command line.

- `-timeSteps` to provide the timings at which the model of the AGS will be computed. A set of timing is subsequently generated at which the model is produced.

- `-noblw` and `-nogammajump` to respectively remove the backleg windings[1] or the gamma transition quadrupoles from the model.

- `-bare` to only use the main magnets, ignoring all other elements.

Then MADX input files are generated using the *snapramp* data and optical functions are computed at the requested timings. A graphical user interface, the *AGSModelViewer*(see Figure 3.1), is also available to conveniently use the *MadxFromSnaprampCmd* command and display the results [51].

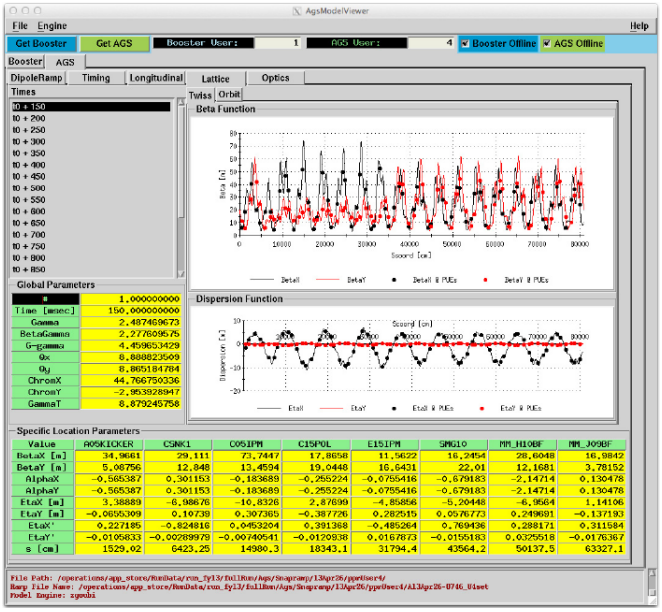

Figure 3.1 The AGS "lattice" page of the AgsModelViewer, at an early timing [2].

For each requested timing, the *MadxFromSnaprampCmd* command generates a MADX input file through the following steps:

- The main magnet current is used to determine the momentum of protons circulating on the *OCO*. In practice a polynomial function generated from the measured integrated dipole strength of the main magnets is used [23] (see Section 3.3.1.2).

[1] Conductor winding on the return yoke of some AGS main magnets to modify the net excitation of groups of magnets, to control the closed orbit. This changes the effective number of Ampere-turns and has an effect on all field components of the magnets.

- The quadrupole and sextupole normalized field strengths of the main magnets are computed using polynomial functions that were generated from tracking through measured field maps [52].
- Transfer functions for the high field quadrupoles [53] and sextupoles [54] are applied to the measured currents in the *snapramp* to compute corresponding magnet strengths. Gamma transition quadrupoles, used to cross the transition energy, are also accounted for.
- Transfer functions for the so-called thin quads, compensating for the optical effect of the AGS partial snakes, are used to compute the strength of these magnets [55].
- Backleg windings are included, if requested.
- Depending on the machine configuration the Siberian snakes may be added. The snakes are here modeled by momentum dependent first order matrices [56].

Each input MADX file (for each timing) is processed and the output data, such as the orbit and periodic functions along the ring, are saved in an associated text file. Access to the data is possible via the dedicated graphical interface *AgsModelViewer* [2] or by direct access to the output files. The data structure is as follow.

```
model_150.madx       model_160.madx [...] model_900.madx       twiss
```

Where the `.madx` files are the MADX input files and one can see that in this case the model was computed from 150ms to 900ms every 10ms. The folder `twiss` contains the output file corresponding to each timing. A file named `OpticsTable.dat` contains all global data such as the tunes for each timing.

3.1.1.1 Siberian Snakes Model

The two AGS partial snakes were extensively studied [57, 58] and it was expected that strong focusing fields would be present, generating important optical distortions of the AGS lattice at low energy. This drove a strong interest to include first order linear mapping of the snakes in the MADX model, as a first approach [56]. Matrices were computed by tracking particles through computed field maps of the snakes [57,58] for proton energies ranging from $\gamma = 2.5$ to $\gamma = 26$ every $\gamma = 0.1$. The matrices were then simplectified using the Cayley transform [59]. During the creation of the AGS MADX input file, *MadxFromSnaprampCmd* uses the equilibrium proton momentum determined from the main magnets current, in order to choose the corresponding matrices of the two snakes.

This method presents the advantage of quickly providing the optical effect of each snake, particularly useful for the AGS online model. However, it only models linear effects of the snakes. Furthermore, effects of the snakes on the AGS closed orbit are also ignored. These problems were partially overcome for offline analysis by using an equivalent element approach using the MADX code, detailed in reference [56]. However it was concluded that simulation of the AGS snakes requires a full non-linear description of the fields to achieve accurate modeling of the machine.

3.1.1.2 AGS Control Command

The AGS control command *OpticsControl* was developed to control the machine tunes and chromaticities. Tunes are controlled using the two families of high field quadrupoles introduced Section 2.1.3.1. Similarly, the control of the chromaticities uses two families of sextupole magnets detailed in Section 2.1.3.2. Using the MAD code and the currents in the high field quads wired in two tune quadrupole families, linear relations were determined between the current provided to each family and the AGS tune. AGS *OpticsControl* command uses the following relation to predict the tunes Q_x and Q_y obtained when currents I_h and I_v are respectively injected in the horizontal and vertical

tune quadrupole families [60]:

$$Q_x = (m_{11} \times I_h + m_{12} \times I_v)\frac{1}{p_0} + Q_{x0}(p_0) \quad (3.1)$$

$$Q_y = (m_{21} \times I_h + m_{22} \times I_v)\frac{1}{p_0} + Q_{y0}(p_0) \quad (3.2)$$

where $Q_{x0}(p_0)$ and $Q_{y0}(p_0)$ are, respectively, the horizontal and vertical bare tune of the AGS only function of the equilibrium momentum p_0, such as obtained with the MAD model of the AGS with only the main magnets [61]. The inverse relation is used to determine the current I_h and I_v required to obtain the tunes Q_x and Q_y. The same method was used to obtain the linear transformation between currents in the two sextupole families and the AGS chromaticities [62].

The main advantage of this linear mapping method is the short computation time required, which is critical during operations. However, the model does not include the effect of other elements such as the Siberian snakes or the compensation quadrupoles. Although always used, this tool is mainly predicting relative changes in tunes, and predicted values of tunes are not accurate, particularly at low energy with the Siberian snakes. Relative tune change prediction becomes poor when the AGS optics deviates from the bare optics, which is particularly true at low energy during polarized protons acceleration due to the optical effects of the snakes.

None of the models described above provide spin dynamics parameters, or tracking. The SPINK code, based on thick element modeling from the MADX AGS model to track position and spin of protons, was developed for that purpose [63]. SPINK does not track directly in the field maps of the Siberian snakes but instead uses transfer matrices. This drove strong interest for a complete modelisation of the AGS providing full particle and spin dynamics parameters as well as tracking capabilities, in particular directly using the computed field maps of the partial snakes. The ray-tracing code Zgoubi did offer these capabilities [64, 65] in a model of the AGS started in

2009 [66, 67].

3.2 The Zgoubi Code

The Zgoubi code computes charged particles trajectories in magnetic and electric fields [3]. It was developed in the early 1970's at the CEN-Saclay in France for ray-tracing in large magnetic spectrometers. Since then, numerous developments have driven the spread of the code amongst laboratories across the world. The Lorentz equation (Eq. 2.1) and the Thomas-BMT equation (Eq. 2.65) are respectively used to track the position and spin of the particles. The core of the code is an integrator based on Taylor expansion of the position and velocity vectors to solve both beam and spin dynamics in magnetic fields [64].

3.2.1 Step-Wise Ray-Tracing Method

The Zgoubi code transports the proton position, velocity and spin vectors over a defined step of length Δs, in a local frame as defined Figure 3.2. Given the particle position $\vec{R}(M_0)$ and velocity

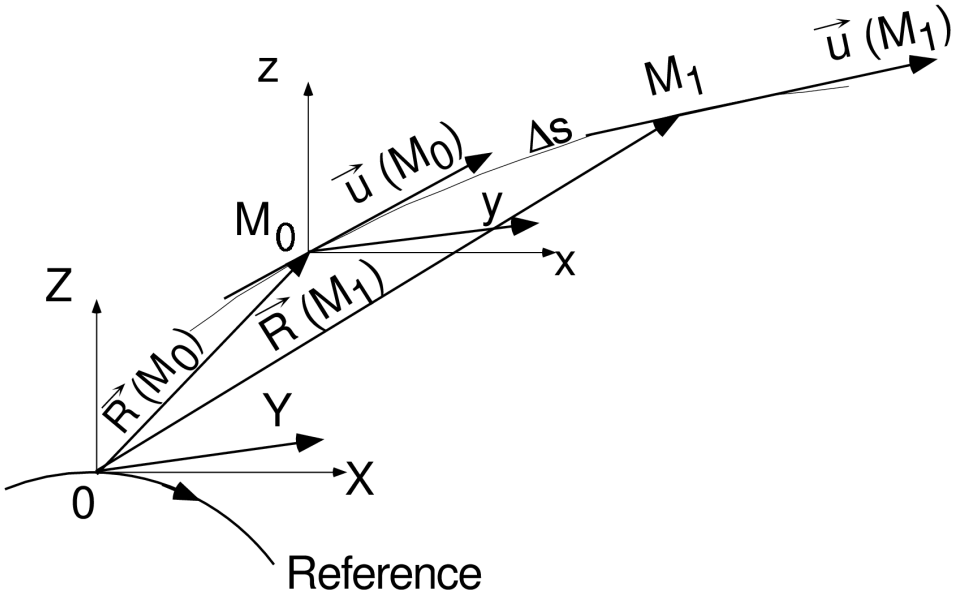

Figure 3.2 Position and velocity of a particle in the Zgoubi reference frame [3].

$\vec{u}(M_0)$, the position and velocity at M_1 are obtained using truncated Taylor series [64]:

$$\vec{R}(M_1) = \vec{R}(M_0) + \vec{u}(M_0)\Delta s + \vec{u}'(M_0)\frac{\Delta s^2}{2!} + \cdots + \vec{u}^{(5)}(M_0)\frac{\Delta s^6}{6!} \quad (3.3)$$

$$\vec{u}(M_1) = \vec{u}(M_0) + \vec{u}'(M_0)\Delta s + \vec{u}''(M_0)\frac{\Delta s^2}{2!} + \cdots + \vec{u}^{(5)}(M_0)\frac{\Delta s^5}{5!} \quad (3.4)$$

where the derivatives $\vec{u}^{(n)}$ are determined from recursive differentiation of the Lorentz equation. This involves the magnetic field and its spacial derivatives at M_0, through the Lorentz equation that can be written $\vec{u}' = \vec{u} \times \vec{B}$ [3]. The maximum order of the Taylor expansions was chosen as a compromise between tracking accuracy and computation time.

In practice, the magnetic field can be analytically computed by the code itself, from a built-in library, for a wide range of magnets (the code also includes electrostatic elements) [3]. The field and its derivatives are computed at the particle position at each step and used in equations 3.3 and 3.4. For instance, the Zgoubi element `'MULTIPOL'` produces a superposition of multipolar magnetic fields and is used for the AGS lattice to simulate sextupoles and dipole correctors. Alternatively, field maps of magnetic elements can be used, either simulated using a magnet simulation code or measured from a real magnet. Zgoubi is capable of handling different types of field maps, from 1-D to 3-D, by assuming different symmetries of the field and using the Maxwell's equations. This is particularly useful in the case of the AGS where 2-D measured field maps of the main magnets and 3-D simulated field maps of the snakes are available. For tracking through field maps the Zgoubi element `'TOSCA'` is used and the code places a grid (generally 3x3 in 2-D and 3x3x3 in 3-D) centered closest to the particle position [3]. The field and its derivatives are computed using the field at the field map nodes and the Maxwell equations.

3.2.2 Spin Dynamics

The spin vector $\vec{S}$ (defined Section 2.3) is transported using the same numerical method as the particle position [64]:

$$\vec{S}(M_1) = \vec{S}(M_0) + \vec{S}'(M_0)\Delta s + \vec{S}''(M_0)\frac{\Delta s^2}{2!} + \cdots + \vec{S}^{(4)}(M_0)\frac{\Delta s^4}{4!} \tag{3.5}$$

where the derivatives $\vec{S}^{(n)}$ are determined from recursive differentiation of the Thomas-BMT equation (Eq. 2.65). This also uses the magnetic field and its spacial derivatives at M_0 (see equation 2.65).

3.2.3 Longitudinal Dynamics

Longitudinal dynamics is handled through equations 3.3 to 3.4 when the particle rigidity changes. In the AGS the particles get accelerated when traveling across one of the RF cavities. In the Zgoubi model of the AGS, changes in energy are simulated using a single longitudinal kick once per turn. A Zgoubi element `'CAVITE'`, located at the end of straight section L20, simulates the combined effect of all cavities used in the machine since the phase slip per turn remains very small [32].

The `'CAVITE'` input data describes the RF wave to be used and includes the length of the closed orbit. When a particle crosses the `'CAVITE'` element at turn i the code transforms its path length into the phase difference relative to the RF wave that the particle accumulated between turns $i-1$ and i. The longitudinal phase of the particle is therefore updated at every turn and each particle receives a longitudinal kick according to the time dependence of the RF wave. Longitudinal dynamics naturally include all high orders due to transverse dynamics such as non linear momentum compaction factors and synchro-betatron coupling.

3.3 Development of the Zgoubi Model of the AGS

3.3.1 Bare Model

As the AGS uses combined function dipoles, most of the beam focusing is achieved by these magnets [61]. Therefore correct modelisation of the AGS main magnets is critical to realistically simulate beam and spin dynamics.

3.3.1.1 Direct Tracking through Measured Field Maps of the Main Magnets

The AGS main magnets are combined function C-shaped magnets with two different lengths. Depending on the side of the wide gap, the magnets are called open (A and B-type) or closed (C-type), as illustrated in Figure 2.3. The iron of A-type and C-type is 90 inches long, while B-type is 75 inches. Point-to-point field maps were obtained for a single A-type and a single C-type magnet, from the fringe field region to the middle of the magnet, using a hall probe. The maps of the vertical field component are produced in the median plane of the magnet and over 13 different currents from 15 to $5850A$. The original mesh size of these maps was $\Delta x = 0.1$inch in the transverse direction and $\Delta s = 0.25$inch or $\Delta s = 1$inch in the longitudinal one, depending on the gradient. However, Zgoubi requires a uniform mesh, so the maps were converted to a constant longitudinal mesh of $\Delta s = 0.25$inch [68]. The field maps of the B-type magnets are derived by shortening the central region of the A-type maps. The two functions of each magnet type (focusing and defocusing) are obtained by flipping the map with respect to the longitudinal axis. Analysis of these data yielded the excitation functions [23] and the harmonic coefficients [27, 69] of the main magnets which have been used so far in every model of the AGS. The measured field maps use a coordinate system called the "Socket System", whereas in Zgoubi (and MADX as well) the origin of the reference frame is taken on the OCO [22]. The different coordinate systems and their relationship are detailed in references [30,70]. Moreover, the AGS model in Zgoubi using the measured field maps,

Table 3.1 List of elements used in the Zgoubi model of the AGS.

AGS element	Zgoubi element	options	thesis reference	Zgoubi user's guide	label associated
main magnet	AGSMM	dk_0, dk_1, dk_2, misalignment and backleg winding	p.72	p.181	AGSMM_
	TOSCA	dk_0, dk_1, dk_2 and misalignment	p.69	p.269	AGSMM_
quadrupole	AGSQUAD	additional winding and misalignment	p.73	p.182	QH_, QV_ or QTHIN
sextuple	MULTIPOL	misalignment	p.74	p.236	SXH_ or SXV_
cold/warm sake	TOSCA	misalignment	p.75	p.269	CSNK or WSNK
accelerating cavity	CAVITE	none	p.68	p.194	CAVITE

employs the same conventions as the classical MADX model: a counter-clockwise circulation of the particles and the positive transverse direction toward the center of the ring. In order to go from one system to the other, at the entrance and exit of the main magnet field maps, the Zgoubi AGS lattice uses the element `'CHANGREF'` [3]. An example is given in appendix A for the case of an A-type magnet.

Tracking in the bare AGS using the measured field maps of the main magnets showed good optical results. However, long term trackings showed that the single particle emittance is not conserved at large amplitudes, likely due to the lack of smoothness of the measured field maps [69]. Direct tracking through the measured field maps provides a realistic optics since high order field components or fringe fields are included. However, long term stability is very important for spin tracking in the AGS (typically more than 150,000 turns in the 240 main magnets of the ring for a complete acceleration cycle), therefore the use of an analytical model for the main magnet is required.

3.3.1.2 Multipole Model of the Main Magnets

Multipolar field components were extracted from the measured field maps of the main magnets [27, 71]. Convenient polynomial functions were generated to determine the multipolar field components as a function of the magnet excitation current or equilibrium proton momentum. These functions are used in the MADX model of the AGS main magnets and are commonly referred to as Bleser's polynomials. Since available documentation does not detail the method used to extract these data, it was proposed to use the Zgoubi code to redo the exercise. Tracking with the Zgoubi code through the measured field maps provided the quadrupole and sextupole strengths, as a function of the magnet excitation current and for proton circulating on the OCO [69]. Figure 3.3 shows good agreement between the historical polynomials from reference [27] and the new values computed using the Zgoubi code. Appendix B provides all the computed values for the 8 different

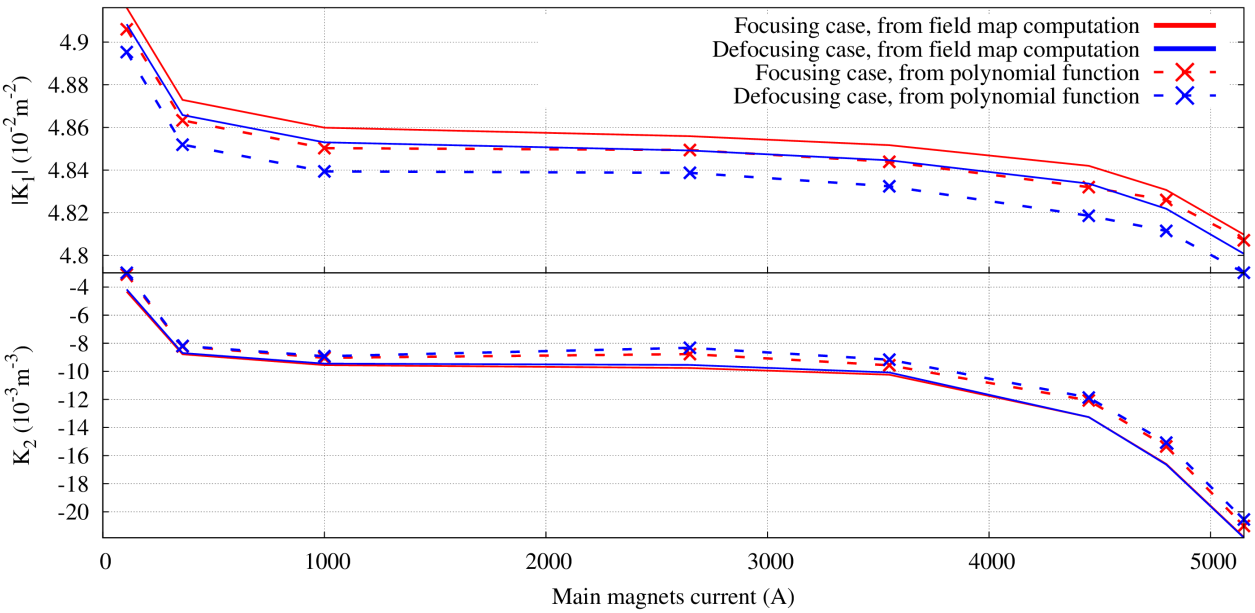

Figure 3.3 Quadrupole (top plot) and sextupole (bottom plot) strengths as a function of the magnet current for a C-type magnet.

main magnet currents in the relevant range of energy.

A new Zgoubi element `'AGSMM'` was developed for dedicated simulation of the AGS main magnets [72]. The module is based on Bleser's polynomials, as the MADX model, to provide the same results as the MADX model. It generates a superposition of dipole, quadrupole and sextupole fields. The element length corresponds to the magnetic length of the main magnet, namely 79 or 94 inches. Bleser's polynomials are included in the routine and generate the correct fields associated with the lattice rigidity [68, 72]. This element also allows advanced manipulation of each main magnet via [3]:

- relative changes of the field components. The dipole, quadrupole and sextupole fields can be independently modified on each magnet.
- introducing backleg windings. Up to 3 different backleg windings can be activated on each magnet.

- controlling fringe field region. Although hard edge model is generally used, it is possible to control the fringe field fall-off.
- translating and rotating the magnet. This allows surveyed magnets' misalignments and roll to be introduced in the model.

Table 3.2 compares the tunes and chromaticities predicted by different models with measurements taken at the proton injection energy using a flat magnet cycle. Although all the models are consistent with the measurements, none perfectly predicts the machine behavior with sufficient accuracy. For accurate simulation of the AGS behavior, in particular for long term multiparticle spin tracking, simulation parameters have to be much closer to the measurements.

Table 3.2 Comparison of AGS bare models with machine measurements taken on January 15, 2012, at injection energy.

Source	Q_x	Q_y	Q'_x	Q'_y
Machine measurement	8.726	8.771	-13.07	-4.55
MADX model	8.711	8.765	-22.73	1.73
Zgoubi with field maps	8.734	8.774	-26.84	1.44
Zgoubi with `'AGSMM'`	8.711	8.765	-20.86	1.60

3.3.2 Comprehensive AGS Model

3.3.2.1 AGS Quadrupoles and Sextupoles

Dedicated quadrupoles and sextupoles are respectively used to control the tunes and chromaticities of the AGS. Transfer functions to compute the field generated by these magnets from the excitation currents are well known [53, 54]. The transfer functions are used by the MADX model and were introduced in the Zgoubi source code.

A new Zgoubi element named `'AGSQUAD'` was developed to conveniently simulate the AGS quadrupoles, based on the same transfer functions as used by the MADX model. The element

simulates the quadrupole field the same way as the 'MULTIPOL' Zgoubi element [3]. Input data consists of the number of amperes provided to each magnet by one or more power supplies. Some of the high field quadrupoles can be excited by more than one source of current, for instance the quadrupoles used to compensate the optical effects of the two Siberian snakes. The code reads the label associated to the 'AGSQUAD' to determine the element behavior, as follow:

- if the label starts with QH_, QV_ the element describes one of the high field quadrupoles used to control the AGS tunes and the associated transfer function is used [53].
- if the label starts with QP_ this describes a polarization quadrupole, similar to high field tune quadrupoles but with half the number of coil turns.
- if the label is QH_A17, QP_B03 or QH_E17 the magnet is powered by two independent power supplies. These magnets are used to compensate the optical effects of the snakes and each possesses a floating power supply. In practice, the code computes the total magnet excitation from the sum of the floating power supply current and the tune power supply.
- if the label starts by Qthin_ the element describes one of the thin quadrupoles used to compensate the Siberian snakes' optical effects and the according transfer function is used [55].
- if the label starts by QGTR the element describes one of the high field quadrupoles used for transition gamma crossing and the same transfer function as for the high field quads is used.

Sextupoles used in the AGS to control the chromaticity are simulated using the general Zgoubi element 'MULTIPOL'. The sextupole strength is given as input to the element that generates the corresponding sextupole field. It is important to note that the quadrupoles provide a purely quadrupolar field and the sextupoles a purely sextupolar field, both centered around the OCO by default.

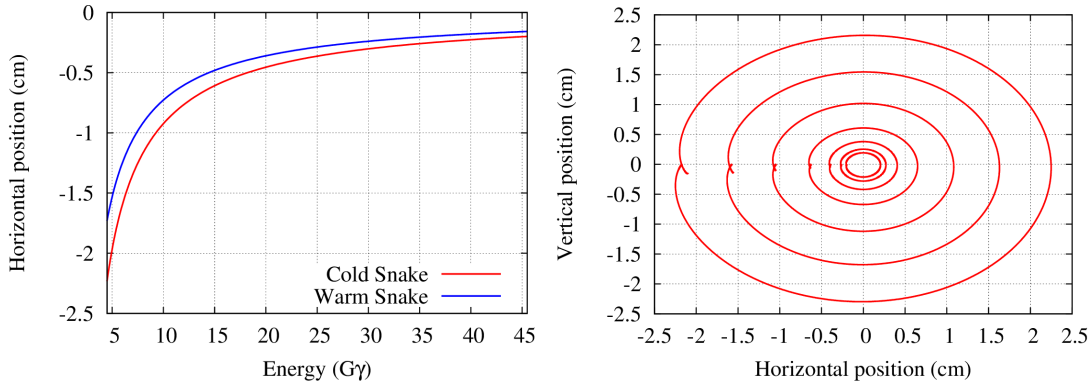

(a) (b)

Figure 3.4 Horizontal position at the entrance of each snake (a). Trajectories in the cold snake projected in the $(\vec{x},\vec{y})$ plane for different energies of the reference particle from $G\gamma = 4.5$ (outer helix) to $G\gamma = 45.5$ (inner helix) (b).

3.3.2.2 Snake Field Maps

Modeling of the AGS snakes is critical for realistic simulations. The strong optical effect of the snakes in the AGS at low energy [56] makes the choice of the snakes model particularly important for realistic simulations of the AGS acceleration cycle. With the capabilities of the Zgoubi code to directly track through field maps [64, 65], tracking in the AGS using field maps of the snakes was initiated [73]. It is important to note that both snakes are run at constant current [56], therefore a single field map of each snake is used.

Modeling of the snakes has always involved tracking through field maps [57, 74]. However, their introduction in the Zgoubi model of the AGS posed numerous problems, in particular at low energy, in terms of beam dynamics behavior such as losses of particles during tracking or variations of the single particle invariant [75]. Additionally, the original field maps of the snakes, were recomputed using the TOSCA code [76].

In the model of the AGS using the field maps of the snakes the particle trajectory inside the element is centered around the snake axis. A transverse horizontal translation is used before each field map to center the trajectory of the reference particle inside the magnet. The transverse shift

is reversed as the particle exits the field map. Figure 3.4 shows that the translation maintains the helical trajectory of the reference particle centered on the snake axis. However, Figure 3.4(b) shows that the exit point is not exactly aligned with the entrance one. The snakes are not completely transparent with respect to the orbit in the AGS: they have a non-negligible dipole effect on the beam that creates a distortion of the closed orbit, particularly at low energy. To simplify the model and make the closed orbit coincide with the OCO in the rest of the ring, a set of 4 small kicks at the downstream end of each field map are used to correct this dipole effect.

3.3.3 Zgoubi Developments for the AGS Online Model

As shown in Table 3.2 none of the models available perfectly predicts the measured tunes or chromaticities. The discrepancies between measured and predicted tunes and chromaticities can be attributed to the simplifications used in the AGS Zgoubi model :

- The closed orbit in the AGS Zgoubi model always follows the *OCO*. All alignment and magnetic errors are ignored, as well as the effect of dipole correctors and backleg windings. This can affect the tune through feed down of the sextupole field when the beam crosses a sextupole off center.

- The beam is always considered to follow the reference momentum defined by the main magnets current in the AGS Zgoubi model. In reality, the measured average radial beam position can vary by up to a few millimeters during the acceleration cycle. Therefore, the tune shift due to chromaticity when the beam is off-centered is ignored.

- While the main magnet model is based on DC magnetic measurement, effects of the fast ramping rate, up to $2.5\,\mathrm{T.s}^{-1}$, used to accelerate polarized protons are neglected. However, it is known that Eddy currents on the vacuum chamber wall, due to ramping dipole field, create strong enough sextupole field to influence the lattice chromaticity, particularly at low

energy [77]. In the example Table 3.2, this effect is not accounted for and the main magnet is considered at constant current.

It was decided to only modify the quadrupole and sextupole components in the AGS main magnets `'AGSMM'` model to respectively control the tunes and chromaticities and recover measured values. The AGS main magnets can be separated into two families, focusing and defocusing. This choice, although arbitrary, allows for maximum effectiveness of small changes in the quadrupole and sextupole fields of each family to adjust the tunes and chromaticities, respectively.

- Matching of the two transverse tunes is achieved by adjusting quadrupole field strengths in the two main magnet families, through relative variations called $dk_1(f)$ and $dk_1(d)$. The small changes involved do not significantly change the particles trajectory in the main magnets neither the closed orbit.

- Modification of the sextupole strength in the two main magnet families allows control of the lattice chromaticities, through relative variations $dk_2(f)$ and $dk_2(d)$. Since the closed orbit in the model always matches the *OCO*, small modifications of the sextupole field in the main magnets does not change the transverse tunes nor the closed orbit.

Matching is automatically done using the `FIT` procedure of the Zgoubi code. In the case of the bare machine at low energy, with parameters as shown in Table 3.2, the required changes in the `AGSMM` model are:

- $dk_1(f) = 0.12\,\%$ and $dk_1(d) = 0.10\,\%$.

- $dk_2(f) = -0.75$ and $dk_2(d) = -0.42$.

The relative changes applied to the quadrupole field are much smaller than 1 % and this is generally the case whatever the AGS configuration. The relative changes required to match the measured chromaticities are much larger, but the sextupole field components are themselves weak anyway.

3.4 The Zgoubi Code as Online Model of the AGS

Predicting AGS tunes and chromaticities is particularly complex in the polarized protons configuration, due to the optical effects of the snakes. As shown in Section 3.1.1.2, the AGS control system uses a linear relation that does not include the effects of the snakes on the machine optics. Changes in the machine optics using the snake compensation quadrupoles are also ignored. Online modeling of the AGS aims to provide a single tool allowing machine operators to predict and control the AGS with increasing accuracy based on staged refinement of the model. The Zgoubi code should be able to account for all the effects mentioned above.

The approximations used in the AGS Zgoubi online model were already discussed in Section 3.3. The online model currently provides optics data along the ramp but cannot directly be used to set machine parameters. Here it will be used for setup of multiparticle spin tracking.

3.4.1 The *ZgoubiFromSnaprampCmd* Command

The development of the AGS Zgoubi online model started by mirroring the MADX online model and associated command called *MadxFromSnaprampCmd*. *ZgoubiFromSnaprampCmd* uses an input file (*ZgoubiFromSnaprampCmd.in*) organized around keywords signaled by square brackets. An example is given in Appendix C. The input file contains data required for the model computations:

- the directory of the snapramp to be used, associated to the keyword `[SNAP RAMP DIRECTORY]`.
- the location of the Zgoubi lattice file to be used, associated to the keyword `[TEMPLATE DATA FILE]`.
- the list or the range of AGS timings at which the modelisation is required, associated to the keyword `[TIMINGS]`.

The input file can also contain optional information to be used during the model execution:

- the model to be used for the AGS main magnets, by default, is the `'AGSMM'` model, but the measured field maps can also be used. This option is associated with the keyword `[AGS MODEL DATA]`.

- to plot and possibly show optical information, such as the beta functions along the lattice at a given energy (keyword `[GET BETA FUNCTIONS]`).

- to adjust the modeled tunes using measured data, or a particular tune couple (Q_x, Q_y), and following the procedure detailed in Section 3.3.3, associated to the keyword `[FIT]`.

Figure 3.5 shows the evolution of the AGS tunes along a typical acceleration cycle of polarized protons with injection from the AGS Booster at 145 ms and maximum energy reached at 580 ms.

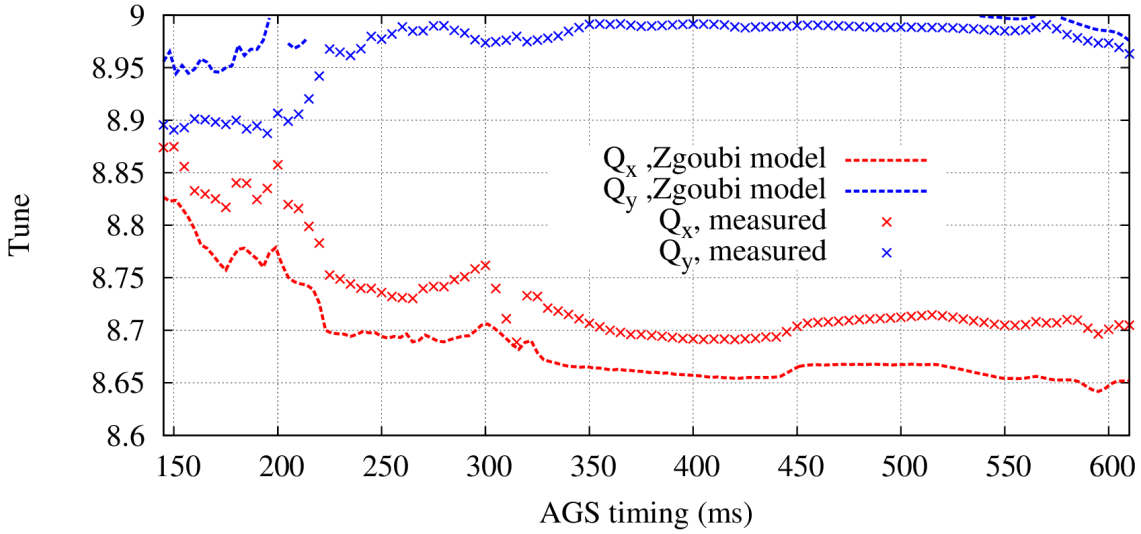

Figure 3.5 Measured tunes and predicted tunes by the AGS Zgoubi online model along the polarized protons acceleration cycle on April 14$^{\text{th}}$, 2013. Statistical errors on the measured tunes are minimal and cannot be seen in the above plot.

Figure 3.6 shows the relative changes of the quadrupole field ($dk_1(f)$ and $dk_1(d)$) in the two families of main magnets required to match the modeled tunes to the measurements. The relative changes required are always very small and usually below 0.35 %. It is particularly important to achieve realistic tunes along the full cycle for both spin and beam dynamics accurate modeling.

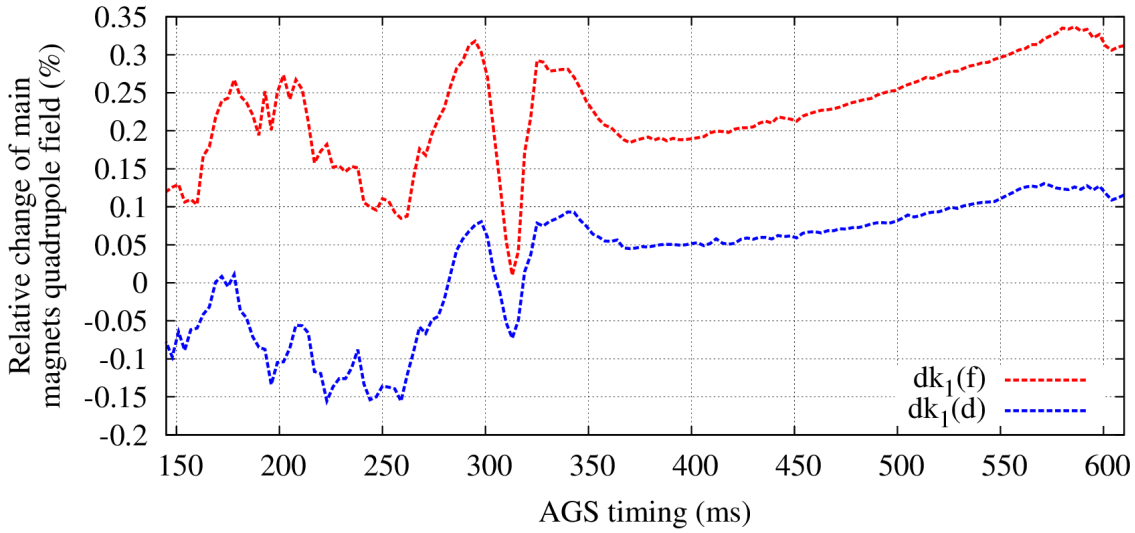

Figure 3.6 Required relative changes to the two main magnets families to match measured tunes.

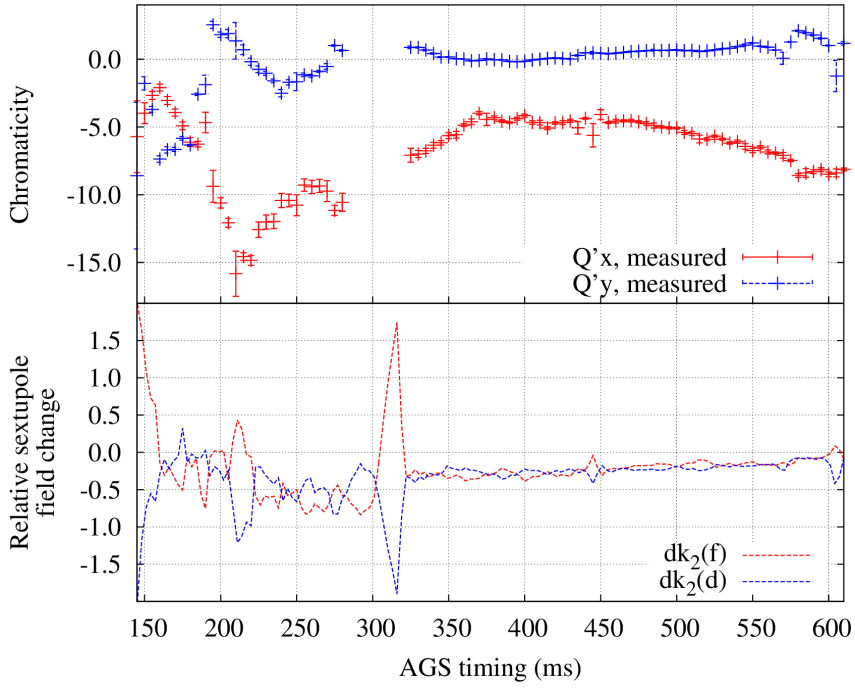

Figure 3.7 Measured chromaticity along the polarized protons acceleration cycle on April 14th, 2013 and required relative changes of the main magnets sextupole field to match the measurements.

Figure 3.7 shows the measured chromaticity along the acceleration cycle, in the regular polarized proton setup. One can see missing data points around 300 ms due to the transition jump, perturbing the measurement of the chromaticity. The relative changes showed in Figure 3.7 allow the modeled chromaticities to perfectly match the measured values. When the model is computed between two timings where measured values are available, the target tunes and chromaticities are determined by interpolation from the measured data.

A post-treatment command was developed to compile all the information regarding the lattice for each timing. The command also gathers the dk_1 and dk_2 required to match the measured tune and chromaticities. All the information is written in a single file, ready for use in multiturn tracking along the ramp and using the Zgoubi code. This is addressed further in Chapter 4.

Chapter 4

Long Term Beam Tracking in the AGS Using the Zgoubi Code

Understanding the sources of depolarization in the AGS is critical to improve the AGS polarized proton performance. Experimental results show that some amount of transverse beam emittance growth occurs during acceleration of polarized protons [5]. Single particle and multiturn tracking codes can be used to investigate both questions. The Zgoubi model of the AGS, detailed in Chapter 3, provides a realistic representation of the AGS, within the approximations mentioned, to explore and improve both spin and beam dynamics.

This chapter will review the process involved in the setup and analysis of the tracking simulations. The tools developed for this purpose will be presented and results from the Zgoubi code will be compared to experimental data.

4.1 Setup and Parallelization of Multiturn Tracking

Complete tracking of the acceleration of polarized protons in the AGS takes approximately 150,000 turns from injection at $G\gamma = 4.5$ up to extraction at $G\gamma = 45.5$, for typical acceleration ramp

settings. New methods for controlling elements of the Zgoubi AGS lattice were introduced in order to continuously change the AGS optics as a function of the lattice rigidity.

4.1.1 Optics Setup for Multiturn Tracking

Information generated along an AGS ramp by the *ZgoubiFromSnaprampCmd* are compiled into a single file. The file created contains the behavior of each magnet or power supply in the AGS as a function of the AGS time or as a function of the equilibrium proton momentum determined from the AGS main magnet current. The file also contains the dk_1 and dk_2 computed by the *ZgoubiFromSnaprampCmd* (see Chapter 3).

Setup usually consists in computing the AGS optics every 3 ms along the ramp. The AGS lattice makes use of the `SCALING` element in mode `1.12`, allowing to interpolate data from a file using the current lattice rigidity and adequately modify the designated parameter in a family of elements [78]. This allows for the parameters of each element to be reevaluated at every turn by Zgoubi and updated using the current lattice rigidity and the data file provided by *ZgoubiFromSnaprampCmd*.

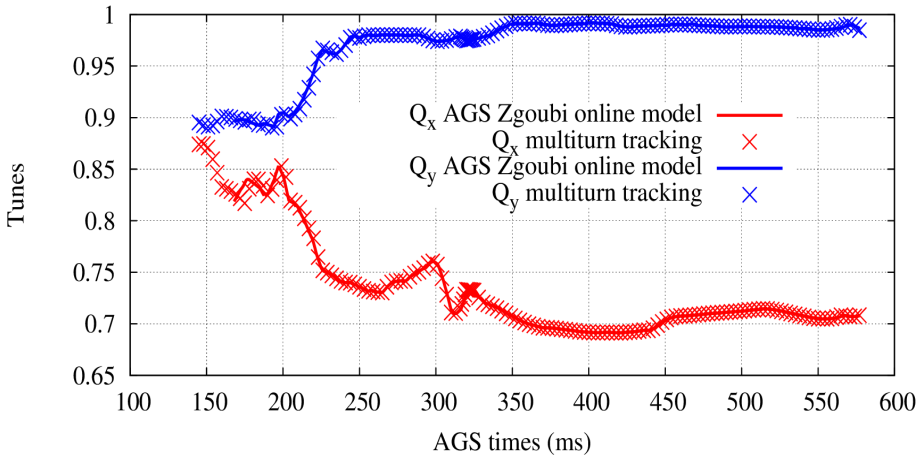

Figure 4.1 Tunes matched to measured data by the AGS Zgoubi online model compared to the tunes from multiturn tracking data for an on-momentum particle.

Figure 4.1 shows the evolution of the transverse tunes from a single particle multiturn tracking

simulation. Tunes are computed by DFT[1] of the transverse motion using a post-processing code from the Zgoubi toolbox [78]: *TunesFromFai*. The particle tunes during tracking are equal to the tunes prior obtained by *ZgoubiFromSnaprampCmd*. This step is important to assess the accuracy of the multiturn simulation.

Evolution of the chromaticity during tracking is also in agreement with the values set up by *ZgoubiFromSnaprampCmd*. Optics generated by *ZgoubiFromSnaprampCmd* is precisely reproduced during the multiturn tracking and changes according to the AGS setup as a function of the energy.

4.1.1.1 Tune Jump Model

The AGS tune jumps system is made of two quadrupoles located on SS-I05 and SS-J05. Each quadrupole can change the horizontal tune by $\Delta Q_x = +0.02$ within $100\,\mu$s [79], up to $G\gamma = 45.5$, effectively accelerating the crossing of horizontal intrinsic resonances(Sec. 2.5.1).

Setup of the tune jumps for multiturn tracking is done by locating each horizontal intrinsic resonance. Peak theoretical effectiveness of the tune jump is reached by crossing the horizontal intrinsic resonance when the tune jump system is half-way to its maximum, *i.e.* $50\,\mu$s after the start of the ramp and generating a tune shift of $\Delta Q_x = +0.02$. The associated resonant condition is:

$$Q_S \pm (Q_x + 0.02) = I \tag{4.1}$$

with I an integer and Q_S the spin tune. The location of each resonance is determined using the theoretical evolution of the spin tune (Eq. 2.117) and the horizontal tune.

In the AGS the strength of each of the two jump quadrupole is experimentally adjusted so as to provide half the total horizontal tune shift. For multiturn tracking, the strength of each quadrupole is determined to provide a horizontal tune shift of $\Delta Q_x = +0.02$ with both quadrupoles

[1] Discrete Fourier Transform

synchronized. The Zgoubi model makes use of option `1.13` of the `SCALING` element to control each quadrupole as a function of real time, allowing accurate control over the pulse shape and timing. The tune jump pulse shape is simulated using a linear ramp to full strength within 100 μs [78]. The effects of the pulse shape were not investigated, but the linear approximation is close to the real pulse shape.

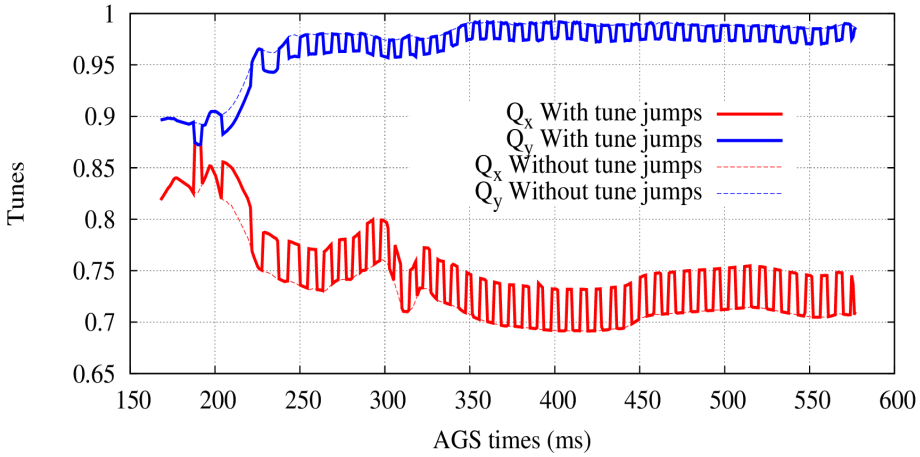

Figure 4.2 Transverse tunes along a multiturn tracking with and without tune jumps.

Figure 4.2 shows the evolution of the transverse tunes as a function of the AGS timing when the tune jumps are active. The tune shifts induced by the tune jumps system are $\Delta Q_x = +0.04$ and $\Delta Q_y = -0.02$. The quadrupoles are powered up, or jumped up, when the *plus* resonance ($Q_S + Q_x = I$) is crossed. Reciprocally, the system *jumps down* when the *minus* resonance ($Q_S - Q_x = I$) is crossed, allowing the vertical tune to be maximal (*i.e.* closer to 9, further away from $Q_S \pm Q_y =$ integer) when vertical intrinsic resonances are crossed around integer values of $G\gamma$.

4.1.2 Acceleration System for Multiturn Tracking

The RF system, and in particular the synchronous phase, is generally used to control the radial beam position during acceleration of polarized protons [80]. This process cannot be used for simulations as described since the parallelization to track multiple particles is achieved without

communication between each thread (see Section 4.1.4).

To simulate realistic variations of the synchronous phase, we make use of the intrinsic reproducibility of the lattice conditions. Using the AGS lattice file, the exact one turn path length of the reference particle is determined as a function of the lattice rigidity. Figure 4.3 shows large evolution of the reference particle path length, due to its shrinking inside the Siberian snakes and downstream of the snakes where the dipole effect of the snakes are corrected.

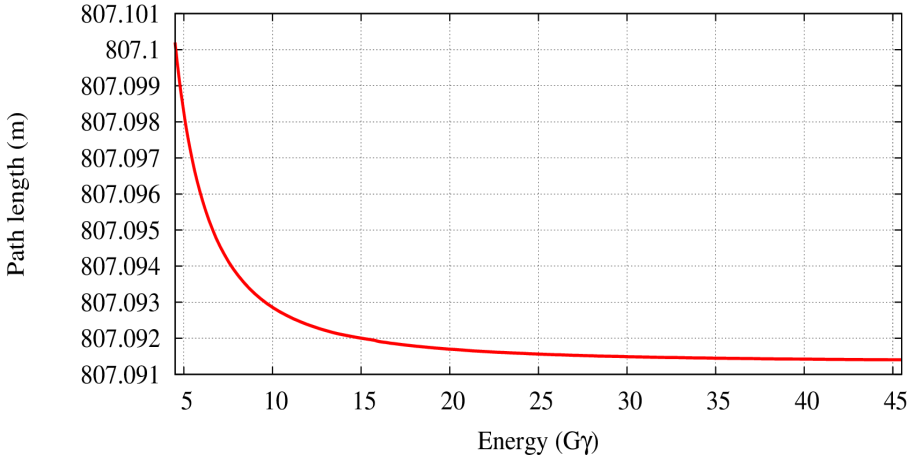

Figure 4.3 Evolution of the reference particle path length as a function of the AGS energy.

Located at the end of each machine turn, the Zgoubi `CAVITE` element is designed to increase the particle forward momentum, based on provided RF parameters and particle phase ϕ. The particle phase relative to the RF wave is updated using the phase change $\Delta\phi$ given by:

$$\Delta\phi = \left(\frac{C_i}{\beta_i c} - \frac{C_{REF}}{\beta_{REF} c}\right)\left(2\pi h \frac{\beta_{REF} c}{C_{REF}}\right) + \Delta\phi_s \tag{4.2}$$

where:

- C_i and $\beta_i c$ are, respectively, the path length of the particle and its velocity for the previous turn.
- C_{REF} and $\beta_{REF} c$ are, respectively, the reference path length and velocity associated to the

equilibrium momentum.

- $\Delta\phi_s$ is the change in synchronous phase between the previous and the current turn.
- h is the RF harmonic number. In the AGS, $h = 8$ for the acceleration of polarized protons.

The tracked particle then receives a longitudinal kick ΔE using the provided RF voltage V_{RF} and the known proton charge q (Eq. 2.51):

$$\Delta E = qV_{RF} \sin\phi \tag{4.3}$$

The acceleration rate is strictly determined by logged main magnets currents since the multiturn tracking maintains the beam around the equilibrium momentum. Typical acceleration rate for polarized protons during AGS operations is shown in Figure 2.6.

Due to the intrinsic behavior of the `CAVITE` Zgoubi element when the synchronous phase is slowly changed, the parameter ϕ_s in equation 4.2 might introduce numerical noise in the evolution of the particle phase due to numerical accuracy. A simple check consists of following the momentum deviation of the reference particle along the multiturn tracking. Figure 4.4 shows the particle launched on-momentum starting to oscillate around the equilibrium momentum. The oscillation is introduced by numerical accuracy and the period follows equation 2.59. However, the amplitude of oscillations remains very small compared to the typical momentum spread for realistic beam conditions. Therefore, the Zgoubi numerical accuracy is good enough for the tracking conditions used in this study.

4.1.2.1 Transition Gamma (γ_{tr}) Crossing

Crossing of the transition region is crucial for tracking realistic beams in the AGS. In the considered lattice, 6 high field quadrupoles called gamma transition quadrupoles are located in SS17 every other superperiod and powered before transition then quickly cut-off to accelerate the transition

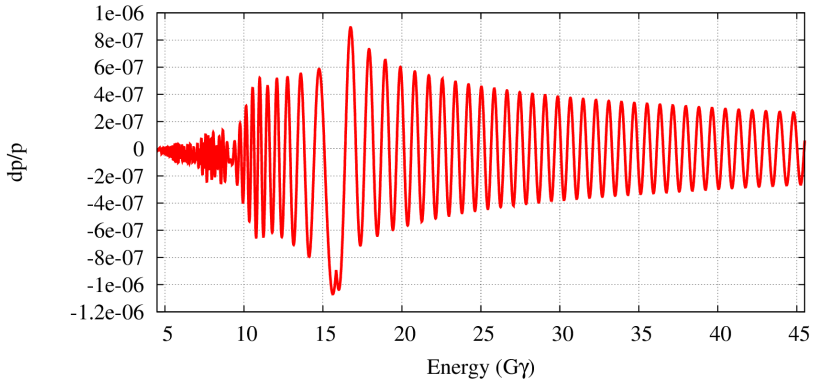

Figure 4.4 Evolution of the momentum deviation from the equilibrium momentum of the reference particle during a multiturn tracking.

crossing. In the Zgoubi model, the gamma transition quadrupoles are present and their respective strengths are derived from logged currents, in the same way as for all other quadrupoles. Figure

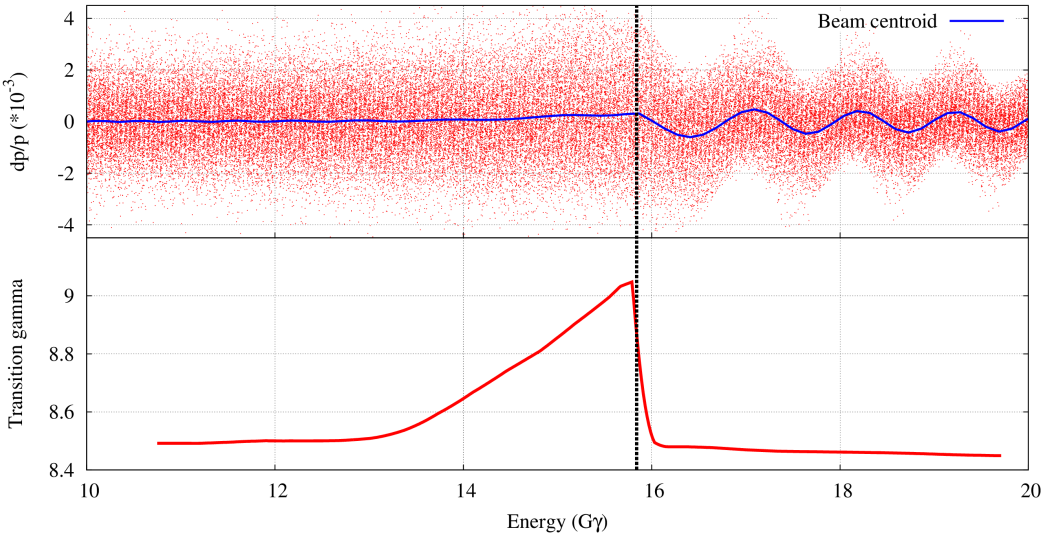

Figure 4.5 Evolution of the momentum distribution in a typical beam tracking and variation of the transition gamma across transition using the Zgoubi code. The black line marks the crossing of the transition.

4.5 shows the gamma transition increasing before being abruptly cut-off for transition crossing, effectively dropping by about 90% in 2 ms. The RF synchronous phase used by the Zgoubi code is instantaneously switched at $G\gamma = 15.8$. After transition some dipole oscillation of the beam

can be seen in Figure 4.5, primarily due to particle losses related to the particle momentum shift (Figure 4.4 confirms that on-momentum particles stay on-momentum after transition). Section 4.4.1.2 details the sources of the losses.

4.1.3 Beam Conditions for Zgoubi Beam Tracking

Realistic simulation of the AGS also requires accurate initial particle distributions. The 6-D distributions used for beam tracking with the Zgoubi code are generated externally by a random Gaussian generator. The particle distributions are always cut at $\pm 3\sigma$ in profile, which proves to be a good compromise. Typical transverse emittances range from 4 to $10\,\pi$ mm.mrad at injection to around $20\,\pi$ mm.mrad at extraction in the vertical plane [81]. Measured horizontal emittance are estimated between $9\,\pi$ mm.mrad at injection and $12\,\pi$ mm.mrad at extraction. Emittances are usually given as normalized (z stands for x or y):

$$\varepsilon_z^N = (\beta\gamma)\,\varepsilon_z \tag{4.4}$$

and containing 95 % of the beam, which relates to the *RMS* emittance of a Gaussian beam by:

$$\varepsilon_z^{95\,\%} = 6\,\varepsilon_z^{RMS} \tag{4.5}$$

The longitudinal distribution is based on RF parameters and bunch length, as measured at AGS extraction. Bunch profiles measured at extraction, using the AGS WCM[1] during Run12 under typical operations conditions and fitted to a Gaussian function, provide a bunch length of $l_{RMS} = 6.58$ ns. Using the RF parameters at that time ($V_{RF} = 240$ kV and $h = 8$), the calculated associated energy spread is $E_{RMS} = 11.78$ MeV. Therefore, the longitudinal emittance at extraction

[1] Wall Current Monitor

is:

$$\varepsilon_l^{95\%} = 6\pi E_{RMS} l_{RMS} = 1.46\,\text{eV.s} \tag{4.6}$$

4.1.4 Pre-Processing of Parallelized Zgoubi Tracking

The Zgoubi code tracks particles that do not interact between each other. Therefore the simplest approach to parallelize Zgoubi tracking consists of tracking one particle per available computation thread and combining the results during post-processing. The parallelization is commonly referred to as *embarrassingly parallel* and presents the advantage of avoiding inter-threads communications during computation, which can be the source of inefficiency. The gain is also perfectly linear and the computation time per particle is constant. Multiple single particle tracking using the Zgoubi code is done using the NERSC[1] supercomputing resources.

The pre-processing consists of all the steps required before the multiparticle tracking simulation is run on the supercomputer. In logical order, the pre-processing:

- generates the lattice, in particular the file containing the behavior of each AGS power supply and possibly the relative changes of the quadrupole and sextupole fields of the main magnets. The method detailed in Section 3.4 generates realistic and stable optics along the AGS ramp.
- generates the acceleration rate along the ramp: a file containing realistic acceleration, RF parameters and path length of the reference particle in the model is generated. Figure 4.4 is generated to control the correct longitudinal behavior of the synchronous particle along the tracking.
- generates the particle distributions: Twiss parameters and RF parameters at the start of the tracking are used to generate realistic and matched particle distributions.

[1] National Energy Research Scientific Computing Center

- generates the tune jump timing: the energy and horizontal tune as a function of time are used to generate perfectly timed tune jumps along the AGS ramp. The tune jumps can be shifted in time, removed or generally altered to investigate their effects.

- transfers all required files to the NERSC computing facility and prepares the Zgoubi input files.

After these steps, each tracking job is split into groups of (usually) 192 particles each and ran on 8 nodes[1]. Each group is then associated to a computation job to effectively track each particle. The number of particles per group was optimized to avoid in-out disk access overloads, susceptible to occur when a large number of tracking jobs start at the same time. The group size also allows for minimum waiting time in the supercomputer queue, which generally quickly grows with the number of nodes to be used. Tracking data are saved at regular intervals, usually once every 21 turns. The number of particle simulated is only limited by the available resources, the simulations are scalable to any number of particle. However, in the case of the AGS, simulation of one machine turn for one particle on a single modern computer core takes around 30 ms. We will see Section 4.4.0.1 that the number of particle per simulation was optimized to provide accurate results with a minimum sample size.

Once completed, the tracking simulation requires multiple post-processing steps to extract all relevant quantities from the thousands of particles tracked.

4.2 Post-Processing of Tracking Data

Post-processing of the Zgoubi tracking data is critical to present and understand the evolution of the relevant quantities along the tracking. One of the first and very likely most interesting quantities to look at is the polarization. However, due to the partial snake configuration (see Section 2.4),

[1]The node is the smallest allocatable computation unit and composed here of 24 physical computing cores.

the average of the vertical spin component is not a convenient quantity to study depolarization. Figure 4.6 does not show depolarization during acceleration. The polarization is not defined by the

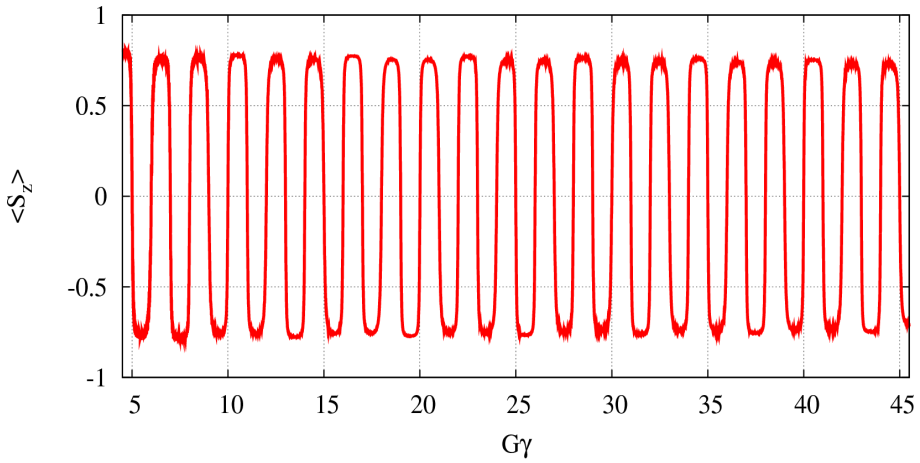

Figure 4.6 Evolution of the average vertical spin component over a typical multiparticle tracking.

projection of the spin vectors on the vertical axis but by the projection on the stable spin direction associated to each particle. Here we define the average beam polarization $< P >$ as the projection of the spin vector on the stable spin direction $\vec{n}_0$ on the closed orbit, averaged over the N particles of the beam:

$$< P >= \sum_N \vec{S}_i \vec{n}_0 \tag{4.7}$$

Typical evolution of the average polarization during a multiturn tracking is showed Figure 4.7. The depolarizations can easily be seen when the average beam polarization drops. It is important to note that the polarization dips observed at every integer value of $G\gamma$ is due to the different momenta of the beam. Due to the momentum spread of the beam, each particle is at a different stage of the spin flip and the projection of the spin vectors on the $\vec{n}_0$ of the synchronous particle drops while no polarization is lost.

In details, Figure 4.7 shows a strong polarization loss around $G\gamma = 5$. This depolarization is mainly due to the crossing of the two weak vertical intrinsic resonances around $G\gamma = 5$ and more

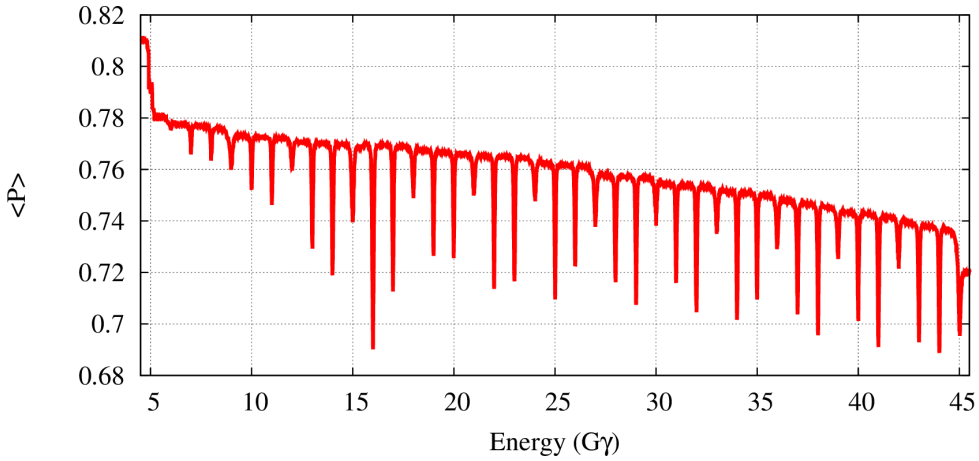

Figure 4.7 Average of the projected spin vector on the stable spin direction on the closed orbit during a typical multiturn tracking.

detail can be found Section 5.3. The depolarization seen across $G\gamma = 45$ is due to the crossing of the strong vertical intrinsic resonance $36 + Q_y$. However, in typical beam and machine conditions no depolarization is observed across $G\gamma = 45$.

4.2.1 Polarization Profile

In the AGS, one of the most relevant quantities measured is not the average polarization over the beam but the polarization profile. The strength of an intrinsic spin resonance depends on the *Courant-Snyder* invariant (Eq. 2.108), hence the depolarization experienced by a particle across such a spin resonance also depends on the single particle invariant. The crossing of an intrinsic resonance can result in the particles at larger amplitude being depolarized while the center of the beam remains polarized, creating a profile of the polarization across the beam.

The polarization profile is characterized by the R-value, using σ_P and σ_I respectively the standard deviations of the polarization and beam intensity Gaussians fits [41]:

$$R = \left(\frac{\sigma_P}{\sigma_I}\right)^2 \tag{4.8}$$

Figure 4.8 shows the result of a typical horizontal polarization profile. Unlike the average polarization, the R-value gives an indication about the source of depolarization. For instance, an increase in the horizontal polarization profile (seen through the rise of the horizontal R-value) is the sign of depolarization due to horizontal intrinsic spin resonnances.

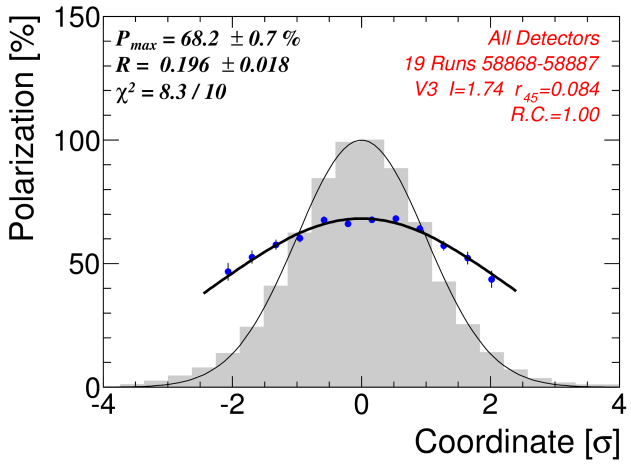

Figure 4.8 Measured horizontal polarization profile in the AGS at extraction energy in May 2013. The beam intensity profile is represented by a grey histogram and the polarization profile by blue dots. This measurement took 5 hours.

Injection in the AGS occurs at $G\gamma = 4.5$ and the vertical tune would need to be placed in the spin gap before the first vertical intrinsic resonance, around $G\gamma = 5$. Figure 4.9 shows the vertical tune crossing the spin tune around $G\gamma = 5$. Due to the strong optical distortions caused by the Siberian snakes, it is not possible to push the vertical tune high enough at low energy. We expect that the crossing of vertical intrinsic resonances in this region depolarizes part of the beam and induces a polarization profile in the vertical plane.

While the partial Siberian snakes configuration avoids depolarizations caused by imperfection and vertical intrinsic resonances, it also induces depolarization through horizontal intrinsic resonances when $Q_s = I \pm Q_x$ with Q_x the horizontal tune. The stable spin direction is not perfectly vertical with partial snakes (see Figure 2.13), therefore the non-zero horizontal component of the spin can resonate with the horizontal betatron tune. The strength of these resonances depends on

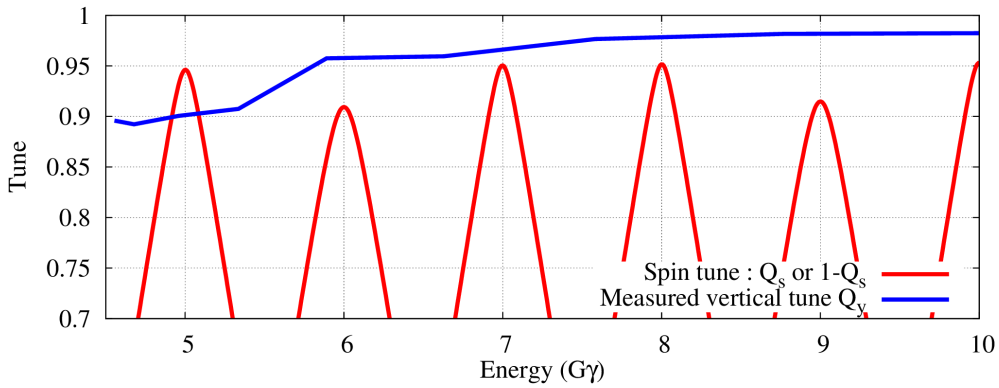

Figure 4.9 Fractional part of the vertical tune and spin tune at low energy as a function of the energy in the AGS.

the horizontal emittance and horizontal component of the spin vector, and crossing any of these resonances builds up a horizontal polarization profile. Other sources of depolarization can also contribute to the polarization profiles. For instance, linear betatron coupling or high order partial snake resonances [4] can increase the polarization profile. Depolarization due to high order partial snake resonances around $G\gamma = 45$ will be explored Section 5.2.2.3.

Post-processing softwares were developed to determine the polarization profile of the beam simulated from Zgoubi tracking data. The method can be described as follows:

- the tracking data is extracted at the required timings. This part is complex due to the size of the files containing the tracking data, easily reaching 10 GB for complete cycle tracking simulations with a few thousand particles. The particle data are generally saved at the end of the lattice as built in the Zgoubi AGS model, *i.e.* at the entrance magnetic edge of the A01 main magnet.

- the chromatic closed orbit is subtracted from each particle coordinates using the known $D_z(s)$ and $D'_z(s)$. The dispersion at the location of the recorded tracking data is used along with the momentum deviation from the reference momentum of each particle. This has the advantage of avoiding any possible longitudinal polarization profiles to appear in a transverse plane,

particularly on the horizontal plane.

- each particle is assigned to a bin according to its transverse position or phase if looking at the longitudinal plane. Since the profiles are always expected to be symmetrical, the binning is being done symmetrically, effectively only filling half of the bins and symmetrizing the bins afterwards. This allows mitigating adverse effects from the relatively small number of particles used in the Zgoubi tracking.

- in each bin the average polarization is determined using equation 4.7. The intensity profile is shown in Figure 4.10 with a grey histogram and the polarization profile by blue dots.

- both intensity and polarization profiles are fitted to Gaussian functions, then the R-value is calculated using equation D.3. Since the fit of the polarization profile is weighted by the beam intensity, the points far from the beam core weakly contribute to the profile and can be far from the fitted Gaussia(detailed in Appendix D)n. Figure 4.10 shows the Gaussian fits in black and the R-values are given using statistical error bars from the fitting.

This analysis aims at reproducing the measurement performed by the AGS polarimeter. However, some important differences need to be pointed out:

- the average polarization in each bin is computed using equation 4.7 while the AGS polarimeter effectively measures $< S_y >$ (Eq. D.2). This small difference only slightly changes the reported P_{max} value but does not change the computed R-value. Furthermore, it allows the computation of the R-value from tracking data when $\vec{n}_0.\vec{y} \sim 0$, *i.e.* around integer values of $G\gamma$.

- the longitudinal polarization profile cannot be seen in either transverse plane since the effect of the chromatic orbit is removed from each particle position before the analysis. The horizontal dispersion $D_x \sim 1.5\,\mathrm{m}$ at the AGS polarimeter means that a longitudinal polarization

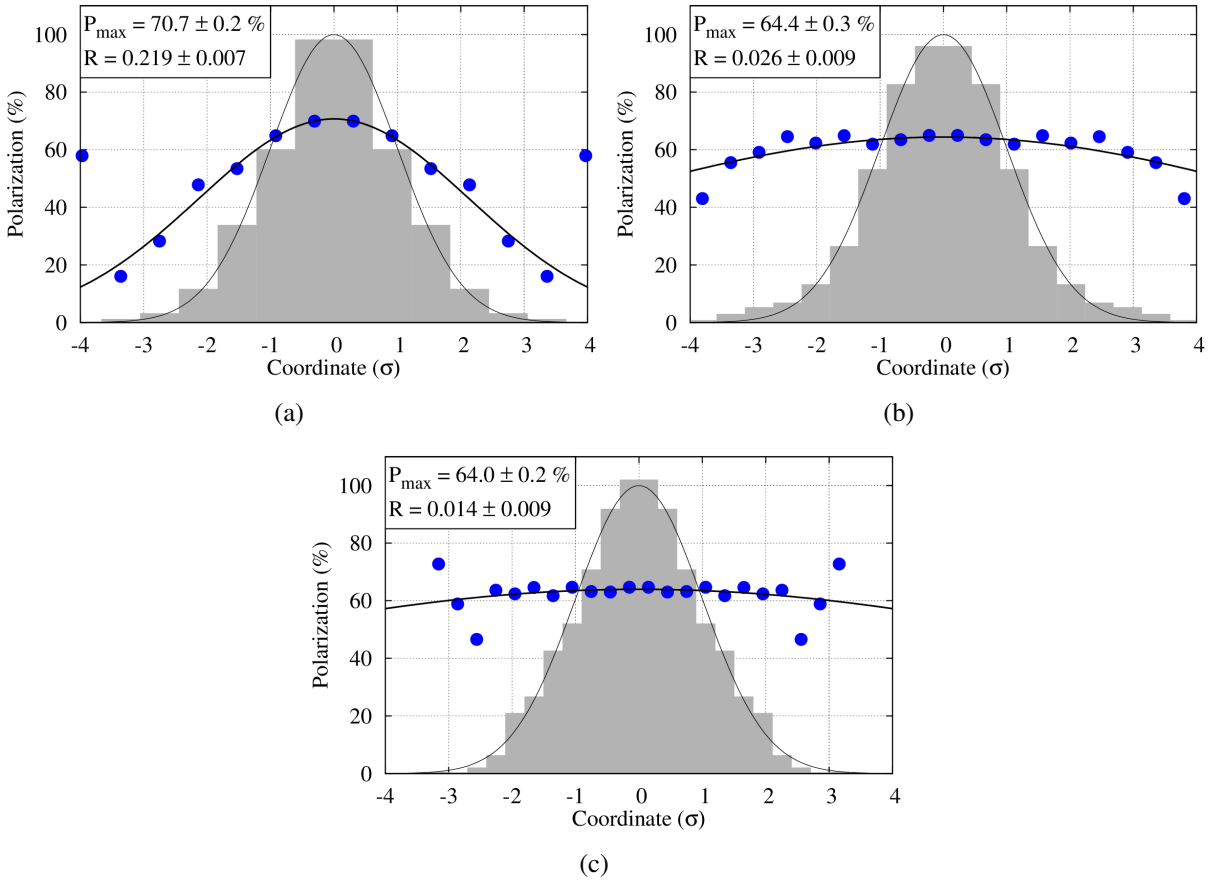

Figure 4.10 Polarization profiles at $G\gamma = 45.5$ from beam multiturn Zgoubi tracking in the AGS in the horizontal (a), vertical (b) and longitudinal (c) planes.

profile can show up in the measurement of the horizontal polarization profile. However, it is important for the simulated data to clearly observe the polarization profiles from each of the three planes independently.

- the simulated polarization profile is generally built from tracking data recorded at the A01 main magnet while the polarimeter is located at the C15 straight section. However the simulated polarization profile does not depend on the location since the effect of the dispersion is removed.

Taking advantage of the tracking data available along the AGS acceleration cycle, the evolution of the R value can easily be investigated. Figure 4.11 shows the evolution of the R value for the tracking simulation used to produce Figure 4.10. A detailed analysis will not be provided, but it is important to point out that the statistical uncertainty on the R value is much smaller than the variation observed by consecutive points in Figure 4.10. 4416 particles were tracked, but it seems that a non negligible uncertainty is introduced in the R value due to that limited number of particles being tracked. However, the number of particles seems to be sufficient to study the evolution of the polarization profile.

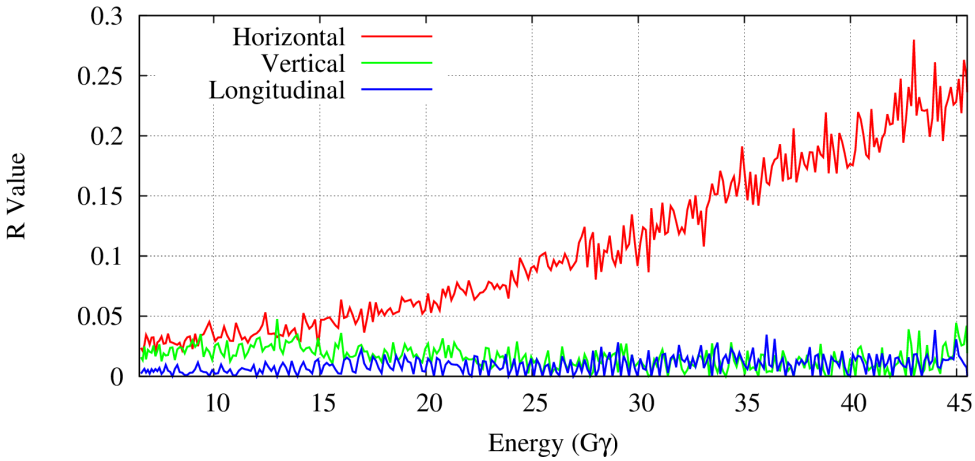

Figure 4.11 Evolution of the polarization profiles along a typical beam multiturn Zgoubi tracking started at $G\gamma = 6.5$.

4.2.2 Beam Emittance

Although polarization is our main interest here, beam dynamics needs to be carefully monitored. Tracking data recorded can be used to compute the evolution of the beam emittance along the simulation. As mentioned earlier, the main difficulty is to compute the beam emittance using particularly large files. The code *TunesFromFai*, part of the Zgoubi toolbox [78], was used to calculate the emittances. The transverse normalized 95 % emittance is estimated at regular intervals along the tracking using [25]:

$$\varepsilon_z^{N,95\%} = \beta\gamma\, 6\pi \sqrt{< z^2 >< z'^2 > - < zz' >^2} \tag{4.9}$$

For the longitudinal plane, the *TunesFromFai* code was modified to compute and store the first two moments of relative momentum dp/p and synchrotron phase ϕ distributions. The 95 % longitudinal emittance is then defined as

$$\varepsilon_l^{N,95\%} = 6\pi \frac{C}{h2\pi\beta c} \sigma(\phi)\, M_0 \gamma\beta^2 \sigma(dp/p) \tag{4.10}$$

with:

- h the harmonic RF number of the AGS, here $h = 8$.
- C the AGS circumference, $C = 807.091\,\text{m}$.
- $\sigma(\phi)$ and $\sigma(dp/p)$, respectively, the standard deviations of the RF phase and relative momentum of the beam.

4.2.3 Single Particle Tunes

Lattice tunes, associated to the tunes of the reference particle, are easy to compute and are only a function of the lattice. However, when large beams with momentum spread are tracked, it can be interesting to look at the evolution of the tunes of each particle within a beam. The code *TunesFromFai* was used to get the tune of each particle for dedicated multiturn simulations. The *TunesFromFai* code derives the DFT[1] of the transverse motion and the tune is assumed to be given by the index of the largest Fourier coefficient. This method requires the tracking data to be saved at every turn and dedicated simulations were done. Speed of beam multiturn simulations is limited by the recording of the tracking data at every turn. This analysis and the associated simulations were mainly used to study beam dynamics at low energy.

[1] Discrete Fourier Transform

4.3 Zgoubi Tracking in the AGS at Low Energy

The AGS uses a dual partial Siberian snakes configuration, but these specialized magnets can have adverse effects on beam dynamics. The strong twisted dipole field creates important longitudinal and non-linear fields along the particle trajectory [57, 58]. Since the snakes are driven at constant current, the effect on beam dynamics is stronger at low energy. Beam dynamics are notably complex below $G\gamma = 6-7$ due to:

- low beam rigidity that maximizes the effect of the snakes field.
- strong deformation of the AGS optics: betatron tunes are quickly changed as the rigidity increases, resulting in the crossing of multiple non-linear coupling betatron resonances below $G\gamma = 6$.

Figure 4.1 shows the evolution of the betatron tunes in the early part of the AGS pp acceleration cycle. The injection tunes are empirically optimized for intensity transmission from the AGS Booster. The vertical tune is increased as early as possible for spin dynamics purposes (as described in Section 2.4) and the location of the horizontal tune is optimized for intensity transmission [82]. Figure 4.12 shows the tune path in a tune diagram: the region where the tunes are quickly moved to increase the vertical tune is usually called the tune swing and one can see that multiple resonant lines of relatively low order are crossed in this region. The early part of the AGS acceleration cycle experiences intensity losses, and emittance growth is not excluded. The crossing of low order betatron resonances could degrade the beam quality by increasing the transverse emittance or through beam losses. Beam multiturn Zgoubi trackings were used to investigate the beam dynamics in this region.

The following simulations were done with a realistic lattice, as detailed earlier. Tracking was performed for 528 particles picked in a 6D Gaussian distribution, leading to initial transverse normalized 95% emittances of $8\,\pi$.mm.mrad. A longitudinal emittance of 1.46 eV.s and a realistic

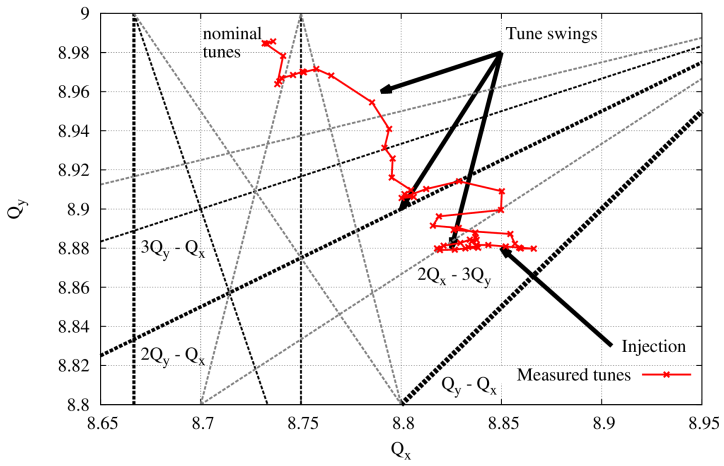

Figure 4.12 Tune diagram with measured tunes and important resonant lines.

acceleration rate were used. Tracking was done from $G\gamma = 4.55$ to $G\gamma = 21$ but we will focus on the region below $G\gamma = 10$.

Numerous beam multiturn simulations were done using the different models available for the snakes (see Section 3) [75]. Tracking using the latest snake maps are discussed here.

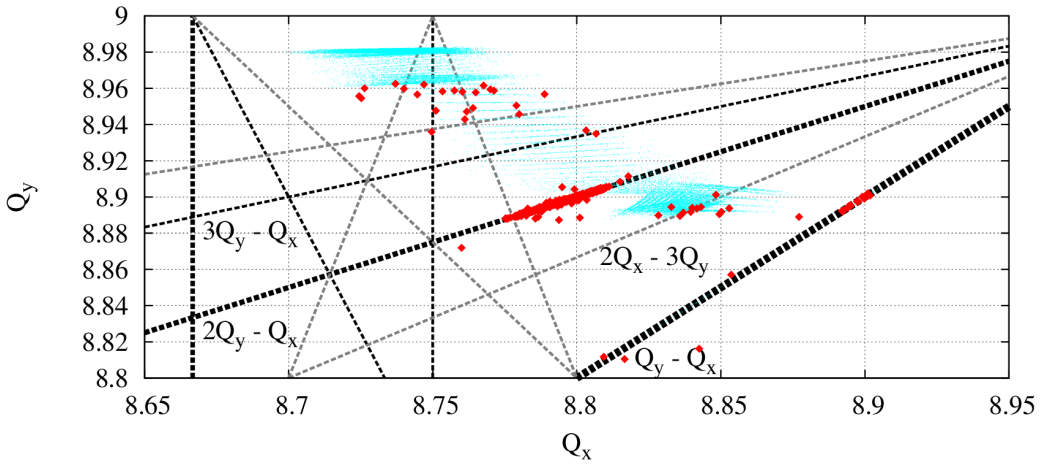

Figure 4.13 Tunes for tracking simulations for 528 particles in a tune diagram in cyan. If a particle is lost, its tune appears in red for its last 300 turns.

Figure 4.13 shows the evolution of the tune footprint for a beam multiturn tracking job from $G\gamma = 4.5$ to $G\gamma = 21$. Beam dynamics are especially complex during the tune swing, below $G\gamma = 6$.

Losses at that time appear to be associated with the $2Q_y - Q_x$ and $Q_y - Q_x$ resonant lines). However, beam dynamics in this region are not well understood yet, developments are carried on.

The evolution of the beam and its shape in this region makes the study of spin dynamics particularly hard. Nevertheless, other simulations associated with the study of vertical tune jumps during the AGS Run14 showed polarization profiles in agreement with measurements [83]. These simulations did not use the snakes magnets model discussed above but instead were using first order matrices to simulate the snakes.

It was therefore proposed to use the field maps of the Siberian snakes to simulate the AGS starting at $G\gamma = 6.5$, overcoming the complex tune swing region. To account for the depolarization experienced by the beam below $G\gamma = 6.5$, the initial spin distribution is extracted from the tracking data in the context of the vertical tune jump scheme. Due to the reproducibility of the pseudo random generator used for the initial particle distributions, the polarization profile can be copied from one tracking to the other.

This method is used in the simulations below to track realistic beam from $G\gamma = 6.5$ to $G\gamma = 45.5$.

4.4 Tracking Results and Experimental Measurements

4.4.0.1 Uncertainty and Number of Particles

The choice of using 4416 particles was driven by the uncertainty associated to the limited number of particles tracked. Table 4.1 shows the spread of the data at the end of a typical tracking job, from $G\gamma = 6.5$ to $G\gamma = 45.5$. The same simulation was repeated four times with four different initial beam distributions generated by changing the seed used by the random generator. For three different numbers of particles the final average polarization and the horizontal polarization profile were determined. The standard deviation used here is defined for n simulations by:

$$\sigma_n = \sqrt{\frac{1}{n-1}\left[\left[\sum X^2\right] - \left[\sum X\right]^2\right]} \tag{4.11}$$

with $n = 4$ here and X the quantity of interest in Table 4.1. It appears that 2000 particles seems to

Table 4.1 Summary of the effect of the sample size on the mean polarization and horizontal R-value.

Number of particles	1000	2000	4416	17664
Mean Polarization(%)	84.16	81.65	81.31	81.31
Standard deviation	5.2	0.5	0.15	-
Mean horizontal R value	0.189	0.192	0.194	-
Standard deviation	0.012	0.014	0.007	-

be enough to study the final average polarization but the standard deviation on the horizontal profile remains large. Using 4416 particles gives a small enough spread for the computed horizontal R value. The number of particles needs to be kept as small as possible to use the allocated computing resources as efficiently as possible: for instance, the simulations discussed here (4416 particles over 130,000 turns using Zgoubi) require around 12,000 CPU hours[1] each. Therefore it is not

[1]Unit commonly used to quantify computer resources consumption and defined as the use of a single core CPU during one hour.

possible to track tens of thousands of particles if one wants to investigate the effects of some parameters such as the beam size or the tune jumps timings, which requires numerous simulations to understand the effect of each parameter on the final beam polarization. Taking into account the yearly allocations of computer resources from NERSC, in the order of one to two million CPU hours, it is best to keep the number of particles as low as possible.

4.4.1 General Tracking Results and Machine Measurements

The simulations consist of a tracking job with 4416 particles initially picked in a 6D Gaussian distribution leading to transverse emittances of $14\,\pi$.mm.mrad in the vertical and horizontal planes. The initial longitudinal emittance is taken at 1.46 eV.s, and the distributions are cut at $\pm 3\sigma$ in all 6 dimensions. These are typical beam sizes measured at the AGS extraction [5].

4.4.1.1 Transverse Beam Dynamics

Figure 4.14 shows non-negligible variations of the estimated beam emittance along the tracking. It is important to note that the spikes observed are not realistic, the increased excursion of one or more particles leads to an overestimation of the beam emittance before the particle is lost. In particular, the transverse emittances seem to slowly vary between $G\gamma = 15$ and the end of the tracking. One would expect this quantity to remain constant according to Equation 2.39. However, the estimation of the beam emittance (see Section 4.2.2) can be influenced by changes in the beam distribution: while the initial distribution is closely Gaussian, it can be altered during the tracking. Figure 4.15 shows the beam projections at the start and at the end of the tracking. It can clearly be seen on Figures 4.15(b) and 4.15(d) that the profiles are not Gaussian anymore at the end of the tracking. Beam dynamics below $G\gamma = 15$ are particularly dependent on the strong optical effects of the snakes and the large motion of the tunes (Figure 4.1), which could explain the variations of the emittance.

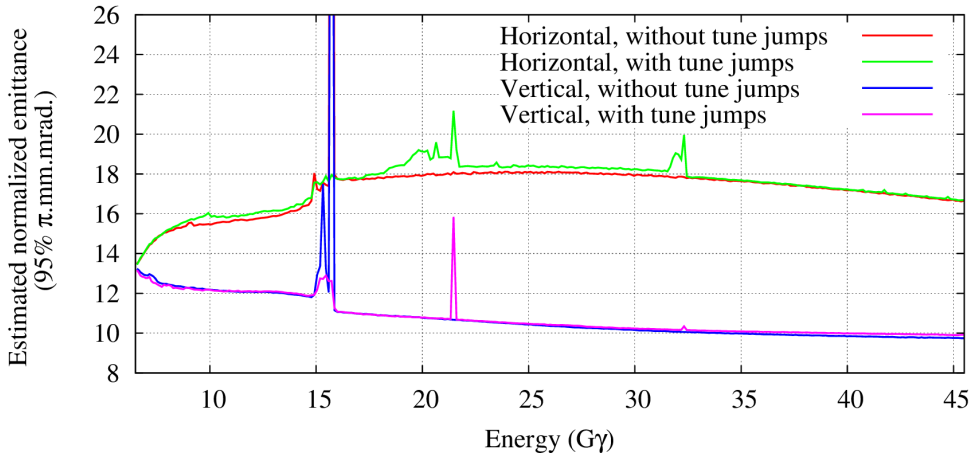

Figure 4.14 Estimated transverse emittance from Zgoubi multiparticle tracking for realistic conditions, as a function of the beam energy.

Figure 4.16 shows the effect of the integration step size used for tracking inside the AGS main magnets by the Zgoubi code on the horizontal emittance. The same behavior is seen in the vertical plane. Lower integration step size leads to better behavior of the beam dynamics since the invariant represented in Figure 4.16 should remain constant. However, the computation time is inversely proportional to the integration step used in the Zgoubi code. Therefore the choice for the integration step size is a compromise between the conservation of the emittance and the tracking speed. Figure 4.16 shows a drop of around 10 % in horizontal emittance for an integration step in the main magnets of 3 cm over 80,000 turns of tracking. Considering the large amount of CPU power needed for beam multiturn Zgoubi tracking, an integration step of 3 cm in the main magnets is a good compromise. Dedicated simulations with smaller integration step size can be considered for specific studies, but are not discussed here.

Due to this choice of integration step size, Figure 4.14 should be interpreted carefully. It can clearly be seen though that the tune jumps do not modify the evolution of the transverse emittance. This particular issue will not be discussed here but it is especially relevant since significant emittance growth due to the tune jumps has been observed, and solved, in the past [79].

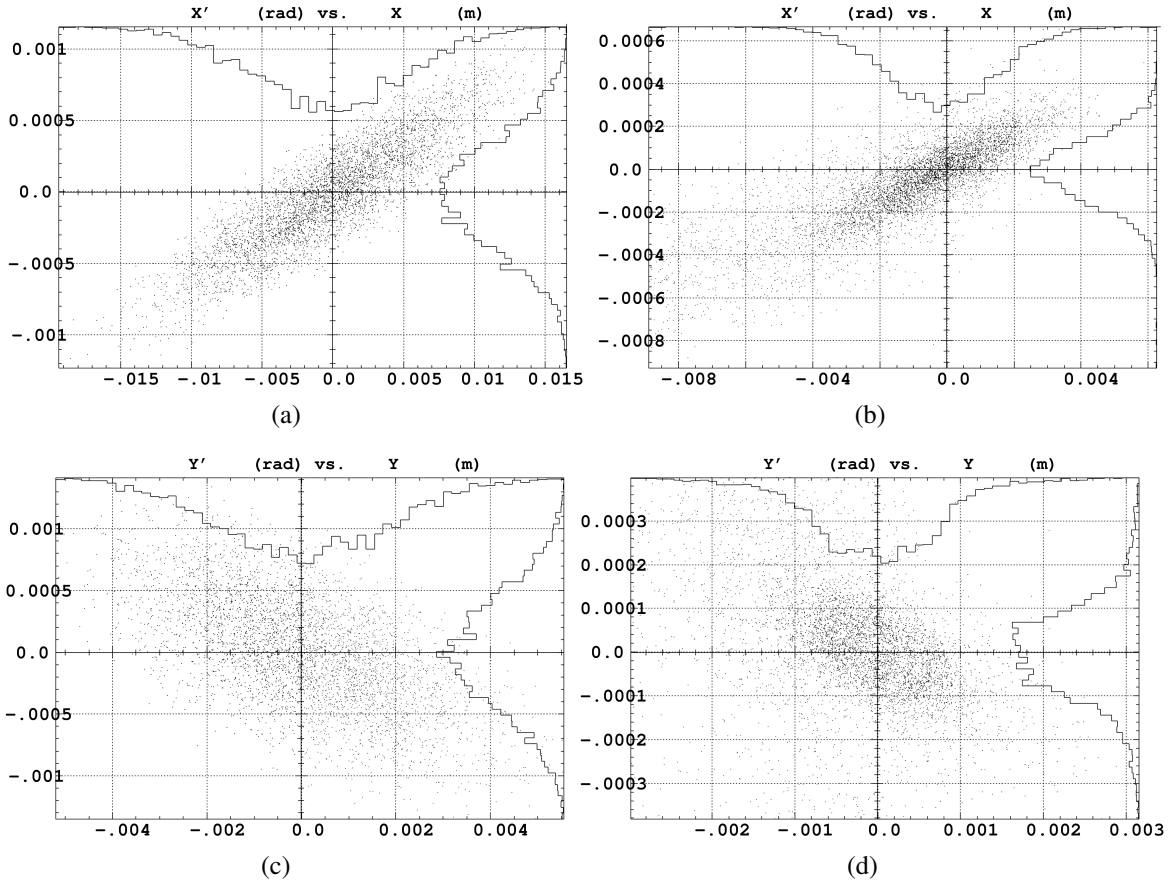

Figure 4.15 Projection of the beam distribution at the start (a)(c) and at the end (b)(d) of the multiparticle tracking, using the Zpop Zgoubi post processing tool.

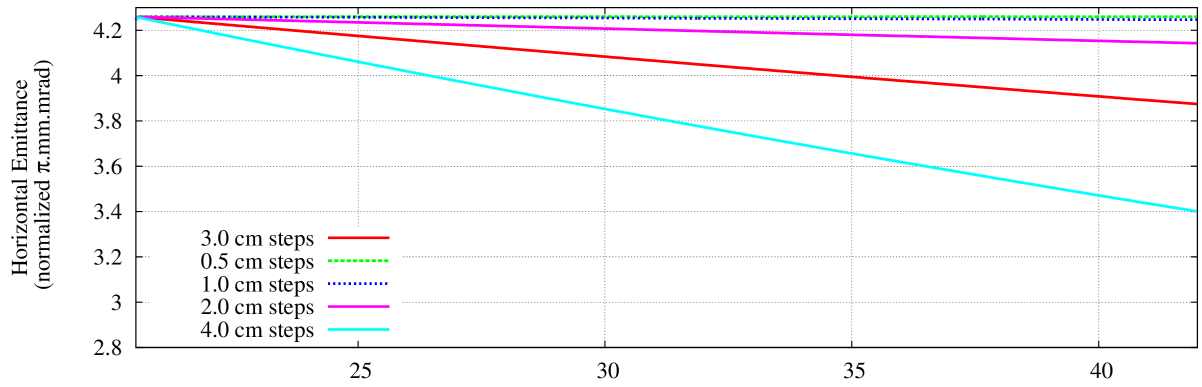

Figure 4.16 Evolution of the single particle horizontal normalized emittance for a 80,000 turns tracking using the AGS bare model.

4.4.1.2 Longitudinal Beam Dynamics

Looking at the longitudinal plane, Figure 4.17(a) shows a large drop in the estimated longitudinal emittance. This behavior is associated to losses around $G\gamma = 15$, during the powering of the gamma transition quads. Figure 4.17(b) shows an increase in the average relative momentum of the beam associated to particle losses. Particles below the reference momentum were preferentially lost, causing the average beam momentum to shift above zero. These losses are not observed in the machine but the transition region is known to be very sensitive and requires frequent tuning to achieve the low level of losses typically experienced during operations [82]. Although non realistic, these losses cannot be avoided without introducing realistic orbit in the model; Figure 4.17(b) still shows that dipole oscillations of the beam remain small compared to the beam extension in momentum, as shown by the 2σ envelope.

Studies on the effect of the longitudinal emittance should, therefore, be interpreted carefully. However, most of the beam remains unchanged from losses at transition, so the final quantities simulated should still be realistic. Additionally, further simulations (not shown here) demonstrated that the longitudinal emittance does not strongly influence the final beam polarization; simulations as described in this section can therefore be compared to machine measurements even if the lon-

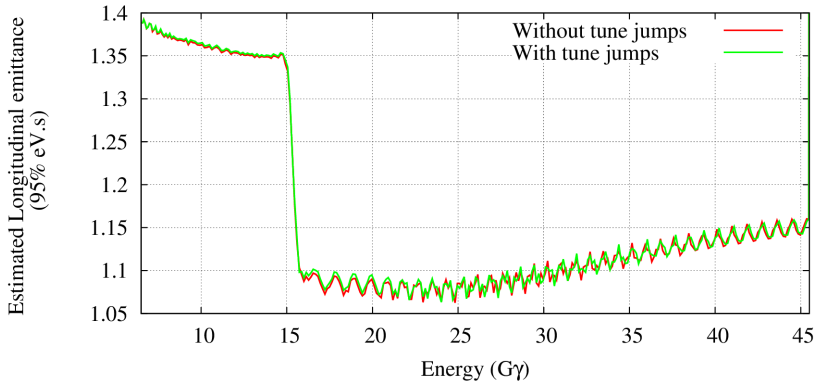

(a)

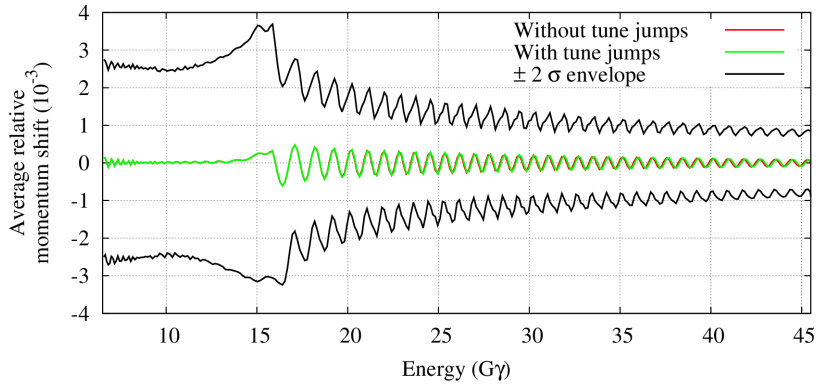

(b)

Figure 4.17 Estimated longitudinal emittance (a) and average beam relative momentum (b) from Zgoubi multiparticle tracking for realistic conditions as a function of the beam energy.

gitudinal emittance being used is somewhat smaller than the actual one after transition. However it is important to note that longitudinal emittance reduces the efficiency of the tune jumps system, hence the polarization gain from the tune jumps [84].

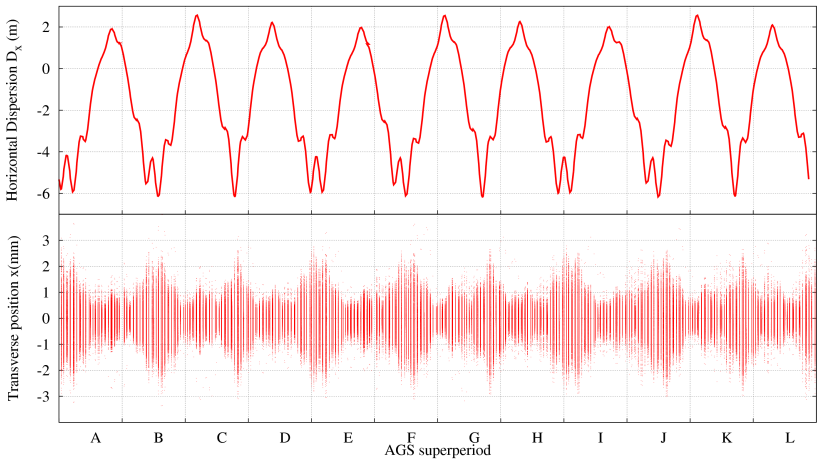

Figure 4.18 Horizontal dispersion and transverse beam position during tracking, at $G\gamma = 15.7$.

Figure 4.18 presents the dispersion function and the horizontal beam projection along the AGS lattice, just before the transition jump. The large deformation in dispersion is caused by the gamma transition quadrupoles and induces the beam losses observed during multiturn tracking. Further work to implement realistic orbits in Zgoubi should allow for a better control of these losses.

4.4.1.3 Spin Dynamics

Figure 4.19 shows the evolution of the polarization profiles along the tracking. The horizontal polarization profile grows regularly along the tracking, although the later part of the tracking seems to contribute more to the final profile. The use of the tune jumps considerably reduces the horizontal polarization profile at $G\gamma = 45.5$ and it can be seen in Figure 4.19 that the effect is also built-up along the tracking.

The vertical polarization profile, however, does not seem to vary along the tracking. The verti-

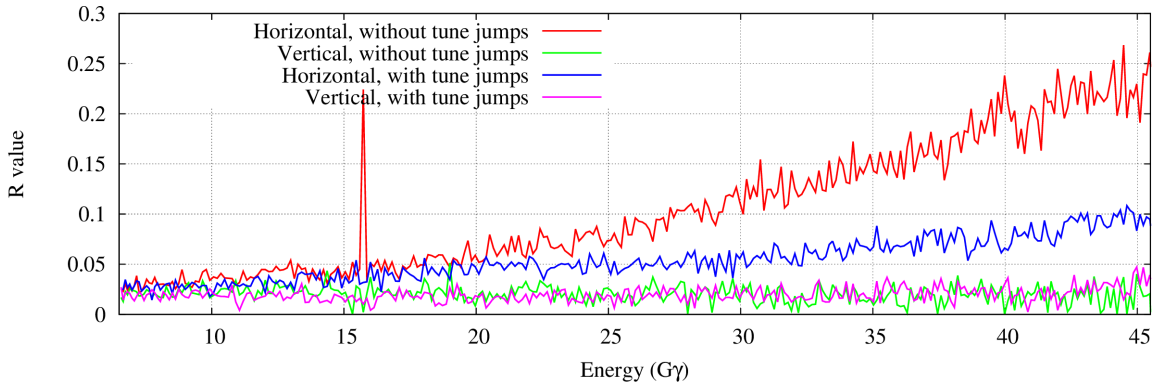

Figure 4.19 Polarization profiles from $G\gamma = 6.5$ simulated by the Zgoubi code, with typical beam and machine conditions.

cal tune being kept within the spin tune gap, it is expected that polarization losses through vertical intrinsic spin resonances are avoided, hence the vertical polarization profile remains constant. The initial polarization profile at $G\gamma = 6.5$ in the vertical plane seems to be conserved along the tracking.

The most recent measurements of polarization profiles are presented in Table 4.2, for typical beam and machine conditions. Measured and simulated horizontal polarization profiles without tune jumps are very close, giving a strong confidence in the spin dynamics simulated by the Zgoubi code. With tune jumps the simulated horizontal polarization profile is also very close to the measurement, which validates the model of the tune jumps but also confirms that the experimental timing of the tune jumps is accurate.

Measured vertical polarization profiles are much larger than the simulations. The value of the simulated vertical polarization profile is expected since no vertical intrinsic resonance is crossed. However measurements consistently show strong vertical polarization profiles. The tune jumps also seem to reduce the measured vertical polarization profile, which is rather unexpected and so far remains unexplained.

The simulated spin dynamics using the Zgoubi code is qualitatively conform to the expectations. Measured values of horizontal polarization profiles are successfully predicted by the Zgoubi

Table 4.2 Comparison of simulated polarization profiles from Figure 4.19 with measurements from the AGS ppRun 14 for typical beam and machine conditions [5]. Uncertainties on the simulated polarization profiles are estimated from Table 4.1.

Measured [5]		Simulated		Machine conditions
R_x	R_y	R_x	R_y	
0.206 ± 0.020	0.181 ± 0.033	0.250 ± 0.007	0.021 ± 0.007	Without tune jumps
0.127 ± 0.019	0.124 ± 0.026	0.100 ± 0.007	0.035 ± 0.007	With tune jumps

code with and without tune jumps. As for the vertical plane, the simulated polarization profile evolution is understood, but discrepancies with measurements drove strong interest in a better understanding of the evolution of polarization profiles along the AGS acceleration cycles. Numerous explanations for the large measured vertical polarization profiles have been advanced so far, such as the transverse coupling or higher order snake resonances. New polarization profile measurements at intermediate energies between $G\gamma = 4.5$ and $G\gamma = 45.5$ are scheduled for the pp-Run 15. These should help understanding the discrepancies observed with the Zgoubi simulations and the mechanisms leading to it.

4.4.2 Example of Parameter Study: Horizontal Emittance and Polarization Profiles

Simulations presented above are especially interesting when trying to quantify the effect of machine or beam parameters on the final polarization and its profiles. It was shown earlier that Zgoubi simulations correctly predict the horizontal polarization profile at $G\gamma = 45.5$. Using the Zgoubi code gives the opportunity to quickly estimate the effect on the final polarization profile of *e.g.*, the initial horizontal beam emittance. A similar measurement during machine operations, while possible, would be particularly complex and slow due to the limited control on the beam emittance and time required for a single polarization profile measured at $G\gamma = 45.5$, which would be at least

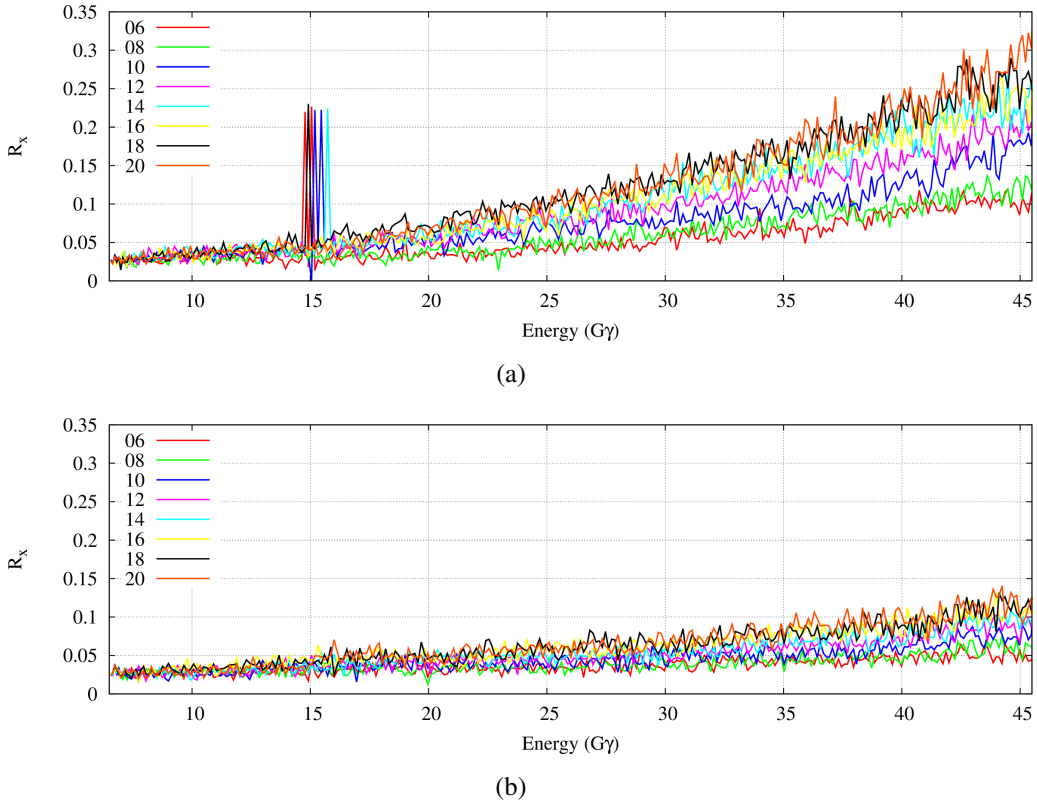

Figure 4.20 Simulated horizontal polarization profile as a function of the energy for different initial beam horizontal emittances (in 95% $\pi mm.mrad$ normalized and at $G\gamma = 6.5$) without (a) and with tune jumps (b).

5 hours.

Figure 4.20 shows the effect of the horizontal beam size at the start of the tracking on the evolution of the horizontal polarization profile R_x. Although it is known that the horizontal polarization profile increases with the horizontal emittance, this simulation gives a quantitative evaluation of this effect. Beam multiturn tracking correctly predicted the horizontal polarization profile in nominal conditions (Table 4.2), therefore the results from Figure 4.20 can be used to predict the effect of, for instance, an increase in injected beam intensity, which is known to change the beam emittance in the machine.

Several other beam and machine parameters can be, and were, explored using beam multiturn

Zgoubi tracking. Section 5.2.1 reviews the effect of errors in the tune jump timing on the final polarization using systematic simulations.

Chapter 5

Simulations and Direct Application to Experimental Work

The Zgoubi model of the AGS, as well as the procedure and general results related to beam multiturn tracking in the AGS, were detailed in Chapter 3 and 4. Now we will focus on a few direct applications of the simulations using the Zgoubi code in the AGS. We will see that these simulations in the AGS are very important to understand the depolarization through the horizontal intrinsic spin resonances. Then the importance of the tune jumps timing will be explored and an original scheme for the tune jumps at low energy will be developed.

5.1 Depolarization through Horizontal Intrinsic Resonances

We have seen in Section 4 that the crossing of horizontal intrinsic resonances causes most of the explained polarization losses. At the start of beam multiturn simulations of the AGS using the Zgoubi code, in 2012, one of the first simulations done was limited to the end of the cycle. The goal was to study the effect of the tune jumps on the polarization at the end of the ramp, and to better understand the depolarization in this region.

5.1.1 Flat Top Roll Over and Depolarization

At that time the AGS acceleration cycle was slowly decreasing at the end of the ramp to smoothly reach the extraction energy. Figure 5.1 shows the measured acceleration rate compared to a constant and maximum acceleration rate up-to extraction energy. The later scheme involved an extraction of the beam during the ramp, hence named extraction-on-the-fly. Also, it is known that the

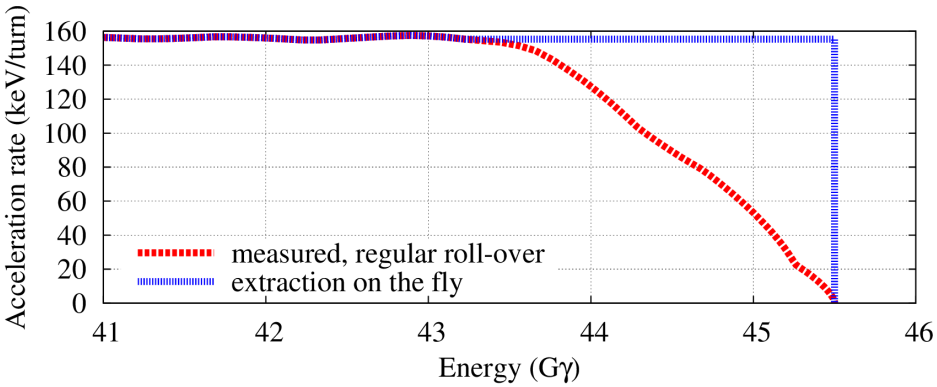

Figure 5.1 Acceleration rate in the AGS at the end of the ramp, as a function of the energy.

depolarization through an intrinsic spin resonance is linked to the acceleration rate (Eq. 2.102). Therefore, Figure 5.1 shows that a number of horizontal intrinsic resonances were crossed at a low speed compared to the rest of the ramp. In particular, the last horizontal intrinsic spin resonance at $G\gamma = 45.3$ was very slowly crossed, possibly leading to large polarization losses. Zgoubi was used to simulate the expected polarization gain in the case of the extraction-on-the-fly. Simulations were required to quantify the polarization gain since the investment needed to implement an extraction-on-the-fly scheme would have been considerable. Figure 5.2 shows the results from a beam multiturn tracking of 2000 particles from $G\gamma = 19.5$ launched on the $\vec{n}_0$ vector, with typical beam and machine conditions. The absolute polarization is not relevant since the simulation was started with full polarization. However, one can determine the relative gain from the extraction-on-the-fly. Without the tune jumps the relative increase would be 6.8%. Despite the high crossing rate provided by the tune jumps, a relative gain of 2.4% can be seen in the case with tune jumps.

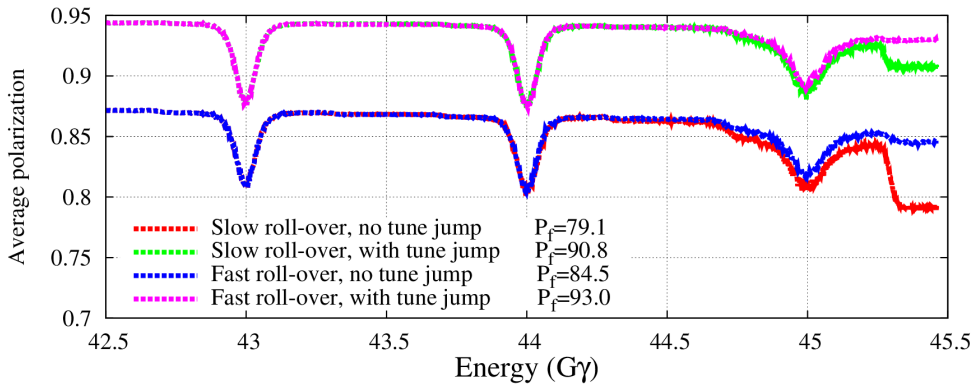

Figure 5.2 Simulated average beam polarization as a function of the energy in the AGS, at the end of the acceleration cycle.

Expectation of higher polarization drove a strong interest for the extraction-on-the-fly scenario but a simpler solution was found. A new power supply function for the AGS main magnets was set up to provide a quick transition between the ramp and the flat-top. This new function allows the AGS to ramp at the full acceleration rate up to the extraction energy. Thus, the last horizontal intrinsic resonance is also crossed at the maximum acceleration rate. Comparisons were then possible between the simulation involving extraction-on-the-fly and measurements carried out in the AGS using the fast roll-over.

Polarization measurements were taken with both magnet functions, with or without tune jumps. Table 5.1 summarizes the measurements taken using a vertical fixed target polarization measurement. The experiment was carried with $1.2.10^{11}$ particles per bunch and typical beam emittances. With the tune jumps active the effect of the fast roll-over is expected to be smaller since the crossing rate of the horizontal intrinsic resonances is dominated by the tune jumps. Nevertheless, the simulations show a relative gain of 2.4%. We can see in Figure 5.2 that the polarization gain occurs across the last horizontal intrinsic resonance, at $G\gamma = 45.3$, where the acceleration rate is very small. The discrepancy between the simulated and measured gains is not completely understood but the probable causes are:

- The fast roll-over imposes a fast modification of the 9^{th} vertical harmonic orbit across $G\gamma =$

Table 5.1 Summary of the polarization measurements taken in March 2012 with both main magnet functions and the associated simulation results.

machine state	measured polarization	measured gain	simulated gain
tune jumps OFF			
slow roll over	62.8 ± 1.1 %		
fast roll over	67.3 ± 1.1 %	+7.2%	+6.8%
tune jumps ON			
slow roll over	70.1 ± 1.1 %		
fast roll over	70.5 ± 1.1 %	+0.6%	+2.4%

45 to avoid the depolarization due to the imperfection resonance. This is harder with the two closest tune jumps at $G\gamma = 44.7$ and $G\gamma = 45.3$, separated by 5 ms [47].

- The uncertainty on the measurement leads to an uncertainty in the measured gain of 3.3%. Therefore the measured gain can be considered in agreement with the simulations if the uncertainty of the measurement is propagated to the gain.

Polarization measurements did not show measurable gain from the fast roll-over with the tune jumps, more measurements are required to reduce the uncertainties. Nevertheless, a clear gain has been measured without tune jumps, giving strong confidence in the Zgoubi model for this application. The fast roll-over is used for operations since March 2013.

This application of the Zgoubi beam multiturn tracking perfectly illustrates the necessity of these simulations to investigate depolarization sources and develop new schemes. The investment, in terms of man power, budget, and beam study time, required to improve polarization transmission in the AGS makes realistic simulations absolutely necessary.

5.2 Tune Jump Timing and Energy Measurement in the AGS

The tune jumps system and its interest has been discussed in Section 2.4 and Chapter 4. Here we will use Zgoubi beam multiturn simulations to show how critical the timing of the tune jumps is to the efficiency of the system. We will then detail experiments to improve the tune jumps timing that were setup using the Zgoubi code.

5.2.1 Tune Jumps Timing Shift

Measuring the efficiency of the tune jumps system is particularly complex, especially if one wants to estimate the accuracy of the tune jumps timings. The only measurement meant to give an idea about the accuracy of the tune jumps timing consists of polarization measurements with shifted tune jumps timing. The expected final polarization as a function of the tune jumps timing shift follows the shape of the beam in the longitudinal plane. The figure eventually widens or shifts in case of errors in the tune jumps timing [79].

Figure 5.3(a) shows such a measurement taken in 2013. A Gaussian function seems to fit the data well, with an estimated standard deviation in agreement with the theoretical expectations detailed in [79]. The shift Δt measured is not expected and will not be discussed here, but a lot of work has been done to improve the tune jumps timing since May 2012 [84, 85]. Figure 5.3(b) shows the simulated polarization using Zgoubi beam multiturn trackings. The beam and machine conditions used for these simulations were detailed in Chapter 4. The error bar visible on the simulated average polarization was introduced in Table 4.1. In this case the estimated shift is compatible with zero, which is expected since the simulations allow for perfectly timed tune jumps.

Measurement and simulations are in good agreement, giving a strong confidence in the model. The important is the estimated standard deviation, which is around $200\,\mu$s. This parameter is

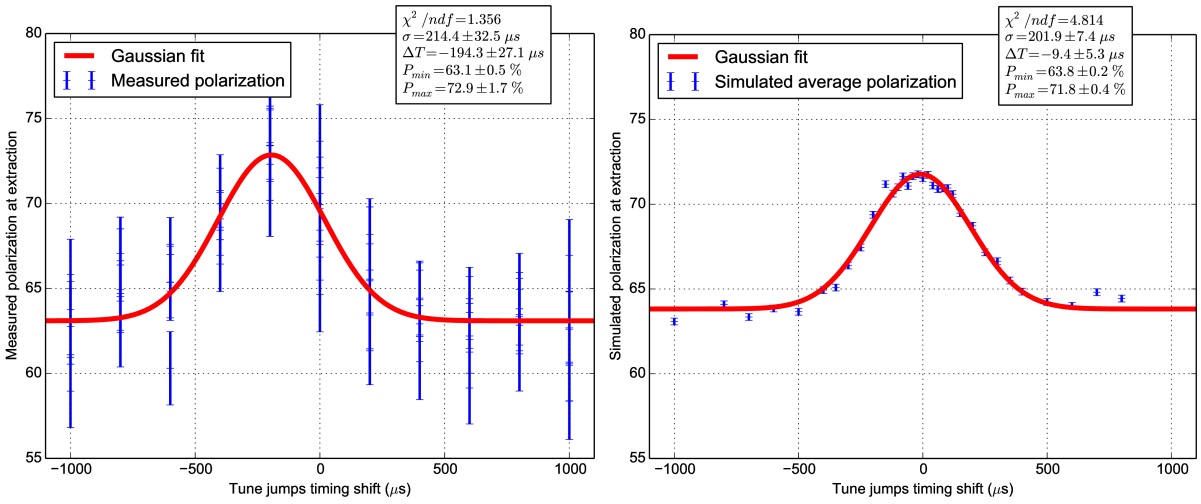

(a) (b)

Figure 5.3 Polarization at $G\gamma = 45.5$ as a function of a global shift of the tune jumps timing measured during the AGS Run13 (a) and simulated using beam multiturn Zgoubi tracking (b).

expected to increase if random errors in the timing of the tune jumps are introduced. This gives an upper limit of $\pm 100\,\mu$s in the acceptable error of the timing of the tune jumps to maintain a good efficiency of the system.

5.2.2 Energy Measurement Methods

We have seen that the tune jumps timings are critical for polarization transmission in the AGS. We will now see how the Zgoubi code helped identify and correct an error detected in the tune jumps timing during the AGS Run13.

While the spin tune Q_s is a function of the energy, tune and energy measurements along the ramp allow precise timing of each jump. During the polarized proton operations, these measurements are regularly used to generate new timings for the tune jumps. This is supposed to compensate for any drift in the timing of the resonant condition, for instance due to a drift of the tune over time. During the AGS Polarized Proton Run 13, these measurements were regularly conducted

to provide the highest polarization to the RHIC. In late April 2013, after a few weeks of running

Table 5.2 Polarization measurements during Run 13.

Measurement date	Tune jumps timing	Polarization
May 5th	from April 6th	$66.0 \pm 0.9\,\%$
May 5th	from April 29th	$59.7 \pm 1.1\,\%$
May 5th	from May 5th	$62.8 \pm 1.1\,\%$
June 6th	Uncalibrated	$64.4 \pm 3.9\,\%$
June 6th	After calibration	$70.9 \pm 1.6\,\%$

with the same tune jumps timings, new timings were generated but the polarization decreased unexpectedly. Table 5.2 shows that on May 5th the measured polarization was higher for the older timings.

To explain this deterioration, the entire process from the computation of the tune jumps timing to the trigger of the pulsed power supply was verified, without finding any error. We decided to investigate on the measurements used to compute the jump timings: tune and energy measurements. The tune measurement is based on the free oscillation of the beam. It is therefore an absolute measurement and is unlikely a source of significant error. The energy measurement is more complex and needs to be calibrated, making it a possible suspect for our problems.

5.2.2.1 Conventional Energy Measurement in the AGS

The AGS uses a dedicated device called the *GgammaMeter* to measure the energy along the ramp. The energy is determined using the measured RF frequency f and average radius of the beam dR (Eq. 5.1), or the measured field $(B_{\text{inj}} + B_{\text{clock}}/C_{\text{scal}})$ and average radius (Eq. 5.2):

$$G\gamma = G\frac{1}{\sqrt{1-\frac{1}{c^2}\left(\frac{f}{h}\right)^2(2\pi)^2(R_0+dR)^2}} \tag{5.1}$$

$$G\gamma = G\sqrt{\left[\frac{\left(1+\gamma_{tr}^2 dR/R_0\right)\rho_0 c\left(B_{\text{inj}}+B_{\text{clock}}/C_{\text{scal}}\right)}{m_0}\right]^2+1} \tag{5.2}$$

with γ_{tr} the *gamma*, R_0 the radius of the AGS, m_0 the proton rest mass and ρ_0 the radius of curvature in the main magnets. The parameters in red (f, dR and B_{clock}) are measured quantities, while the blue ones are machine parameters (R_0, γ_{tr}^2, ρ_0, B_{inj} and C_{scal}) that can be adjusted, and the black are fixed physical constants.

The *GgammaMeter* is cross calibrated: at low energy the machine parameters in equations 5.2 and 5.1 are adjusted manually until the two methods report the same energy along the ramp. However, at high energy the measurement based on the RF frequency (Eq. 5.1) is too sensitive, due to the highly relativistic beam.

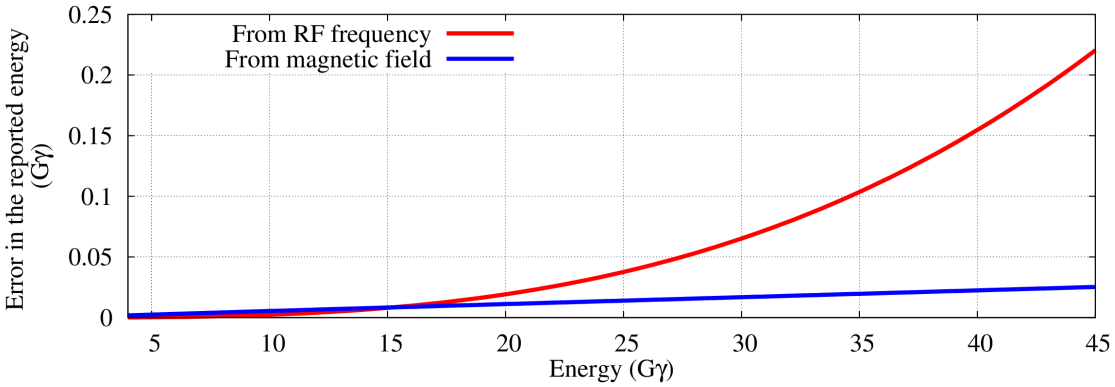

Figure 5.4 Error on the reported energy caused by an error of 1 mm in the measured average beam radius.

Figure 5.4 shows the derivative of equations 5.2 and 5.1 with respect to the measured average radius: $\partial G\gamma/\partial(dR)$. As the energy increases, we can see that the sensitivity of the energy measurement based on the revolution frequency becomes very large. While we consider that the

measured average radius is known within a fraction of millimeter we also need an accuracy of around $0.01\,G\gamma$. It is visible that the conventional method of cross calibration is very hard at high energy.

5.2.2.2 Fitting Assisted Energy Calibration

In order to reach and maintain the accuracy of the AGS energy measurement system, frequent calibrations are performed during polarized proton operations. The procedure consists of minimizing the difference between the energy computed by equations 5.1 and 5.2 along the acceleration ramp (shown in pink in Figure 5.5(b)). However, the manual modification of the adjustable parameters to calibrate the *GgammaMeter* is particularly complex and requires an expert of the system.

It was proposed to develop an application capable to automatically calibrate the *GgammaMeter* parameters using fitting procedures. Figure 5.5 shows the graphical interface of the application, developed in collaboration with the RHIC Control System group. The application provides a convenient interface to load and present data averaged over multiple consecutive cycles of the AGS. The mean is used to determine the statistical accuracy associated with each of the measured parameters. The correct transport of the uncertainties from the measured parameters allowed to compute and plot the resulting uncertainties in the differences between the two methods of energy computation (showed in grey in Figure 5.5(b)).

The automatic fitting of the machine parameters, shown Figure 5.5(b), allows the application to be used by non experts of the system. This effectively grants the ability for the calibration to be carried out by operation, and on a regular basis during polarized proton operations.

However, Figure (b) clearly shows large uncertainties at high energy, considerably limiting the calibration method in the later part of the acceleration cycle. This raises a strong interest to develop an independent method on energy measurement, possibly to calibrate the *GgammaMeter*. Since the AGS accelerates polarized protons, approaches based on the depolarization of the beam can be

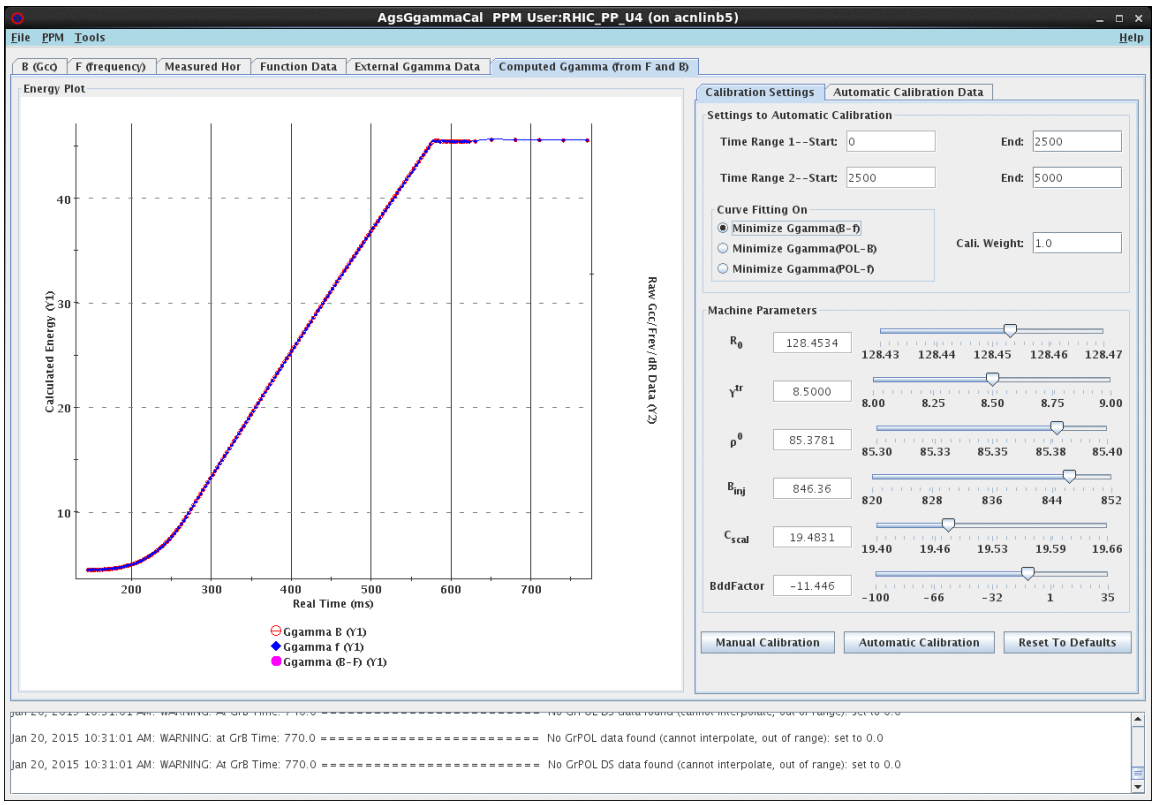

(a)

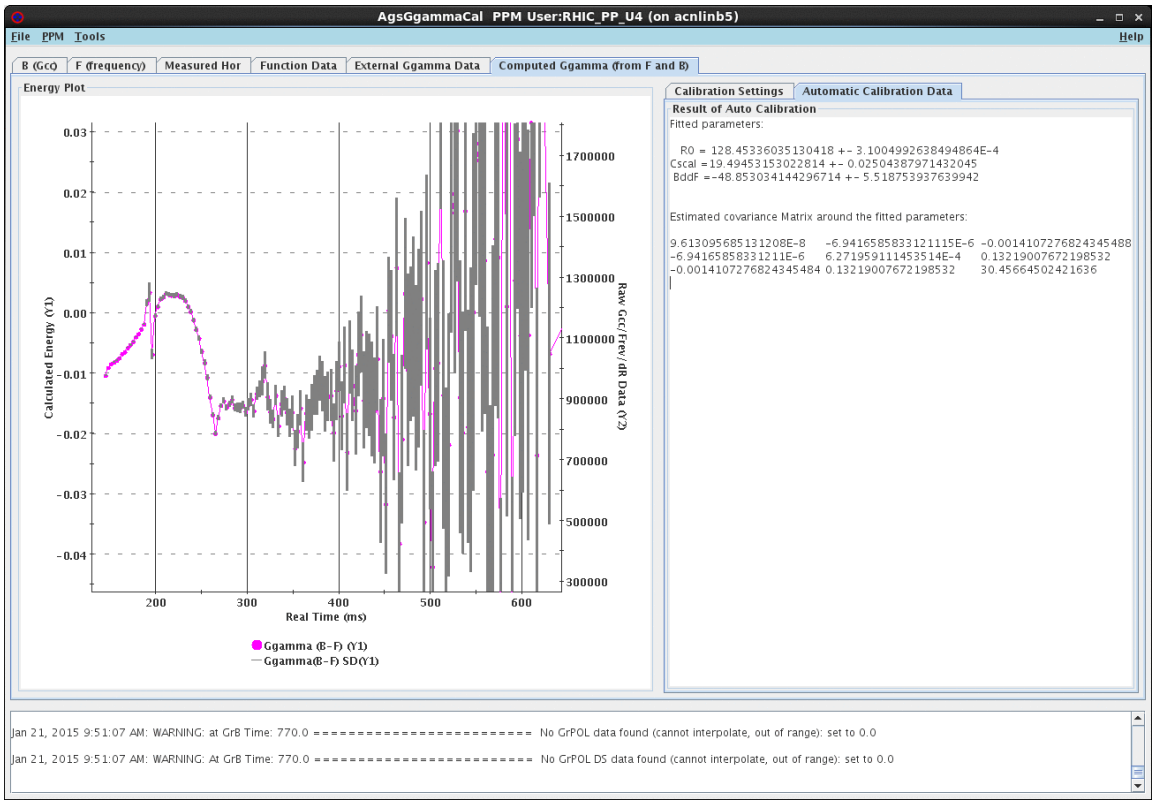

(b)

Figure 5.5 Screenshot of the *AgsGgammaCal* application showing the energy as a function of the AGS time and the manual calibration tab (a), and the difference between the two methods of energy computation and the auto calibration tab (b)

explored. A promising method using the current hardware of the AGS takes advantage of the tune jump system to accurately locate a strong vertical intrinsic resonance.

5.2.2.3 Tune Jumps Based Energy Measurement

While the tune jump system is used for its effect on the horizontal tune, it also induces a tune shift of $\Delta Q_y \sim -0.02$ in the vertical plane, within $100\,\mu$s. In addition, the partial snake configuration of the AGS modifies the spin tune, opening a forbidden band or "spin gap" in which the vertical tune is placed to avoid the vertical intrinsic resonances $Q_s \pm Q_y = n$. It is then possible to use a single tune jump to lower the vertical tune below the maximum value of the spin tune $Q_s^{\max}$, leading to a depolarization of the beam.

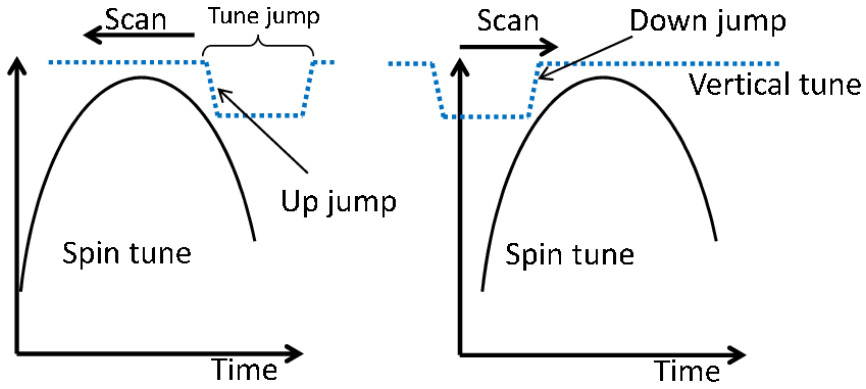

Figure 5.6 Illustration of the method used to locate the vertical intrinsic resonance.

Figure 5.6 shows the principle of the measurement. First the vertical tune is lowered to just above $Q_s^{\max}$, such that the tune jump is able to lower the vertical tune out of the spin gap. Then the timing of the tune jump is scanned across the spin resonance and the polarization at the end of the ramp is measured for each timing of the tune jump. If the spin tune crosses the vertical tune, a lower polarization is measured due to the depolarization across the resonance. The up-jump determines the location of the right side of the resonance and the down-jump allows to locate the left side.

The single crossing of the resonance, at the regular acceleration rate, has to strongly depolarize the beam in order for the difference in polarization to be clearly measured. Therefore, the measurement is only carried at the two very strong vertical intrinsic resonances: 0+ and 36+.

While the method shown in Figure 5.6 is very simple, several factors complicate the expected behavior:

- the vertical and spin tunes feature some spread due to energy spread of the beam and chromaticity of the machine, potentially blurring the transition between no depolarization and depolarization.
- the two resonances on each side of $Q_s^{\max}$ can have different strengths, depending on the distance between them.

The experimental results are expected to be complex and no simple theoretical model can predict the observed polarization. One solution to take everything into account would be to completely simulate the experiment. The Zgoubi code and the AGS Zgoubi on-line model provide the perfect tools for that purpose.

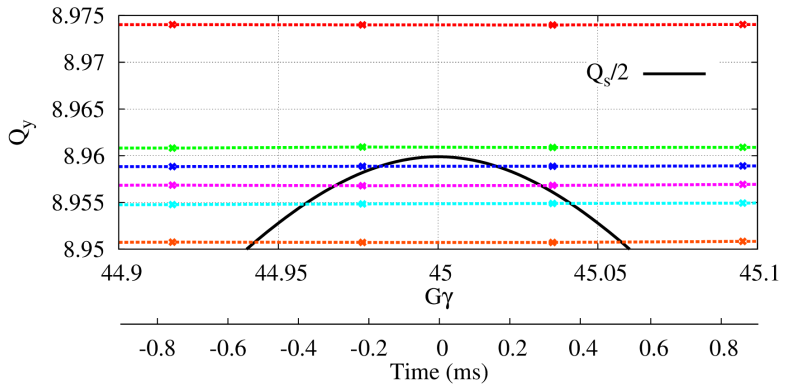

Figure 5.7 Vertical tune for the 5 different simulations, and resonant condition for the second order snake resonance ($Q_s/2$) as a function of the energy or the time from $G\gamma = 45$.

Simulation at 36+

The Zgoubi code allowed us to quickly estimate that the crossing of the second order snake resonance ($Q_S + 2Q_y = n$ with n an integer) would create a strong enough depolarization of the beam to be easily measured by the AGS polarimeter. At $G\gamma = 45$, the resonance $Q_y + 36 = Q_s$ is strong enough that the crossing of the second order snake resonance induces a significant depolarization of the beam. Beam multiturn trackings using the Zgoubi code were done for a short simulation from $G\gamma = 44.5$ to $G\gamma = 45.5$. Realistic beam and machine conditions were set up using the AGS Online model. Each simulation consists of a tracking of 408 particles picked in a realistic 6-D Gaussian distribution for 3800 turns. The simulations total up to around 20,000 CPU hours.

Figure 5.7 shows the vertical tune without tune jump at $Q_y \sim 8.975$, which is lower than the operational tune across this resonance in order to cross the spin resonance when the jump quads are fired. Below this, the different tunes on the jump were chosen across a wide range to determine the best configuration for the measurement.

Figure 5.8 shows the experiment simulated for the different vertical tunes on the jump shown in Figure 5.7. On Figure 5.8(b) the vertical tune on the jump is very close to the maximum value of the $Q_S/2$. The two vertical intrinsic resonances on either side of $G\gamma = 45$ are so close that they have the same effect on the beam and the figure is very symmetric, centered around $G\gamma = 45$. For a lower vertical tune, the result is distorted due to the two resonances having different strengths when the distance separating them increases. These simulations show that the vertical tune on the jump should be positioned as close as possible to the maximum value of the spin tune.

Experiment at 36+

In order to correctly place the vertical tune, we determined the maximum value reached by the spin tune across the resonance. By measuring the final polarization as a function of the vertical tune across $G\gamma = 45$ we determined that $Q_s^{\mathbf{max}}/2 = 0.956$. The vertical tune on the jump was placed at $Q_y = 8.954$, just below the resonant condition.

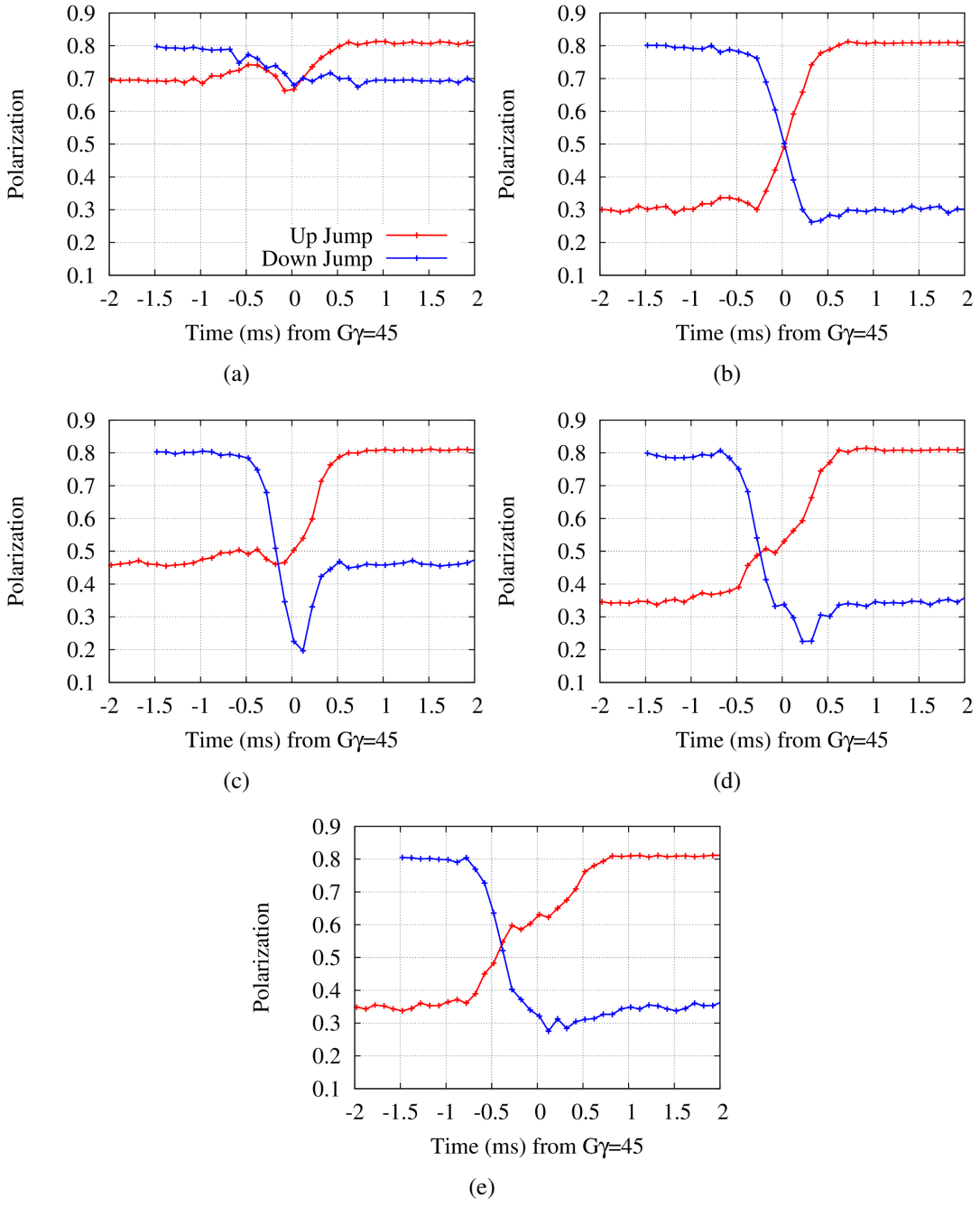

Figure 5.8 Final polarization for the up and down jump locations, as a function of the time from $G\gamma = 45$ for the vertical tune on the jump just above the second order snake resonance (a), for $Q_y = 8.951$ (e) and for the other cases shown in Figure 5.7, in decreasing order.

The polarization on the flat-top was measured as a function of the up and down jump locations, by steps of 200 μs. Figure 5.9 shows the measured data, along with the simulation closest to the experimental conditions. The simulation results were numerically matched: vertically to account for the polarization lost outside the simulated range and horizontally shifted. The matched hori-

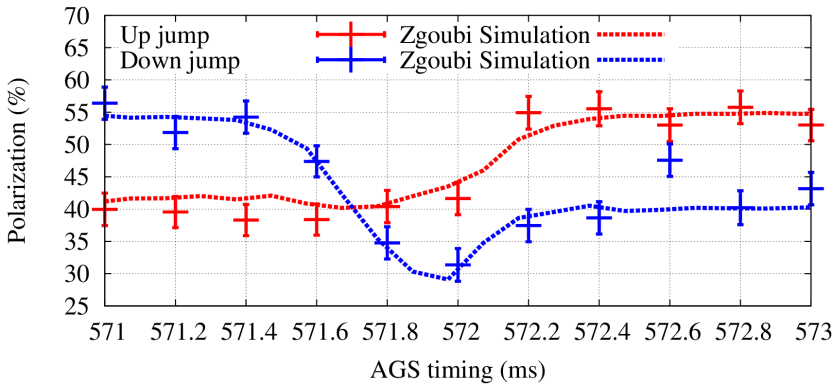

Figure 5.9 Final polarization for the up and down jump locations as a function of the AGS time.

zontal shift of the simulation allows to determine that $G\gamma = 45$ is crossed at $T = 571.85$ ms. From the *GgammaMeter* data, we expected to see $G\gamma = 45$ at T = 572.7 ms. This 850 μs difference is equivalent to $\sim 0.1\,G\gamma$.

The energy measurement at 36+ led to surprising results, but the magnitude would suffice to explain an important loss of efficiency for the tune jumps. The same method was applied at $G\gamma = 9$, where a strong vertical intrinsic resonance is located, reporting a smaller disagreement with the energy measured by the *GgammaMeter* of $\Delta T = 0.1$ ms. Therefore it would appear that the energy reported by the *GgammaMeter* drifts along the ramp. These results were used to recalibrate the the *GgammaMeter* and generate new tune jump timings. Higher polarization was measured with the new timings on June 6$^{\text{th}}$ (Table 5.2), giving strong confidence in the energy measurement. The energy measurement, based on depolarization, provided interesting results, but the procedure is complex and the data collection is very long. However, a faster method based on a continuous polarization measurement along the ramp is being developed and could be used for operations,

while the method described above would be an important tool for experts to cross-check the results.

5.2.2.4 Ramp Polarization Based Energy Measurement

Continuous polarization measurements in the AGS provide the evolution of the non-calibrated polarization, also called asymmetry, as a function of the AGS time (see Appendix D, Figure D.1). The approach exploits the spin flip occurring when the beam crosses an integer value of $G\gamma$ during

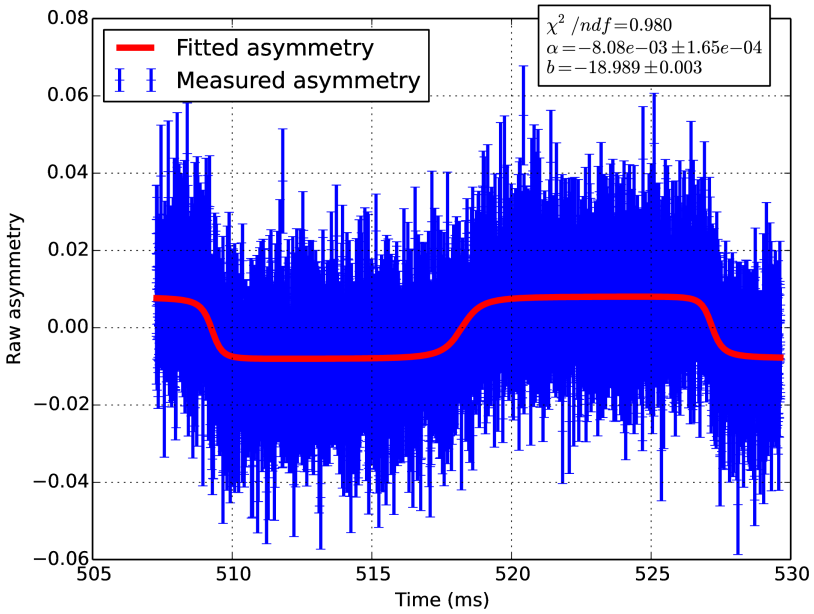

Figure 5.10 Measured and fitted asymmetry as a function of time around $G\gamma = 39$.

acceleration, due to the partial snake configuration of the AGS (Eq. 2.120). The method is described in [84] but Figure 5.10 shows the result of a measurement acquired in May 2013, around $G\gamma = 39$. The measured asymmetry is fitted by the theoretical, known, evolution of the vertical component of $\vec{n}_0$ at the polarimeter as a function of the energy $G\gamma$ (Eq. 2.120).

For Figure 5.10 the analysis provides an estimate of the timing associated with the crossing of $G\gamma = 39$ with a statistical uncertainty of around $30\,\mu$s. The repetition of the fit along the acceleration cycle offers an accurate estimate of the energy at every spin flip. This has shown to

be particularly useful to validate the energy measured with the conventional method (reported in Section 5.2.2.1).

5.3 Vertical Tune Jumps Scheme in the AGS

We have seen in Chapter 4 that the AGS vertical tune cannot be pushed high enough to overcome the first 2 vertical intrinsic spin resonances. Figure 4.9 shows the crossing of the two resonances on either side of $G\gamma = 5$.

Although the tune jump system was designed for fast change of the horizontal tune, it also changes the vertical tune by $\Delta Q_y = -0.02$ within $100\,\mu$s. It was proposed to use the vertical tune shift induced by the AGS tune jump system to accelerate the crossing of the two vertical intrinsic resonances around $G\gamma = 5$. Although each tune jump changes the tune in both planes, we define the vertical tune jump as the tune jump used to accelerate the crossing of a vertical intrinsic resonance. We will present the new scheme and hardware limitations of the system for this application. Then the gain in polarization will be estimated using multiparticle trackings with the Zgoubi code and compared to experimental data.

5.3.1 Vertical Tune Jumps Scheme Setup

Figure 5.11 shows the proposed vertical tune jumps at $G\gamma = 4.9$ and $G\gamma = 5.1$. The first constraint of this scheme is the distance between the vertical and horizontal tunes. Since the tune jump power supplies need around 3 ms between two consecutive tune jumps, the case shown in dashed lines was technically impossible. Lowering the horizontal tune allowed to increase the time between the vertical and horizontal tune jumps, as seen in Figure 5.11. In the final scheme, corresponding to the plain lines in Figure 5.11, the minimum time between two consecutive jumps is 2.8 ms. This is very close to the usual charging time and can be achieved by the current tune jump system hardware.

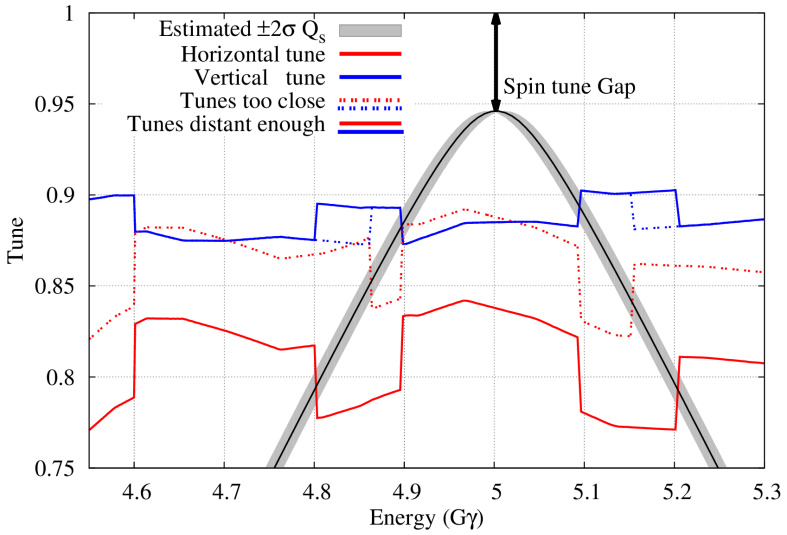

Figure 5.11 Representation of the proposed tune jump scheme around $G\gamma = 5$, using realistic tunes and energy spread.

5.3.1.1 Zgoubi Beam Multiturn Trackings

The tracking code Zgoubi and the Zgoubi AGS online model were used to simulate the effect, and expected polarization gain, of the vertical tune jump scheme. The lattice was setup using measured magnets currents and measured tunes. Unlike in Chapter 4, the snakes here were simulated using first order simplectic matrices. Although not as realistic as tracking using field maps of the snakes, the results were easier to interpret due to the particularly complex beam dynamics at low energy. Realistic longitudinal dynamics were simulated using measured acceleration rate and total RF voltage. The simulations consist of the tracking of 1000 particles picked in a 6D Gaussian distribution leading to realistic transverse normalized 95% emittances of $4\,\pi$.mm.mrad and longitudinal emittance of 1.43 eV.s. The initial spin vectors were aligned with the stable spin direction, resulting in an initial polarization of 100%. Therefore the vertical polarization profile is flat at $G\gamma = 4.5$, as measured in the machine. Figure 5.12 shows the evolution of the average polarization predicted by the Zgoubi code. The tracking results clearly show that the polarization losses are dominated by vertical intrinsic resonances, located around $G\gamma = 4.9$ and $G\gamma = 5.1$. The horizontal

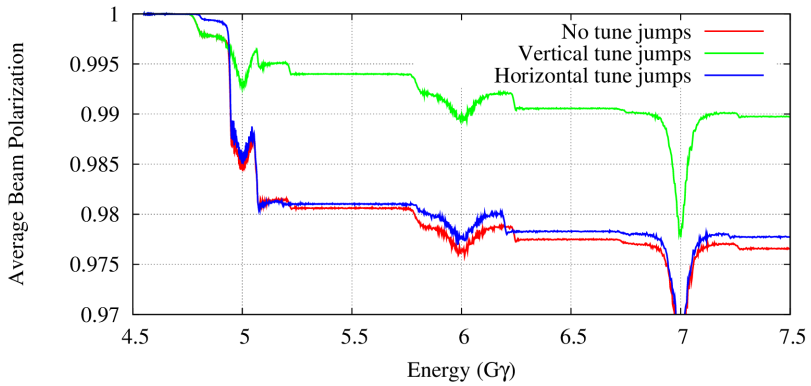

Figure 5.12 Average polarization over the whole beam as a function of the energy for different tune jump settings simulated using the Zgoubi code.

intrinsic resonances cause minor polarization drops at $G\gamma = 4.8$ and $G\gamma = 5.2$, as well as around $G\gamma = 6$ and $G\gamma = 7$. This is confirmed by the simulations with the tune jumps. While the effect of the horizontal tune jumps is negligible, we can see that the vertical tune jumps greatly reduce the polarization losses around $G\gamma = 5$. The simulations show an increase in the overall polarization transmission from the vertical tune jumps from 97.6% to 99% between $G\gamma = 4.5$ and $G\gamma = 7.5$. Assuming a final polarization of 70% at $G\gamma = 45.5$, the effect of the vertical tune jump would be an increase of 1% average beam polarization, which cannot be measured without excessively long measurements due to the statistical uncertainty inherent to the polarization measurements in the AGS.

In order to take advantage of the larger analyzing power at low energy of the AGS CNI polarimeter (see Appendix D), it was proposed to measure the effect of vertical tune jumps before the AGS extraction energy of $G\gamma = 45.5$. Measurements of the polarization were done at $G\gamma = 7.5$. The simulations were stopped and analyzed at $G\gamma = 7.5$.

Figure 5.13 shows the polarization profiles predicted by the Zgoubi code at $G\gamma = 7.5$ without tune jumps. The polarization profile in the vertical plane dominates, which is an additional proof that most of the polarization losses occurred through vertical intrinsic resonances.

Following these promising results predicted by the Zgoubi simulations, measurements in the

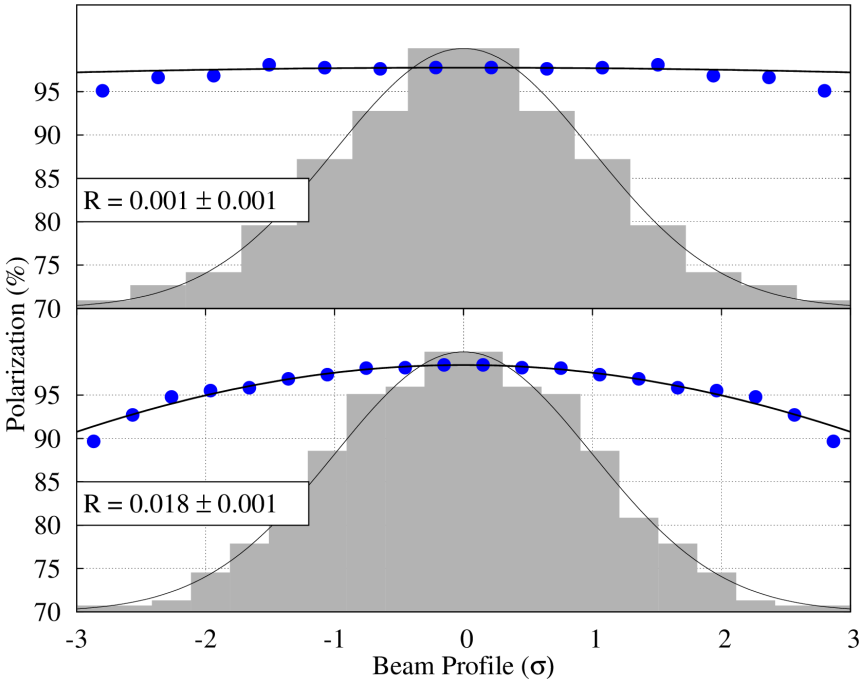

Figure 5.13 Polarization profile obtained from the Zgoubi tracking at $G\gamma = 7.5$ for the horizontal (top plot) and vertical plane (bottom plot).

AGS were conducted.

5.3.2 Experimental Results

The experimental conditions were very close to the simulations. Even though the machine tunes were slightly different from the ones used in simulations, no major impact on the results were expected. Dedicated tune jump functions were generated with only vertical tune jumps and timed to accelerate the crossing of the vertical intrinsic resonances, although the timing of the tune jump is experimentally difficult to set up perfectly. Polarization profiles were then measured at $G\gamma = 7.5$ with and without vertical tune jumps, but only in the vertical plane.

Polarization measurement at $G\gamma = 7.5$ only gives relative numbers since the analyzing power of the polarimeter is only known at $G\gamma = 45.5$. Therefore, comparing simulated and measured polarization profiles through the R allows to directly compare measurements to simulations using

the Zgoubi code. Figure 5.14 shows the result of a polarization profile measurement. The relevant

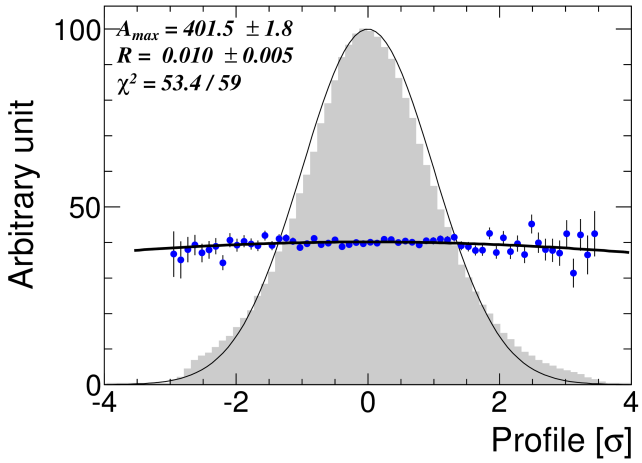

Figure 5.14 Measured vertical polarization profile at $G\gamma = 7.5$ with vertical tune jumps.

parameter is the R value and can directly be compared to the Zgoubi simulations.

Table 5.3 Summary of the measured and simulated R values of the polarization profiles.

Conditions	Horizontal	Vertical
Zgoubi simulations		
No tune jumps	0.001 ± 0.001	0.018 ± 0.001
Vertical tune jump	0.007 ± 0.001	0.003 ± 0.001
Horizontal tune jumps	0.003 ± 0.001	0.014 ± 0.001
Measured data		
No tune jumps	not measured	0.017 ± 0.005
Vertical tune jump	not measured	0.010 ± 0.005
Horizontal tune jumps	not measured	not measured

Table 5.3 summarizes the R values determined from the polarization profiles, measured and simulated using the Zgoubi code. The agreement between simulated and measured polarization profiles is very good in the absence of tune jump. However the larger horizontal profile predicted by the trackings with the vertical tune jump is not yet understood. Similarly the effect of the horizontal tune jumps on the R values are yet to be explained. Although a transfer of polarization profile between the two planes is not excluded when vertical and horizontal tunes are close. Further studies should help in understanding these effects.

Time constraints limited the quantity of measurements taken, mainly due to the large amount of time required to reach a small enough uncertainty on the measured R value.

The Zgoubi code accurately predicts the vertical polarization profile at low energy. The losses through the first 2 vertical intrinsic resonances were estimated to be large enough for a measurement, and successfully measured. A new tune jump scheme was designed and tested, again using the Zgoubi code. Hardware limitations were taken into account and the simulated tune jump scheme was successfully tested in the machine. Measurement of the vertical polarization profile with vertical tune jumps indicates a polarization gain, in agreement with the Zgoubi simulations.

This last example illustrates the design and simulation of a complex and original tune jumps scheme using the Zgoubi code. We also show that the simulated polarization profile can directly be compared to the measured one.

Conclusion

The development of the AGS Zgoubi model, described in Chapter 3, provides a tool that realistically simulates the AGS optics. The use of the measured magnet currents ensures the accuracy of the computed optics. Additionally, the Siberian snakes are modeled using 3D simulated field maps; this is particularly important since beam and spin dynamics are strongly determined by those unusual magnets.

Online capabilities were added and interface with the AGS Control System through the *ZgoubiFromSnaprampCmd* allows a fast access to the Zgoubi modeled AGS optics.

Chapter 4 introduces the parallelized multiturn beam trackings and some of the most important results. Simulated polarization using Zgoubi beam tracking showed good agreement with the measurements, in particular the depolarization through horizontal intrinsic resonances. The simulations helped to better understand the behavior of the depolarizations in the AGS, the role and challenges associated with the tune jumps system and the polarization losses dependence on different parameters.

Beam dynamics simulations also provided important insight in the low energy range. The role of some non-linear resonant lines crossing during the early range of the AGS acceleration cycle was clearly highlighted.

We have seen in Chapter 5 that Zgoubi simulations were very useful to simulate realistically many experiments. Complex schemes were tested using the Zgoubi code to investigate the possible polarization gains and to design the experiments in order to limit the required beam time. The AGS Zgoubi online model and the beam trackings provide a set of versatile and complete tools to investigate many aspects of the AGS, in order to improve machine performances.

However, some results from the beam tracking simulations disagree with experiments. In particular, measured vertical polarization profiles were not reproducible using Zgoubi simulations, hinting at polarization losses through vertical intrinsics resonances. Measurements focused on the evolution of the vertical polarization profile are schedule for the AGS Run15. Simulated beam dynamics in the low energy range is also hard to directly relate to measurements. The role of the snakes in the observed and simulated beam dynamics issues such as beam losses or emittance increase during the ramp is not yet completely understood.

Furthermore, refinements of the Zgoubi model remain to be done. As seen in Chapter 4, improvements of the beam dynamics at low energy range are necessary to completely simulate the AGS. Better understanding of the beam dynamics in the low energy could also lead to improved polarization transmission through a reduction of the transverse emittance.

Introduction of realistic orbit in the AGS Zgoubi online model and beam trackings is necessary to clearly understand the beam and spin dynamics effects in the AGS. Study of the effect of the orbit on the polarization transmission remains to be studied. Beam dynamics effect of the orbit will also be studied and could lead to improve the beam emittances and polarization at the end of the AGS acceleration cycle.

Finally, better online capabilities with the direct control of the AGS by the AGS Zgoubi online model need to be undertaken. This could simplify numerous procedures commonly carried by operations such as the orbit and optics adjustment, which might also improve the machine performances.

Bibliography

[1] F. Méot *et al.*, "Spin tracking simulations in the AGS based on ray-tracing methods," CAD AP Note 452 (2009).

[2] F. Méot *et al.*, "AGS model in Zgoubi RHIC run 13 polarization modeling status," Conf.Proc. **IPAC13, Shangai, China,** WEPEA082 (2013).

[3] F. Méot, "Zgoubi user's guide," CAD AP Note 470 (2012).

[4] S.Y. Lee, *Spin Dynamics and Snakes in Synchrotrons* (World Scientific Publishing Company, Incorporated, 1997).

[5] H. Huang, "AGS/Booster pp study," Presented at RHIC retreat (2014).

[6] A. Martin, "History of spin and statistics," CERN-TH/2002-226 (2002).

[7] J.T. Londergan, "Nucleon resonances and quark structure," Int.J.Mod.Phys. **E18,** 1135–1165 (2009).

[8] K.N. Barish, "PHENIX spin program: recent results and prospects," AIP Conf.Proc. **1523,** 182–187 (2012).

[9] A. Zelenski *et al.*, "The RHIC polarized H^- source," AIP Conf.Proc. **1149,** 847–852 (2009).

[10] A. Zelenski, "The RHIC polarized source upgrade," presented at the RHIC Spin Meeting (January 15, 2014).

[11] W.T. Weng, "Progress and status of the AGS booster project," Part.Accel. **27,** 13–20 (1990).

[12] M.Q. Barton, *Catalogue of High Energy Accelerators* (Brookhaven National Laboratory, 1961), Vol. 683.

[13] I. Nakagawa *et al.*, "RHIC polarimetry," Eur.Phys.J.ST **162,** 259–265 (2008).

[14] H. Hahn *et al.*, "The RHIC design overview," Nucl.Instrum.Meth. **A499,** 245–263 (2003).

[15] H. Huang *et al.*, "Proton emittance Measurements in the Brookhaven AGS," Conf.Proc. **IPAC13, Shangai, China,** TUPFI084 (2013).

[16] W. Fischer *et al.*, "Head-on beam-beam compensation in RHIC," ICFA Beam Dyn.Newslett. **52,** 102–107 (2010).

[17] I Pinayev *et al.*, "Progress with coherent electron cooling proof-of-principle experiment," Conf.Proc. **IPAC13, Shangai, China,** TUPFI081 (2013).

[18] C. Pai *et al.*, "RHIC spin flipper status and simulation studies," Conf.Proc. **PAC11, New-York, NY, USA,** MOP191 (2011).

[19] S. Peggs *et al.*, "The rapid cycling medical synchrotron, RCMS," Conf.Proc. **EPAC02, Paris, France,** (2012).

[20] V. Ptitsyn and eRHIC collaboration, "eRHIC future electron ion collider at BNL," AIP Conf.Proc. **842,** 1046–1048 (2006).

[21] L. Shao *et al.*, "Simulation prediction and experiment setup of vacuum laser acceleration at Brookhaven National Lab-accelerator test facility," Nuclear Instruments and Methods A **701,** 25–29 (2012).

[22] E. Bleser, "The optimum central orbit in the AGS," AGS Tech. Note 217 (1985).

[23] R. Thern and E. Bleser, "The dipole fields of the AGS main magnets," AGS Tech. Note 424 (1996).

[24] E. Wilson, "Transverse beam dynamics," in *Proceedings of CAS general accelerator physics, Gif-sur-Yvette, Paris, France* (1985), p. 64.

[25] A. Tkatchenko, "Mouvement d'une particule chargée dans un champ magnétique," Cours du DEA de physique des grands intruments, Univ. Paris XI (unpublished).

[26] E. Courant and H. Snyder, "Theory of the alternating-gradient synchrotron," Annals of Physics **3,** 1 – 48 (1958).

[27] E. Bleser and R. Thern, "The quadrupole and sextupole fields of the AGS main magnets," AGS Tech. Note 429 (1996).

[28] R. Rice, "Error sources and effects," in *Handbook of Accelerator Physics and Engineering (2nd Edition)*, edited by A. Chao, ed., (World Scientific Publishing Co., Singapore, 2012), p. 346.

[29] E. Wilson, "Non-linearities and resonances," in *Proceedings of CAS general accelerator physics, Gif-sur-Yvette, Paris, France* (1985), p. 96.

[30] E. Bleser, "Where are the AGS magnets," AGS Tech. Note 215 (1985).

[31] J. Le Duff, "Longitudinal beam dynamics in circular accelerators," in *Proceedings of CAS general accelerator physics, Gif-sur-Yvette, Paris, France* (1985), p. 128.

[32] J.A. MacLachlan, "Difference equations for longitudinal motion in a synchrotron," Fermi National Accelerator Laboratory Note 529 (1989).

[33] J.M. Brennan, "Ferrite loaded cavities," in *Handbook of Accelerator Physics and Engineering*, edited by A. Chao, ed., (World Scientific Publishing Co., Singapore, 1999), p. 524.

[34] H. Huang, "Preservation of polarization of proton beam in the AGS with partial Siberian snake," Ph.D. Thesis, Indiana University (1995).

[35] M. Bai, "Overcoming intrinsic spin resonances by using an RF dipole," Ph.D. Thesis, Indiana University (1999).

[36] P. Nghiem and A. Tkatchenko, "Simulation of proton spin motion in circular accelerators using one-turn spinor transfer maps," Nuclear Instruments and Methods A **335,** 349–366 (1993).

[37] Wolfram Research, Inc., "Mathematica," Version 9.0, Champaign, IL (2012).

[38] M. Froissart and R. Stora, "Depolarization of a polarized proton beam in a synchrotron," ANL-TRANS-570 (1968).

[39] H, Huang *et al.*, "Preservation of proton polarization by a partial Siberian snake," Phys. Rev. Lett. **73,** 2989 (1994).

[40] T. Roser, "Properties of partially excited Siberian snakes," AIP Conf.Proc. **187,** 1442–1446 (1989).

[41] F. Lin, "Towards full preservation of polarization of proton beam in the AGS.," Ph.D. Thesis, Indiana University (2007).

[42] N. Tsoupas *et al.*, "Acceleration of polarized protons in the AGS," BNL CAD Note No. 391 (2010).

[43] "Alternating gradient synchrotron project construction completion report," Brookhaven National Laboratory (1966).

[44] E. Courant, "Computation of AGS orbits with 704 computer," AGS Int. Report 36 (1960).

[45] M. Barton, "BEAM program on the PDP-10," AGS Computer Note 20 (1972).

[46] F. Iselin and J. Niederer, "The MAD program, user's reference manual," CERN/LEP-TH/87-33 (1987).

[47] L. Ahrens, "Private communication," Broohkhaven National Laboratory (2014).

[48] L. Ratner, "Gamma-transitions studies," AGS Studies Note 228 (1987).

[49] E. Auerbach, "Computer models of the AGS I," AGS Tech. Note 297 (1988).

[50] V. Schoefer *et al.*, "RHIC injector complex online model status and plans," Conf.Proc. **PAC09, Vancouver, BC, Canada,** FR5REP003 (2009).

[51] K.A. Brown *et al.*, "Improvement plans for the RHIC/AGS online Model environments," Conf.Proc. **ICAP09, San Franciso, CA, USA,** WE3IODN03 (2009).

[52] E. Bleser, "The quadrupole and sextupole fields of the AGS main magnets," AGS Tech. Note 293 (1988).

[53] E. Bleser, "Data sheets for the AGS high field quads," AGS Tech. Note 294 (1988).

[54] E. Bleser, "Data sheets for the high field chromatic sextupoles," AGS Tech. Note 294 (1988).

[55] N. Tsoupas *et al.*, "Design and measurements of a thin quadrupole magnet for the AGS synchrotron," Nuclear Instruments and Methods A **633,** 1–7 (2011).

[56] V. Schoefer *et al.*, "Incorpotating partial Siberian snakes into the AGS online model," Conf.Proc. **ICAP09, San Franciso, CA, USA,** THPSC010 (2009).

[57] A.U. Luccio, "Tracking through a Warm Helical Snake for the AGS," CAD AP Note 136 (2004).

[58] A.U. Luccio *et al.*, "Focusing of the AGS cold snake," CAD AP Note 246 (2006).

[59] M. Conte and W.Mackay, *An Introduction to the Physics of Particle Accelerators, second edition* (World Scientific Publishing Co., Singapore, 2008).

[60] E. Bleser and M. Mussorrafiti, "Calculated formulas for controlling the AGS tune," AGS Tech. Note 464 (1997).

[61] E. Bleser, "The Parameters of the bare AGS," AGS Tech. Note 430 (1996).

[62] E. Bleser, "Calculated formulas for controlling the AGS chromaticity," AGS Tech. Note 461 (1997).

[63] A.U. Luccio *et al.*, "Spink user's manual. Version v.2-21-beta," CAD AP Note 283 (2007).

[64] F. Méot, "The ray-tracing code Zgoubi - Status," Nuclear Instruments and Methods A **427,** 353–356 (1999).

[65] F. Méot, "The ray-tracing code Zgoubi - Status," Nuclear Instruments and Methods A 767 .

[66] F. Méot *et al.*, "Spin tracking simulations in AGS based on ray-tracing methods - bare lattice, no snakes," CAD AP Note 452 (2009).

[67] F. Méot *et al.*, "Zgoubi-ing AGS: spin motion with snakes and jump-quads, $G\gamma = 43.5$ through $G\gamma = 46.5$ and beyond," CAD AP Note 453 (2012).

[68] F. Méot *et al.*, "Modelling of the AGS using Zgoubi - status," Conf.Proc. **IPAC11, San Sebastián, Spain,** TUPZ039 (2011).

[69] Y. Dutheil *et al.*, "A model of the AGS based on stepwise ray-tracing through the measured field Maps of the Main Magnets," Conf.Proc. **IPAC12, New Orleans, LA, USA,** TUPPC101 (2012).

[70] C. Gardner, "Notes on orbit equations in the AGS," CAD AP Note 164 (2004).

[71] E. Bleser and R. Thern, "The dipole fields of the AGS main magnets," AGS Tech. Note 424 (1996).

[72] F. Méot *et al.*, "Modelling of the AGS using Zgoubi - status," Conf.Proc. **IPAC12, New Orleans, LA, USA,** MOPPC024 (2012).

[73] F. Méot *et al.*, "Spin dynamics simulations at AGS," Conf.Proc. **IPAC10, Kyoto, Japan,** MOPD001 (2010).

[74] A.U. Luccio *et al.*, "Cold AGS snake optimization by modeling," CAD AP Note 128 (2003).

[75] Y. Dutheil *et al.*, "Optimization of the pp AGS Zgoubi model in the low energy range," Conf.Proc. **IPAC14, Dresden, Germany,** THPRO088 (2014).

[76] F. Méot *et al.*, "AGS snake stories," Conf.Proc. **IPAC14, Dresden, Germany,** TUPRO077 (2014).

[77] L.A. Ahrens *et al.*, "Measurement of the chromaticities and eddy current effects," AGS Study Note 206 (1986).

[78] F. Méot , "Zgoubi code," http://sourceforge.net/projects/zgoubi/ (Accessed December 2014).

[79] H, Huang *et al.*, "Overcoming horizontal depolarizing resonances with multiple tune jumps," Phys. Rev. ST Accel. Beams **17,** 081001 (2014).

[80] K. Smith, "Private communication," Broohkhaven National Laboratory (2014).

[81] H. Huang *et al.*, "RHIC polarized proton operations for 2013," Conf.Proc. **IBIC13, Oxford, UK,** TUPF01 (2013).

[82] K. Zeno, "Private communication," Broohkhaven National Laboratory (2014).

[83] Y. Dutheil *et al.*, "New tune jumps Scheme in the low energy part of the AGS cycle," Conf.Proc. **IPAC14, Dresden, Germany,** THPRO089 (2014).

[84] Y. Dutheil *et al.*, "Energy calibration and tune jumps efficiency un the AGS pp," Conf.Proc. **IPAC14, Dresden, Germany,** THPRO090 (2014).

[85] Y. Dutheil *et al.*, "Energy calibration in the AGS using depolarization through vertical intrinsic spin resonnaces," Conf.Proc. **NAPAC13, Pasadena, CA USA,** TUPAC10 (2013).

[86] H. Huang *et al.*, "p-Carbon CNI polarimetry in the AGS and RHIC," Conf.Proc. **EPAC08, Genoa, Italy,** TUPC039 (2008).

Appendix A

Main Magnet Field Map Positioning

Tracking through measured field maps of the main magnets requires a change of reference frame in the Zgoubi model of the AGS. The element `'CHANGREF'` is used and an example in the case of the A-type magnet is given below:

```
'CHANGREF' TOP
ZR 0.801138237   YS -0.5564124   XS -38.1
'TOSCA'
[...]
'CHANGREF' BOTTOM
XS -38.1   YS 0.5564124   ZR 0.801138237
```

Each `'CHANGREF'` element consists of 3 successive changes of referential before the field map:

- a rotation around $\vec{y}$ corresponding to half the deviation of the *OCO* across the magnet, 0.801138237° for the long magnets and 0.6732941642° for the short magnets.
- a horizontal translation along $\vec{x}$ corresponding to the distance between the *OCO* and *SOCKET* systems, 5.564124 mm for the long magnets and 3.929888 mm for the short magnets.
- a longitudinal translation since the field maps are longer than the magnetic length of the magnets by 38.1 cm on each side.

After tracking through the magnet, the referential is changed again in reverse order to carry the tracking in the *OCO* system.

Appendix B

Computed Quadrupole and Sextupole Strengths of the AGS Main Magnets

Table B.1 Computed quadrupole strengths of the AGS main magnets using the Zgoubi code, by tracking through measured field maps.

Intensity (Amps)	Equilibrium momentum (GeV/c)	AD	AF	BD	BF	CD	CF
		($10^{-2}\,\mathrm{m}^{-2}$)					
108	0.65084943	-4.8327	4.8407	-4.8227	4.8295	-4.8953	4.9060
360	2.0952495	-4.8627	4.8714	-4.8492	4.8565	-4.8519	4.8633
1000	5.8006843	-4.8714	4.8793	-4.8575	4.8643	-4.8394	4.8503
2650	15.355370	-4.8750	7.8834	-4.8605	4.8676	-4.8387	4.8494
3550	20.546276	-4.8677	4.8767	-4.8518	4.8595	-4.8324	4.8439
4450	25.625960	-4.8524	4.8637	-4.8328	4.8323	-4.8186	4.8320
4800	27.495482	-4.8445	4.8566	-4.8221	4.8323	-4.8115	4.8260
5150	29.241457	-4.8250	4.8350	-4.7997	4.8105	-4.7919	4.8071

Table B.2 Computed sextupole strengths of the AGS main magnets using the Zgoubi code, by tracking through measured field maps.

Intensity (Amps)	Equilibrium momentum (GeV/c)	AD	AF	BD	BF	CD	CF
		(10^{-3} m^{-3})					
108	0.65084943	-12.961	-13.516	-14.452	-14.968	-2.987	-3.113
360	2.0952495	-8.196	-8.136	-9.547	-9.703	-8.192	-8.229
1000	5.8006843	-6.420	-6.315	-7.732	-7.619	-8.923	-9.038
2650	15.355370	-6.465	-6.651	-7.894	-8.036	-8.328	-8.772
3550	20.546276	-7.662	-7.736	-9.180	-9.229	-9.173	-9.568
4450	25.625960	-10.601	-10.601	-12.568	-12.537	-11.867	-12.073
4800	27.495482	-13.556	-13.495	-15.715	-15.723	-15.077	-15.351
5150	29.241457	-18.971	-18.742	-21.143	-21.067	-20.547	-21.007

Appendix C

Typical Input File for the AGS Online Zgoubi Model

```
  [SNAP RAMP DIRECTORY]  ! path of the folder containing the snapramp
/operations/app_store/RunData/run_fy13/fullRun/Ags/Snapramp/13Apr14/ppmUser4/A13Apr14

  [TEMPLATE DATA FILE]  ! template zgoubi input file containing the AGS lattice
./templateZgoubi4ZgoubiFromSnaprampCmd.dat

  [TIMINGS]  ! list of timings or first, last and timing step
  145 610 3

  [GNUPLOT OPTICS TABLE]  ! 1/0 to respectively plot the optics for each timings or n
  1

  [AGS MODEL DATA]
 0   0  1           ! 0/1/2 for main magnet model as AGSMM/ MULTIPOL/ TOSCA
 0                  ! 0/1/2/3 to activate some or all orbit bumps
 0  0.d0  0.00      ! to use the measured average beam radius for off-momentum beams
```

```
 1  0               ! 1/2 for the quadrupole model AGSQUAD/MULTIPOL and 0/1 for tune
### db0  values for the 6 MM types
0.   0.  0.  0.  0.  0.
### db1 values for the 6 MM types
1.   1.  1.  1.  1.  1.
### db2 values for the 6 MM types
1.   1.  1.  1.  1.  1.
0

  [GET BETA FUNCTIONS]  ! to control and plot the beta function along the lattice
  1 1 1

 [FIT TUNES]  ! to control the adjustment of the tunes using measured data
1 1  1 1
'FIT2'
2   nofinal
 4    4   0  [-5.e-1, 5.e-1]
 4   10   0  [-5.e-1, 5.e-1]
2     1.0000E-8   1000
 0.10  7  7  956   0.695548111   1.000000 0
 0.10  8  8  956   0.876328559   0.800000 0
./Chroma_1.out
1 2 6
```

Appendix D

AGS Polarimeter

The AGS polarization measurement system is a Coulomb-Nuclear Interference polarimeter[2] located in the AGS C15 straight section [41, 86]. The measurement of the beam polarization is done by plunging a thin carbon strip target in the beam and by measuring the asymmetry A_s of recoiled carbon nucleus scattered by the polarized protons of the beam. The AGS polarimeter determines the average vertical spin component $< S_y >$ of the particles crossing the target, related to the measured asymmetry by the analyzing power A_P, only known at $G\gamma = 45.5$:

$$< S_y >= A_s \times A_P \tag{D.1}$$

Furthermore, the absolute polarization P is related to $< S_y >$ by:

$$< S_y >= P \times \vec{n}_0.\vec{y} \tag{D.2}$$

However, at the location of the polarimeter and at $G\gamma = 45.5$ we have $\vec{n}_0.\vec{y} \sim 0.99$ such that the measured $< S_y >$ is very close to the beam polarization. When the beam polarization is measured with the AGS polarimeter the factor $\vec{n}_0.\vec{y}$ is neglected and the analyzing power at $G\gamma = 45.5$, $A_P(G\gamma = 45.5)$, is always used.

The absolute polarization measurement can only be carried at extraction energy while A_s (also referred to as *relative polarization*) can be measured at any energy. This is a strong limitation of

[2]CNI polarimeter

the system and, for instance, dramatically complicates the localization of depolarizations during the acceleration ramp. This system can function in three different modes:

- In the fixed target mode the target is moved to the center of the beam. In this case the polarization is averaged over one plane, while it is the "core" polarization of the other plane being measured. For instance if the horizontal target is used, the polarization measured is averaged on the horizontal plane while only the *core* polarization from the vertical plane is sampled. This measurement typically requires 20 to 30 AGS cycles when done at the extraction energy, with nominal beam intensity and emittances. The measure obtained is only absolute at $G\gamma = 45.5$, and measurements done at other energies cannot be compared to simulations since calibration data associated to the CNI polarimeter only exists for $G\gamma = 45.5$.

- Derived from the fixed target mode has recently been developed the ramp measurement mode. In this configuration the target is plunged into the beam at the AGS injection and maintained into the beam along the ramp. Figure D.1 shows the measured asymmetry along the AGS cycle, clearly showing the effect of the partial snake configuration with the spin flip during acceleration. It can also be seen that the maximum measured asymmetry decreases fast along the AGS cycle, mainly due to the decrease in analyzing power since polarization changes are too small to be seen in Figure D.1.

- In the sweep mode, the target is swept across the beam while the beam is kept at constant energy. From this measurement one can extract the intensity and measured asymmetry as a function of the target position. Figure 4.8 shows the result of a typical polarization profile measurement. The relevant quantity is the the *R*-value, constructed from the standard deviations σ_P and σ_I, respectively, from the Gaussian fit of the polarization and intensity profiles:

$$R = \left(\frac{\sigma_P}{\sigma_I}\right)^2 \tag{D.3}$$

  The *R*-value characterizes the depolarization of the beam due to the crossing of intrinsic depolarization resonances [41]. Furthermore, the *R*-value measured does not depend on A_P such that this measurement can be done at any energy and directly compared to simulations.

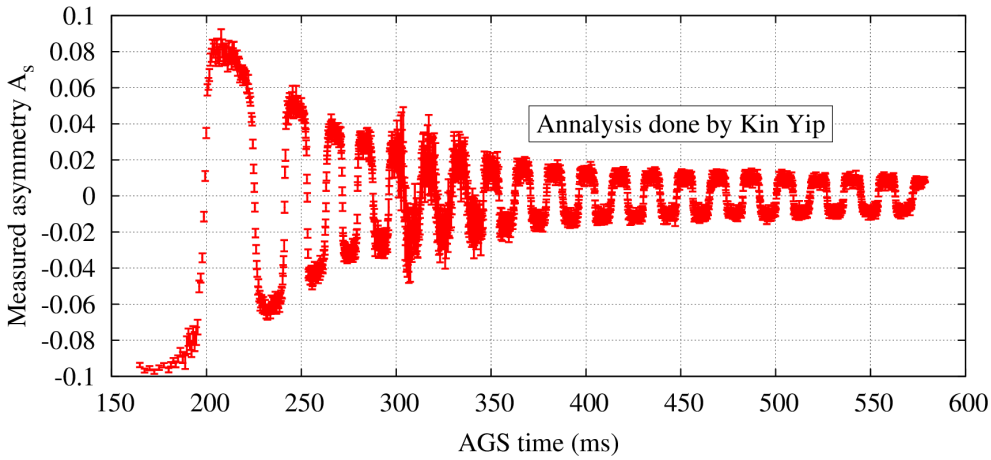

Figure D.1 Asymmetry measured by the AGS polarimeter along the acceleration cycle with typical polarized protons beam and machine conditions.

Appendix E

Résumé en français

Résumé

L'AGS fournit un faisceau de protons polarisés à RHIC. Le faisceau est accéléré dans l'AGS de $G\gamma = 4.5$ à $G\gamma = 45.5$ et la transmission de la polarisation est critique pour le programme de spin de RHIC. Au cours des dernières années, divers systèmes ont été mis en place pour améliorer la transmission de la polarisation dans l'AGS. Ces améliorations consistent essentiellement en l'introduction de deux serpents siberien partiaux et du système de saut de nombre d'onde. Cependant, la transmission de la polarisation n'atteint pas encore 100 % durant le cycle d'accélération de l'AGS. L'efficacité actuelle de la transmission de la polarisation est estimée à environ 85 % dans les conditions de fonctionnement typiques.

Comprendre les sources de dépolarisation dans l'AGS est essentiel pour améliorer les performances en protons polarisés de la machine. La dynamique de faisceau et de spin, notamment en présence des aimants spécialisés appelés serpent sibériens, justifient le fort intérêt pour des méthodes de simulation originales. Le code Zgoubi, capable de résoudre l'équation du mouvement et de l'évolution du spin directement à partir d'une carte de champs, est utilisé pour modéliser l'AGS.

Un modèle de l'AGS utilisant le code Zgoubi a pour cette raison été développé et interfacé avec le système actuel par une simple commande: l'*AgsFromSnapRampCmd*. L'interfaçage avec le système de contrôle de la machine permet la modélisation rapide en utilisant les paramètres réels la machine. Ces développements ont permis de reproduire fidèlement l'optique de l'AGS le long

du cycle d'accéleration. Des développements supplémentaires sur le code Zgoubi, ainsi que sur des outils de post-traitement et de pré-traitement, ont fournis au code la possibilité de suivre les faisceaux sur de nombreux tours, ce qui s'avère être fondamental pour une représentation réaliste du cycle d'accélération complet de la machine.

Des simulations de faisceaux sur de nombreux tours dans l'AGS, en utilisant des conditions réalistes de faisceau et de machine, ont fourni une vision unique des mécanismes sous-jacents de l'évolution de l'émittance et de la polarisation du faisceau au cours du cycle d'accélération. Des programmes de post-traitement ont été développés pour permettre la représentation des quantités pertinentes des données simulées par Zgoubi. Les simulations se sont avérées particulièrement utiles pour mieux comprendre les pertes de polarisation à travers les résonances horizontales intrinsèques de spin.

Le modèle Zgoubi ainsi que les outils développés ont également été utilisés pour certaines applications directes. Par exemple, les simulations d'expériences de faisceau ont permis l'estimation précise des gains de polarisation attendus en fonction des changements apportés. En particulier, des simulations d'expériences impliquant le système de saut du nombre d'onde ont fournis des estimations précises de la polarisation gagnée et permis le choix des conditions optimales de la machine.

E.1 Introduction

E.1.1 Le proton, le spin et la crise du spin du proton

Le spin d'une particule est son moment cinétique intrinsèque. Il joue un rôle très important dans la physique moderne, mais c'est en physique des particules que le spin est particulièrement difficile à comprendre. Alors qu'il est clairement établi que le proton est une particule composite de spin $^1/_2$, la question est de comprendre comment le spin est distribué parmi ces composants [6].

En chromodynamique quantique, le proton est composé de trois quarks de valence, de gluons et d'une mer de quarks (paires de quarks anti-quarks virtuels). Les quarks sont des particules élémentaires de spin $^1/_2$ et les gluons sont de spin 1. Pendant longtemps, il a été communément admis que seuls les trois quarks du proton contribuaient à son spin. Cependant, en 1987, l'EMC[1] réalisa une expérience de diffusion profondément inélastique de muons sur une cible de protons pour mesurer la contribution des quarks au spin du proton. Les résultats ont montré que les spins des quarks de valence et de la mer de quarks (Σ) ne contribuent pas a plus de 30% du spin du proton, au lieu des 100% attendus. Cela a été une grande surprise pour la communauté scientifique et a conduit à une crise théorique souvent désignée comme la *crise du spin du proton* [7]. Il a ensuite été établi que la fraction manquante du spin devait être créée par le spin des gluons (ΔG), le moment cinétique orbital des gluons (L_{G}) et le moment cinétique orbital des quarks(L_{q}). Les contributions au spin du proton peuvent être résumées par:

$$\frac{1}{2} = \frac{1}{2}\Sigma + \Delta G + L_{\mathrm{q}} + L_{\mathrm{G}} \tag{E.1}$$

E.1.2 Aperçu et ambitions du programme de spin de RHIC

RHIC[2] est le premier collisionneur de protons polarisés à haute énergie. Il a été construit à BNL [3] en 2001. RHIC est capable aujourd'hui de fournir des collisions de protons polarisés à des énergies allant jusqu'à $\sqrt{s} = 510\,\mathrm{GeV}$ avec une polarisation moyenne du faisceau de 50 à 55 %. Des énergies de $\sqrt{s} = 510\,\mathrm{GeV}$ ou $\sqrt{s} = 200\,\mathrm{GeV}$ et des collisions de protons polarisés transversalement ou

[1] European Muon Collaboration
[2] Collisionneur d'ions lourds relativistes
[3] Brookhaven National Laboratory

longitudinalement permettent d'explorer diverses caractéristiques de la structure de spin du proton. Les deux expériences STAR [1] et PHENIX [2] ont récemment montré, pour la première fois, une valeur non nulle de la contribution des gluons au spin du proton [8]. Dans les années à venir, le programme de spin de RHIC devrait être étendu à des collisions de protons polarisés avec des noyaux ^{3}He polarisés ainsi qu'avec d'autres ions lourds. Le programme de physique de RHIC n'a pas pour seul but d'explorer la structure du spin du proton, dans le cadre du programme d'ions lourds il donne également l'occasion d'étudier certains effets de "*cold QCD matter*" grâce aux collisions entre protons et ions.

Quelle que soit la physique étudiée, la polarisation des faisceaux de protons est primordiale. Bien qu'en général le facteur de mérite croisse linéairement avec la luminosité intégrée, il évolue de manière quadratique ou même à l'ordre 4 avec la polarisation du faisceau, selon le phénomène physique exploré. Cela conduit à un fort intérêt pour l'amélioration de la polarisation du faisceau de protons.

Alors que les faisceaux de protons sont produits polarisés, leur polarisation ne peut que décroître pendant l'accélération à travers la chaine des accélérateurs du complexe de RHIC. Des pertes de polarisation sont observées à travers les deux derniers étages d'accélération: dans l'AGS[3] et dans RHIC. Par conséquent, l'augmentation de la transmission de la polarisation à travers l'AGS est critique pour le programme de physique de RHIC.

E.1.3 Chaine d'accélération de protons polarisés à BNL

La chaine d'accélérateurs utilisée a BNL pour accélérer des protons polarisés jusqu'à 255 GeV est schématisée Figure E.1. L'OPPIS[4] produit des ions H^- polarisés selon un processus complexe impliquant de multiples étapes [9]. Les ions H^- sont ensuite ionisés et les protons résultants injectés dans le linac. Le linac, de type DTL[5], accélère des paquets de protons à une énergie de 200 MeV. Le polarimètre présent à la fin du linac permet de mesurer une polarisation d'environ 82 % [10].

[1] *Solenoidal Tracker at RHIC*
[2] *Pioneering High Energy Nuclear Interaction eXperiment*
[3] *Alternatif Gradient Synchrotron*
[4] *Optically Pumped Polarized Ion Source*
[5] *Drift Tube Linac*

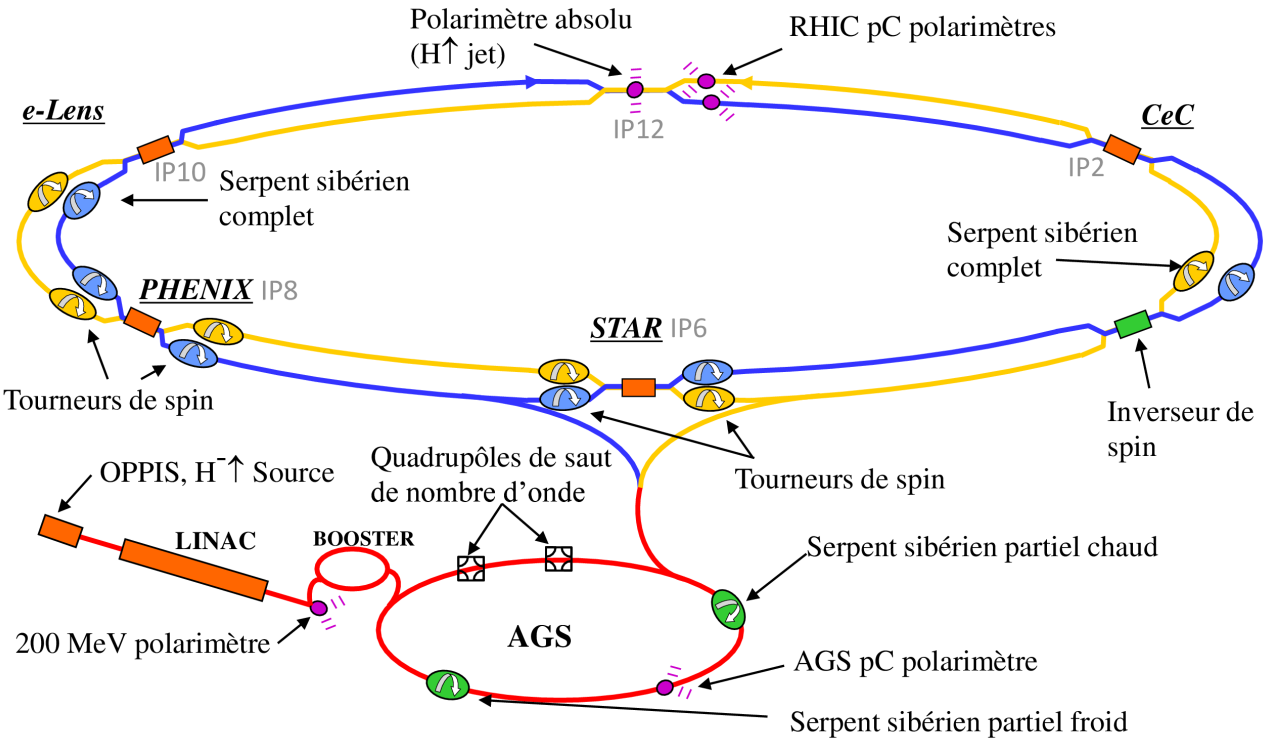

Figure E.1 Schéma de la chaine d'accélération des protons polarisés du complexe de RHIC.

L'étage suivant d'accélération est le Booster, un synchrotron basé sur une maille de type FODO et d'une circonférence de 201.7 m. Le faisceau est capturé puis accéléré dans un unique paquet jusqu'à une énergie de 2.36 GeV en approximativement 90 ms. La préservation de la polarisation durant l'accélération ne fait pas intervenir d'équipements spécialisés mais requiert une gymnastique particulière de l'orbite et du nombre d'onde vertical.

L'AGS est le deuxième synchrotron du complexe. Basé lui aussi sur une maille de type FODO, il est quatre fois plus grand que le Booster avec une circonférence de 807.1 m. Le cycle d'accélération permet d'accélérer un unique paquet de protons jusqu'à une énergie de 25.38 GeV en environ 450 ms. La Figure E.1 montre plusieurs éléments spécialisés présents sur la maille de l'AGS. Les deux serpents sibériens partiaux sont des aimants produisant un puissant champ dipolaire entrelacé permettant de préserver la polarisation durant l'accélération. Les deux quadrupôles de saut de nombre d'onde sont utilisés pour améliorer la transmission de la polarisation durant l'accélération des protons polarisés. Le polarimètre mesure une polarisation du faisceau à l'énergie d'extraction d'environ 72 %.

Le dernier étage du complexe est le synchrotron RHIC. Les aimants de RHIC sont supraconducteurs et donc maintenu a une température de 4 K permettant d'atteindre des champs dipolaires d'environ 3.5 T. Deux tubes à vide indépendants permettent d'accélérer deux faisceaux de protons, tournants dans des direction opposées, à des énergies maximales de 255 GeV. Les deux faisceaux se croisent en 6 endroits, nommé IP1 à IP6. Des collisions entre les deux faisceaux se produisent à l'IP6 ainsi qu'à l'IP8, autour desquels les détecteurs STAR et PHENIX enregistrent les évènements. La Figure E.1 montre de nombreux dispositifs présents sur la maille de RHIC, tous spécialisés dans la manipulation, la mesure, ou la préservation de la polarisation des faisceaux de protons. En particulier les polarimètres présents permettent de mesurer une polarisation d'environ 50 à 55 % à une énergie de 255 GeV.

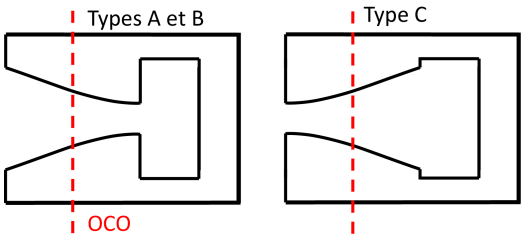

Figure E.2 Dessin schématique de la coupe transversale des aimants principaux de l'AGS.

E.2 Théorie de dynamique des faisceaux de spin dans l'AGS

E.2.1 La maille de l'AGS

L'AGS utilise des aimants à fonctions combinées produisant à la fois un champ dipolaire pour le guidage des particules et un champ quadrupolaire pour le maintien de la cohésion du faisceaux. Le Tableau E.1 résume les paramètres pertinents de l'optique de l'AGS.

Les aimants principaux de l'AGS se déclinent en 2 familles selon leur coupe transversale. La Figure E.2 montre la coupe transversale des deux types d'aimants. Les aimants A et C sont long de 90 pouces tandis que les aimants de type B sont plus courts, avec 75 pouces. Ces longueurs correspondent aux longueurs physiques des aimants mais nous utiliserons préférentiellement leur longueur effective définie comme étant plus longues de 4 pouces [30]. Chaque aimant peut avoir un effet défocalisant ou focalisant sur le faisceaux, suivant son orientation. La fonction d'un aimant est définie par son effet sur le plan horizontal. Par exemple un aimant de type C a un effet focalisant lorsque le côté ouvert est dirigé vers l'extérieur de l'anneau, l'inverse étant vrai pour les aimants de type A ou B.

La Figure E.4 montre la structure de base d'une super-période de l'AGS. La super-période est faite de 5 cellules FODO et de 20 aimants principaux. Les côtés ouverts sont orientés vers le centre de l'anneau dans la première moitié de la super-période et vers l'extérieur dans la seconde moitié. La maille de l'AGS est définie par deux types d'éléments: les aimants principaux et les sections droites. Un système de numérotation a été créé pour localiser un élément dans la maille en utilisant la lettre associée à la super-période suivie par le numéro de l'aimant principal. Par exemple, le 5^{e} aimant principal de la 3^{e} super-période est nommé "MM C05" la section droite en aval est appelé

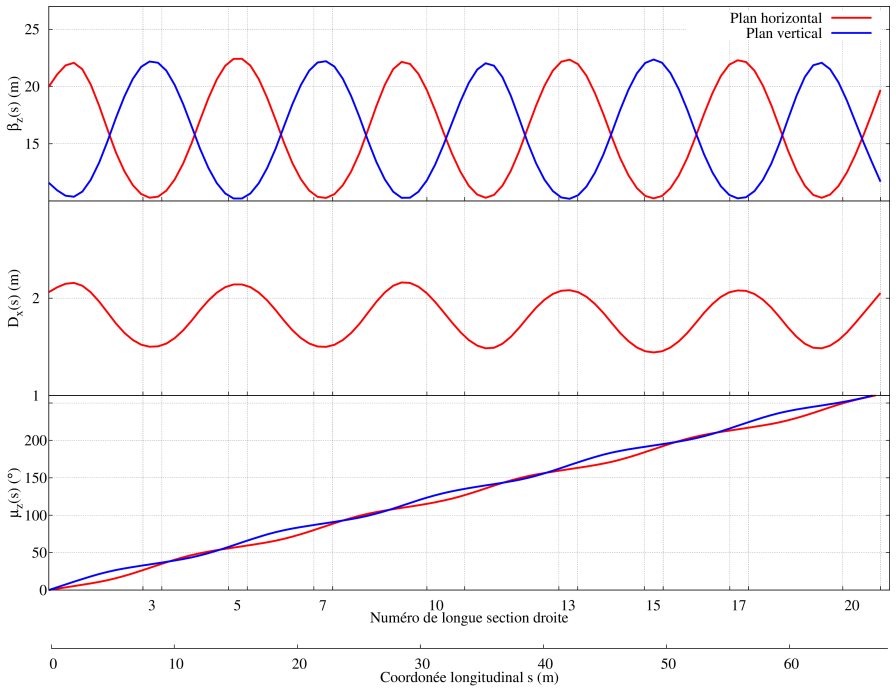

Figure E.3 Graphique des fonctions optiques le long d'une super-période de l'AGS. Le dernier graphique montre l'évolution de l'avance de phase dans les deux plans transversaux le long de la super-période.

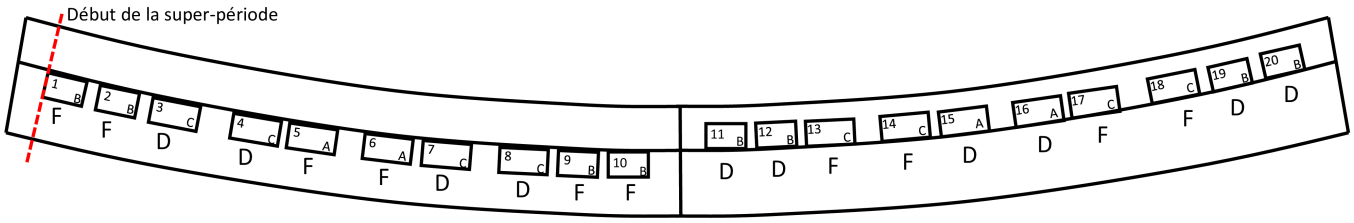

Figure E.4 Dessin synoptique d'une super-période de l'AGS avec le côté ouvert de chaque aimant orienté vers la ligne centrale. Le numéro, le type et la fonction de chaque aimant sont également indiqués. Le début de la super-période est, par convention, définie au bord magnétique du premier aimant principal.

"SS C05".

La Figure E.3 montre la position des longues sections droites de la maille de l'AGS. Les sections droites en positions 10 et 20 font 10 pieds de long, tandis que les autres font 5 pieds de long. Les sections droites qui ne sont pas mentionnées dans la Figure E.3 font seulement 24 pouces de

Table E.1 Important paramètres optique et d'acceleration de l'AGS, dans le cas de proton polarisés à l'énergie d'extraction.

Paramètre		Valeur
Energie (totale)	E	23.8 GeV
Circonférence	C	807.091 m
Nombre d'onde horizontal	Q_x	8.69
Nombre d'onde vertical	Q_y	8.73
Fréquence de révolution	f_{rev}	372 kHz
Nombre d'harmonique RF	h	8
Vitesse maximal de rampe du champ dipolaire	$\dot{B}_{max}$	$\approx 2.5\,\mathrm{T.s^{-1}}$
Volage RF maximal	$\hat{V}_{RF}$	$\approx$ 280 kV
Gamma de transition	γ_{tr}	8.5
Nombre d'onde synchrotron	Q_s	3.4

long et accueillent uniquement les BPM [1], les stations de pompage ou les correcteurs dipolaires utilisés pour la correction de l'orbite.

[1] *Beam Position Monitor*

E.2.2 Dynamique de spin dans l'AGS

Pour une particule en mouvement, la transformation du champ magnétique dans le référentiel du laboratoire vers le référentiel de la particule conduit à l'équation de Thomas-BMT, en l'absence de champ électrique :

$$\frac{\mathrm{d}\vec{S}}{\mathrm{d}t} = \frac{e}{m_0\gamma}\vec{S}\times\left[(1+G\gamma)\vec{B}_{\perp}+(1+G)\vec{B}_{\parallel}\right] \tag{E.2}$$

Avec $\vec{\beta}=\vec{v}/c$, e la charge du proton, m_0 sa masse, G son moment magnétique anomal et γ le facteur de Lorentz. Sont aussi introduits les composantes du champ magnétique $\vec{B}_{\perp}$ et $\vec{B}_{\parallel}$ respectivement orthogonale et parallèle à $\vec{\beta}$.

Dans le cas d'une particule circulant sur la trajectoire de réference, les champs magnétiques rencontrés sont uniquement verticaux et $\vec{B}=B_0\vec{y}$. L'équation E.2 prend alors sa forme la plus simple :

$$\vec{\Omega}_S = -\frac{q}{m_0\gamma}(1+G\gamma)B_0\vec{y} \tag{E.3}$$

où $\vec{\Omega}_S$ est la fréquence de précession du spin.

Dans ces conditions l'équation de Lorentz peut être écrite :

$$\frac{\mathrm{d}\vec{v}}{\mathrm{d}t} = \vec{\Omega}_c\times\vec{v} \tag{E.4}$$

avec $\vec{\Omega}_c$ la fréquence cyclotron relativiste qui caractérise la fréquence de révolution de la particule autour de la machine. Il est intéressant de comparer la fréquence cyclotron à la fréquence de précession du spin.

$$\frac{\Omega_S}{\Omega_C} = 1+G\gamma \tag{E.5}$$

Dans le référentiel tournant, le spin fait $G\gamma$ tours autour de l'axe vertical par tour de l'AGS. Par analogie avec le nombre d'onde bêtatron, est définie une quantité capitale en dynamique de spin appelé le nombre d'onde de spin Q_S. Dans le cas d'une machine circulaire, Q_S est le nombre d'onde de spin non perturbé sur l'orbite de référence :

$$Q_S = G\gamma \tag{E.6}$$

Dans un synchrotron comme l'AGS, le nombre d'onde de spin est très important et $G\gamma$ est souvent utilisé comme unité de l'énergie des particules.

E.2.2.1 Résonances de spin d'epolarisantes

Les champs magnétiques horizontaux rencontrés par les particules perturbent la précession du spin autour de l'axe vertical. La sommation cohérente de ces champs le long de la machine peut conduire à une perte de polarisation du faisceau. Il existe deux types de résonances de spin dépolarisantes en fonction des valeurs prises par le nombre d'onde de spin :

- lorsque la relation $Q_S = K$, avec K un entier, est satisfaite on parle alors de résonance de spin d'imperfection. Dans ce cas les champs perturbateurs horizontaux dus à l'orbite fermée verticale causent une perte de polarisation. Il est intéressant de noter que ce type de résonance de spin n'existe pas dans le cas d'une machine idéale, sans orbite fermée verticale.

- lorsque la relation $Q_S = K \pm Q_y$, avec Q_y le nombre d'onde bêtatron vertical, est satisfaite on parle alors de résonance de spin intrinsèque. Dans ce cas ce sont les champs perturbateurs horizontaux dus au mouvement bêtatron vertical qui sont responsables de la dépolarisation. La dépolarisation due à ce type de résonance existe même dans le cas d'une machine idéale, du moment qu'une émittance verticale non nulle est considérée.

E.2.2.2 Dynamique de spin en présence de serpents sibériens

Dans les années 70, Derbenev et Kondratenko proposèrent de surmonter les résonances de spin dépolarisantes dans les accélérateurs circulaires en utilisant un rotateur local de spin, capable de faire tourner le vecteur de spin de 180° autour de l'axe horizontal et couramment appelé serpents sibériens complets. Alors que dans un accélérateur circulaire plan classique $Q_S = G\gamma$ et la direction de précession de spin pour une particule circulant sur l'orbite de référence, $\vec{n}_0$, est vertical le long de la machine, l'introduction d'un serpent Sibérien complet modifie ces grandeurs qui deviennent alors :

$$t(\theta + 2\pi, \theta) = e^{-\frac{i}{2}G\gamma(2\pi-\theta)\sigma_y} e^{-\frac{i}{2}\pi\sigma_s} e^{-\frac{i}{2}G\gamma\theta\sigma_y} \tag{E.7}$$

(a) (b)

Figure E.5 Image du serpent sibérien supraconducteur dans la section droite A20 (a) et du serpent sibérien normal-conducteur dans la section droite E20 (b).

et

$$Q_S = \frac{1}{2} \quad \text{and} \quad \vec{n}_o = \begin{pmatrix} -\sin\left(G\gamma(\pi-\theta)\right) \\ -\cos\left(G\gamma(\pi-\theta)\right) \\ 0 \end{pmatrix} \tag{E.8}$$

Il est intéressant de noter que le nombre d'onde de spin est maintenant constant et indépendant de l'énergie. L'utilisation d'un unique serpent Sibérien complet permet donc de s'affranchir des résonances de spin dépolarisantes.

Dans le cas de RHIC, nous pouvons voir Figure E.1 que deux serpents sibériens complets par anneau sont utilisés. Cette configuration permet aussi de fixer $Q_S = \frac{1}{2}$ mais maintient aussi $\vec{n}_o = \vec{y}$.

Dans le cas de l'AGS il n'est pas possible d'utiliser des serpents sibériens complets. Alors que les sections droites les plus longues de l'AGS font environ 3 m, un serpent sibérien complet tel que ceux fabriqué pour RHIC fait environ 10 m de long. L'AGS utilise deux serpents sibériens partiaux. Le schéma utilisé ici est composé de deux serpent sibériens partiaux séparés par un tiers de l'anneau [40]. Les serpents sibériens ont été construits pour être suffisamment courts afin de rentrer dans une longue section droite de l'AGS tout en offrant un angle de précession du spin de 10 à 20 degrés autour de l'axe longitudinal. Cette configuration ne permet pas, contrairement au schéma utilisé dans RHIC, de fixer le Q_S et $\vec{n}_o$. Cependant cette configuration permet de s'affranchir naturellement des résonances de spin d'imperfection et le placement du nombre d'onde bêtatron vertical près de

l'entier, typiquement à $Q_y = 8.98$, permet aussi de s'affranchir des résonances de spin intrinsèques.

Cette configuration présente cependant deux difficultés :

- les serpents sibériens présentent une conception et des champ magnétiques particulièrement complexes afin d'atteindre les angles de précession requis, tout en maintenant une longueur suffisamment courte. Ces champs, dont des composantes non linéaires importantes, causent de nombreuses limites en terme de dynamique de faisceaux et d'ouverture dynamique. En particulier l'optique à basse énergie, typiquement en dessous de $G\gamma = 6$, est fortement distordue par les serpents sibériens.

- alors que $\vec{n}_o$ possède une composante non nulle dans le plan horizontal, un nouveau type de résonance de spin dépolarisante est crée. Les champs perturbateurs peuvent désormais s'ajouter dû au mouvement bêtatron horizontal et un nouveau type de résonance intrinsèque dépolarisante dite horizontale est créé. La condition résonnante associée aux résonances dépolarisantes intrinsèques horizontales est $Q_S = K \pm Q_x$, avec Q_x le nombre d'onde bêtatron vertical.

E.3 Modèle de l'AGS et application

E.3.1 Du modèle MAD vers le modèle Zgoubi de l'AGS

Le développement du modèle MAD de l'AGS a commencé à la fin des années 1980 [49]. Ce modèle utilise une représentation matricielle des éléments de l'AGS pour déterminer les paramètres optiques le long de l'anneau. Dans sa première mise en oeuvre, seuls les aimants principaux et sections droites ont été inclues. Les aimants principaux ont été simulés en utilisant les forces quadrupolaires et sextupolaires calculées, disponibles pour seulement 6 moments différents (15, 20, 25, 27, 29 and 32 GeV/c). Il est important de noter que la source de ces données n'est pas claire dans les publications disponibles aujourd'hui [49].

Par la suite, le modèle MAD a été utilisé pour le développement et la mise en service des quadrupôles de saut de transition [47, 48], avec un bon accord sur les mesures. La documentation limitée, sur l'évolution du modèle, exclut la composition d'une chronologie plus complète. Aujourd'hui, le modèle courant MADX de l'AGS est bien mieux documenté. Il utilise le code MADX et est accessible par la commande *MadxFromSnaprampCmd* [50].

E.3.2 Modèle des serpents sibériens

Les deux serpents partiaux ont été largement étudiés [57, 58] et de puissants champs magnétiques focalisants ont été constatés, générant des distorsions optiques importantes de la maille de l'AGS à basse énergie. Cela a conduit à l'introduction d'un modèle linéaire des serpents dans le modèle MADX sous la forme de matrices du premier ordre, comme une première approche [56]. Les matrices ont été calculées par l'intégration des trajectoires de particules à travers des cartes de champs calculées des serpents sibériens [57, 58] pour des énergies de protons allant de $G\gamma = 2.5$ à $G\gamma = 26$ par pas de 0.1. Les matrices ont ensuite été simplectifiées en utilisant une transformation de Cayley [59]. Lors de la création du fichier d'entrée de MADX, *MadxFromSnaprampCmd* utilise le moment d'équilibre des protons, déterminé à partir du courant circulant dans les aimants principaux, afin de choisir les matrices correspondantes pour chaque serpent sibérien.

E.3.3 Modèle complet et résultats

Des quadrupôles et sextupôles dédiés sont respectivement utilisés pour contrôler les nombres d'onde et chromaticitées de l'AGS. Les fonctions de transfert permettant de calculer le champ produit par ces aimants sont bien connues [53, 54]. Les fonctions de transfert sont utilisées par le modèle de MADX et ont été introduites dans le code Zgoubi. Un nouvel élément du code Zgoubi, nommé `'AGSQUAD'`, a été développé pour simuler les quadrupôles de l'AGS, basé sur les mêmes fonctions de transfert que le modèle de MADX.

E.3.4 La commande *ZgoubiFromSnaprampCmd*

Le développement du modèle en ligne de l'AGS a été réalisé sur le modèle de la commande MADX existante *MadxFromSnaprampCmd*. La commande *ZgoubiFromSnaprampCmd* utilise un fichier d'entrée (*ZgoubiFromSnaprampCmd.in*) organisé autour de mots clés, signalés par des crochets. Un exemple est donné en annexe C.

La Figure E.6 montre l'évolution des nombres d'ondes de l'AGS durant un cycle d'accélération typique de protons polarisés, avec l'injection depuis l'AGS Booster à 145 ms et l'énergie maximum atteinte à 580 ms.

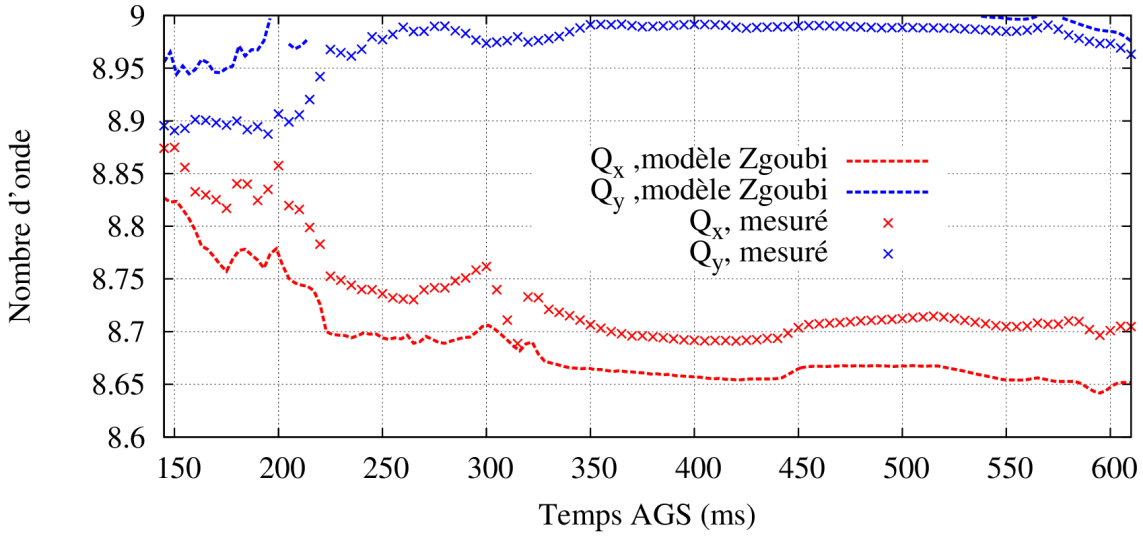

Figure E.6 Nombres d'onde mesurés et prédits par le modèle en ligne de l'AGS le long du cycle d'accélération des protons polarisés, le 14 Avril 2013. L'incertitude statistique sur les nombres d'onde mesurés est négligeable et n'est pas visible ici.

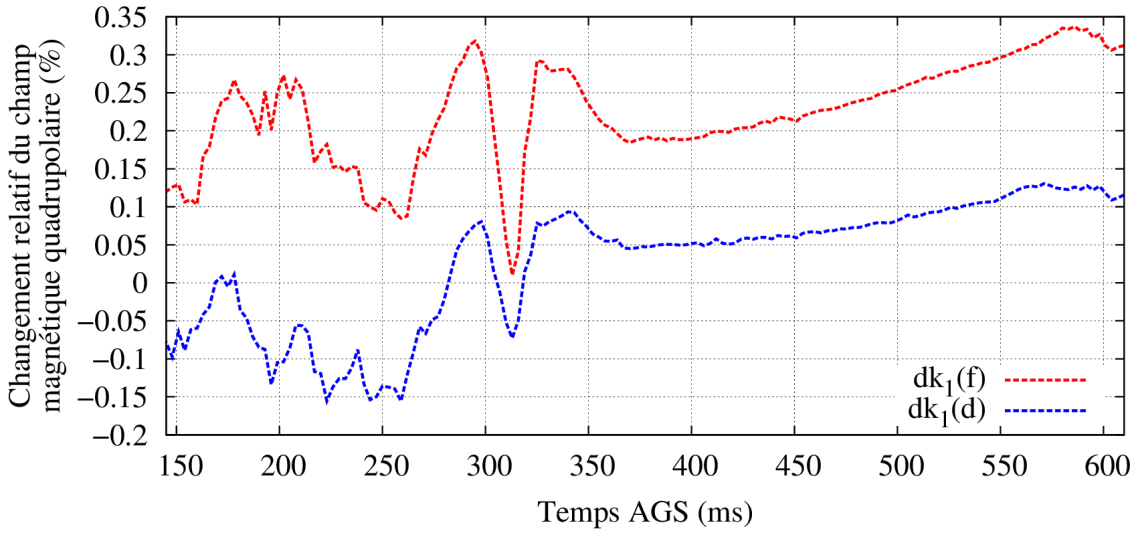

Figure E.7 Changements relatifs requis sur les deux familles d'aimants principaux pour reproduire les nombres d'onde mesurés.

La Figure E.7 montre les variations relatives du champ quadrupolaire ($dk_1(f)$ et $dk_1(d)$), dans les deux familles d'aimants principaux, nécessaires pour faire correspondre les nombres d'onde modélisés aux mesures. Les changements relatifs requis sont toujours très faibles et généralement en dessous de 0.35 %. Il est particulièrement important de reproduire fidèlement les nombres d'onde le long du cycle d'accélération pour simuler précisément la dynamique des particules et de leur spin.

Il est dès lors possible d'utiliser la maille générée ici afin de réaliser le suivi des particules durant le cycle d'accélération, en utilisant le code Zgoubi.

E.4 Suivi de faisceau à long terme dans l'AGS en utilisant le code Zgoubi

Comprendre les sources de dépolarisation dans l'AGS est essentiel pour améliorer les performances de la machine. Des résultats expérimentaux montrent aussi qu'une augmentation de l'émittance transverse se produit lors de l'accélération de protons polarisés [5]. Des codes de suivi de particules uniques et multitours peuvent être utilisés pour étudier ces questions. Le modèle Zgoubi de l'AGS, détaillé dans le Chapitre 3, fournit une représentation réaliste de l'AGS, dans les approximations mentionnées, permettant d'explorer et d'améliorer la dynamique des spins mais aussi du faisceau.

E.4.1 Mise en place de la parallélisation et du suivi multitours

Les données produites le long de la rampe de l'AGS par la commande *ZgoubiFromSnaprampCmd* sont regroupées dans un seul fichier. Le fichier créé contient le comportement de chaque alimentation ou aimant présent dans l'AGS en fonction du temps, ou en fonction du moment d'équilibre des protons, déterminé à partir du courant circulant dans les aimant principaux.

Plusieurs étapes sont ensuite nécessaires afin de préparer les fichiers d'entrées, incluant le reste des éléments nécessaires. La procédure se déroule ainsi:

- les quadrupôles de saut de nombre d'onde sont réglés et temporisés pour une efficacité maximale.
- le système d'accélération RF est réglé pour reproduire fidèlement la vitesse d'accélération de la machine, sans provoquer d'élargissement de l'émittance longitudinale.
- les quadrupôles de saut de gamma de transition sont inclus et le saut de phase du système d'accélération ajusté à l'évolution du gamma de transition.
- les coordonnées initiales des particules suivies sont générées en utilisant des grandeurs réalistes, typiquement rencontrées dans l'AGS pour l'accélération de protons polarisées.

Les fichiers d'entrée sont ensuite téléversés sur les serveur de calcul. A chaque particule suivie est attribué un coeur de calcul unique. Les travaux sont généralement démarrés par groupes de

192 pour éviter les goulets d'étranglement qui peuvent survenir lorsque des milliers de suivis de particules sont initialisés simultanément.

E.4.2 Résultats de suivis et comparaison à des mesures expérimentales

Une des grandeurs pouvant être extraite des résultats de simulation est appelée le profil de polarisation, caractérisé par la grandeur R. Le profil de polarisation permet de sonder les pertes de polarisation dues à la traversée de résonances de dépolarisation intrinsèques par le faisceau. Cette grandeur présente aussi l'avantage d'être directement mesurable à quelque énergie que ce soit, alors que la polarisation absolue ne peut être mesurée qu'à l'énergie d'extraction.

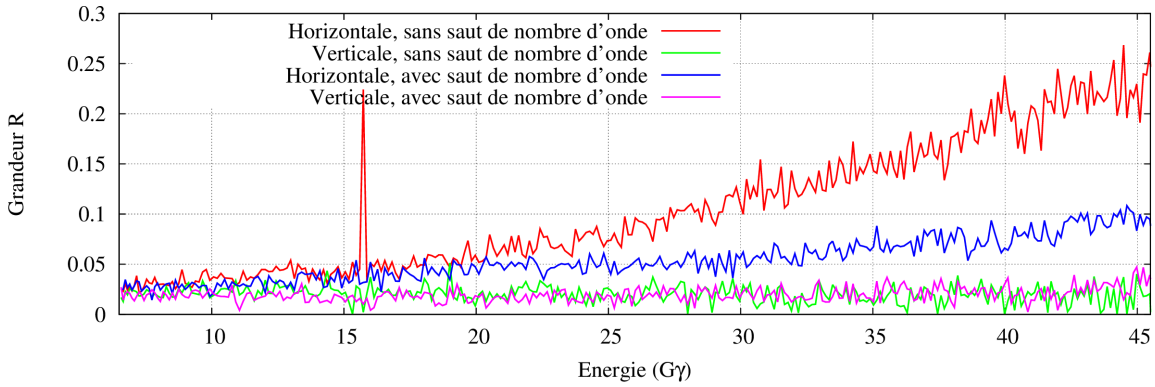

Figure E.8 Profil de polarisation à partir de $G\gamma = 6.5$ simulés par le code Zgoubi, en utilisant des conditions de faisceau et de machine typique.

La Figure E.8 montre l'évolution des profils de polarisation le long du cycle d'accélération de l'AGS. Le profil de polarisation horizontal croît régulièrement le long de la rampe, bien que la dernière partie de l'accélération semble contribuer davantage au profil final. L'utilisation des sauts de nombre d'onde réduit considérablement le profil de polarisation horizontale à $G\gamma = 45.5$ et l'on peut voir Figure E.8 que l'effet est reparti tout au long du suivi.

La table E.2 montre que le profil horizontal mesuré est en accord avec les simulations mais le profil vertical reste largement inexpliqué par les simulations.

Table E.2 Comparaison des profils de polarisation simulés Figure E.8 et mesurés durant l'opération de protons polarisés de l'AGS de l'année 2014.

Mesures [5]		Simulations		Conditions de la machine
R_x	R_y	R_x	R_y	
0.206 ± 0.020	0.181 ± 0.033	0.250 ± 0.007	0.021 ± 0.007	sans sauts de nombre d'onde
0.127 ± 0.019	0.124 ± 0.026	0.100 ± 0.007	0.035 ± 0.007	avec sauts de nombre d'onde

E.5 Simulations et application directe au tTravail expérimental

Alors que nous avons introduit et développé le modèle de l'AGS ainsi que les simulations de suivi de faisceau dans les chapitres précédents, nous allons ici étudier un exemple concret pour l'amélioration de la transmission de la polarisation dans l'AGS.

E.5.1 Perte de polarisation et résonance intrinsèque horizontale

Jusqu'en 2012, le taux d'accélération était diminué lentement à la fin du cycle, afin d'atteindre sans difficulté l'énergie d'extraction.La Figure E.9 montre le taux d'accélération mesuré par rapport à un taux d'accélération constant jusqu'à l'énergie d'extraction. Or, dans le cas où une résonance intrinsèque de spin est traversée plus lentement, la perte de polarisation résultante est plus importante. La question de la perte de polarisation due à la traversée ralentie des quelques dernières résonances intrinsèques horizontales a donc été posée.

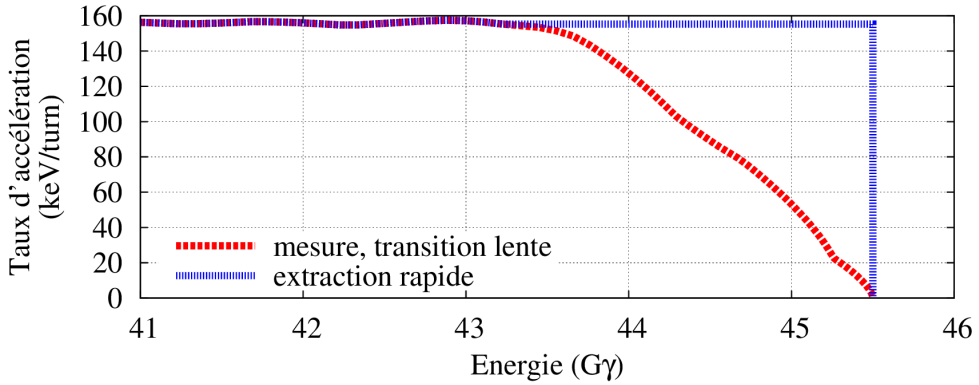

Figure E.9 Taux d'accélération à la fin du cycle, en fonction de l'énergie.

La Tableau E.3 montre les résultats des simulations réalisées grâce aux outils développés dans les chapitres précédents. Il est clair que, sans le système de saut de nombre d'onde, les pertes de polarisation dues à la traversée ralentie des dernières résonances intrinsèques horizontales sont importantes. Avec les système de saut de nombre d'onde le gain dû à un plus haut taux d'accélération est plus faible, ce qui est attendu puisque le système de saut de nombre d'onde accélère lui aussi la vitesse de traversée des résonances intrinsèques horizontales.

Ces résultats, particulièrement prometteurs, ont poussé à la recherche d'une solution pra-

Table E.3 Comparaison de mesures de polarisation, prises en mars 2012, et de simulations avec les deux cycle d'accélération différents.

état de la machine	**polarisation mesurée**	**gain mesuré**	**gain simulé**
sans sauts de nombre d'onde			
transition lente	62.8 ± 1.1 %		
transition rapide	67.3 ± 1.1 %	+7.2%	+6.8%
avec sauts de nombre d'onde			
transition lente	70.1 ± 1.1 %		
transition rapide	70.5 ± 1.1 %	+0.6%	+2.4%

tique permettant de fournir une accélération constante et maximale jusqu'à l'énergie d'extraction, comme dans le cas d'extraction rapide mentionné Figure E.9 ou dans le cas de transition rapide du Tableau E.3. Une solution utilisant des systèmes déjà en place, ainsi qu'un ajustement précis de l'alimentation électrique des aimants principaux de l'AGS, a alors été découverte et jugée suffisamment stable pour une utilisation en opération.

Des mesures de polarisation utilisant la transition rapide ont alors confirmé les résultats des simulations, bien que le gain mesuré lorsque le système de saut de nombre d'onde est actif n'ait pas tout à fait atteint le gain prévu par les simulations. La méthode d'accélération a ainsi été utilisée, dans le cadre des opérations courantes d'accélération de protons polarisés depuis mars 2012.

Cet exemple illustre parfaitement l'utilisation des outils de simulations de l'AGS développés dans les chapitres précédents. Les outils de simulation permettent d'explorer des solutions plus ou moins complexes pour améliorer la transmission de la polarisation dans l'AGS. La prédiction des gains de polarisation permet de diriger au mieux les ressources, investissant expérimentalement dans des schémas ou des modifications du cycle d'accélération pour lesquels des gains substantiels de polarisation sont attendus.

E.6 Conclusion

Le développement du modèle de l'AGS avec le code Zgoubi fournit un outil pour simuler de façon réaliste l'optique de l'AGS. L'utilisation des courants mesurés des aimants assure la précision de l'optique calculée. Qui plus est, les serpents sibériens sont modélisés en utilisant des cartes de champs en trois dimensions simulées, ce qui est particulièrement important, car les dynamiques de faisceau et de spin sont fortement contraintes par ces aimants inhabituelles.

Des capacités en ligne ont été ajoutées et l'interface avec le système de contrôle de l'AGS *ZgoubiFromSnaprampCmd* permet un accès rapide à l'optique modélisé de AGS.

Le suivi des faisceaux, pour de nombreux tours, fournissent d'importants résultats. La polarisation simulée en utilisant le code Zgoubi a montré un bon accord avec les mesures, en particulier pour les dépolarisations dues aux résonances intrinsèques horizontales. Les simulations ont permis de mieux comprendre le comportement de la polarisation dans l'AGS, les défis associés au système de saut de nombre d'onde et la perte de polarisation en fonction de différents paramètres.

La dynamique simulée des faisceaux a également fourni des résultats importants à basse énergie. Le rôle de certaines lignes de résonance non linéaires que le faisceau traverse a été clairement mis en évidence.

Cependant, certains résultats des simulations de suivi du faisceau sont en désaccord avec les expériences. En particulier, les profils verticaux de polarisation mesurés ne sont pas reproduits par les simulations. Des mesures axées sur l'évolution du profil de la polarisation verticale sont prévues pour l'année 2015. La dynamique simulée des faisceaux à basse énergie est également difficile a corréler directement à des mesures. Le rôle des serpents sibériens dans les questions de dynamique des faisceaux observés et simulés tels que les pertes de particules ou augmentation de l'émittance au cours de la rampe n'est pas encore complètement compris.

En outre, des améliorations du modèle Zgoubi restent à faire. Des améliorations de la dynamique de faisceaux à basse énergie sont nécessaires pour simuler complètement le cycle d'accélération de l'AGS. Une meilleure compréhension de la dynamique de faisceaux à basse énergie pourrait également conduire à une meilleure transmission de polarisation via une réduction de l'émittance transverse.

L'introduction d'une orbite réaliste dans le modèle est nécessaire pour mieux comprendre la

dynamique de faisceaux et de spin dans l'AGS. L'étude de l'effet de l'orbite dans la transmission de polarisation reste à étudier.

Enfin, le développement des capacités en ligne du modèle de l'AGS avec un contrôle direct de la machine par le modèle en ligne doivent être entrepris. Cela pourrait simplifier de nombreuses procédures couramment pratiquées par des opérateurs, telles que le réglage de l'orbite et de l'optique, ce qui pourrait également améliorer les performances de la machine.